

NORTHWESTERN UNIVERSITY

X-Ray Scattering Studies of Novel Photoactive Materials

A DISSERTATION

SUBMITTED TO THE GRADUATE SCHOOL
IN PARTIAL FULFILLMENT OF THE REQUIREMENTS

for the degree

DOCTOR OF PHILOSOPHY

Field of Physics and Astronomy

By
Boris Harutyunyan

EVANSTON, ILLINOIS

June 2018

Copyright by Boris Harutyunyan 2018

All Rights Reserved

Abstract

Morphology and crystal structure of photoactive materials are key factors in determining the efficiency of solar devices. We present X-ray scattering studies of four types of photoactive systems with novel photoactive elements: perylene monoimide based nanoribbons for solar-to-fuel conversion devices, tetrathienoacene based organic dyes for dye sensitized solar cells, layered lead perovskites for solar cells and fluorinated small molecule donor for ternary bulk heterojunction solar cells.

We perform wide angle X-ray scattering measurements of perylene monoimide based nanoribbons, both in solution and deposited dry film, and develop formalism for interpreting obtained X-ray scattering patterns. This generally applicable method reproduces the measured diffraction patterns, including the asymmetric line-shapes for the Bragg reflections and yields the molecular packing arrangement within a 2D crystal structure and how it alters upon chemical modification of the constituting molecules. X-ray study of phase transition of n-propyl perylene monoimide nanostructure is discussed as well.

We used X-ray reflectivity technique to study the monolayer morphology of tetrathienoacene based dyes deposited on titanium dioxide surface. The latter serves as an electron channeling electrode in dye sensitized solar cells. Through atomic layer deposition a model surface of titanium oxide is fabricated, and organic dye monolayer deposited on it from organic solution. Analysis of X-ray reflectivity measurements expose the transformations monolayer films undergo upon alterations of backbone structure and modifications of hydrophobic alkyl chains. Alkyl chains are designed to prevent recombination and improve solubility. The results for molecular packing and molecular footprint correlate well with the measured efficiency and other characteristics of solar cells built with these dyes.

Grazing incidence wide angle X-ray scattering was further used to determine orientation of Ruddlesden-Popper perovskite films fabricated with a new deposition method. The analysis indexed all measured

spots on the diffraction pattern which indicated high degree of crystallinity for these films and, crucially, perpendicular alignment of insulator organic spacer with respect to the electrode surface. 12.52% efficiency is achieved for this system with exceptionally high environmental stability, a major hurdle in utilizing perovskites in solar cells.

The same technique is applied in investigation of crystallinity of a blend of fluorinated and non-fluorinated small molecule donor compounds for bulk heterojunction solar cells. These molecules consist of benzodithiophene unit with two diketopyrrolopyrrole moieties. We show that 1:9 blend possesses highest degree of crystallinity. We attributed this effect to formation of C–H···F hydrogen bonding, which improves intermolecular connectivity and enhances photoconductivity. The 1:9 ratio also exhibits the highest efficiency in solar cells as compared to blends with other ratios of constituents.

Acknowledgement

I express my gratitude to my advisor, Prof Michael J. Bedzyk, for his support throughout my research, occasionally in a rather difficult circumstances. Prof Sumit Kewalramani supplied innumerable advices in every aspect of my endeavors. Dr. Guennadi Evmenenko was a constant source of practical wisdom which undoubtedly helped in the success of my experimental work. I thank all our group who did not hesitate in sharing their expertise whenever requested.

This work was supported as part of the Argonne-Northwestern Solar Energy Research (ANSER) Center, an Energy Frontier Research Center funded by the U.S. Department of Energy, Office of Science, Basic Energy Sciences under Award DE- SC0001059. Research in perylene monoimide amphiphiles was conducted in collaboration with the group of Prof Samuel Stupp (Adam Dannenhoffer and Roman Kazantsev), dye sensitized and bulk heterojunction solar cells in collaboration with the groups of Prof Tobin Marks (Nanjia Zhou, Nicholas Eastham, Matthew Leonardi), Prof Ming-Chou Chen and Prof Robert Chang (Peijun Guo), perovskites in collaboration with the group of Prof Mercury Kanatzidis (Dr. Constantinos Stoumpos, Chan Myae Myae Soe).

Table of Contents

1. Introduction	21
2. Overview of elastic X-ray scattering theory.....	23
2.1. Wide-angle X-ray scattering.....	23
2.2. X-ray reflectivity.....	26
3. X-ray studies of molecular packing of amphiphilic PMI nanosheets	31
3.1. Motivation.....	31
3.2. Investigation of MeO-PMI.....	34
3.2.1. Experimental Methods.....	34
3.2.2. Results and Discussion	36
3.3. Accounting for the second chain	50
3.3.1. Applications.....	53
3.4. Summary	64
4. X-ray reflectivity studies of tetrathienoacene based dyes for dye sensitized solar cells	66
4.1. Introduction	66
4.1.1. Operation principle	67
4.2. Donor- π -acceptor (D- π -A) dye design and TiO ₂ electrode.....	68
4.3. TTAR dyes.....	70
4.3.1. Experimental methods.....	73

4.3.2. Assembly study of TTAR dyes on Si/SiO _x	75
4.3.3. Assembly study of TTAR dyes on TiO ₂ films	76
4.3.4. Assembly study of branched TTAR dye.....	80
4.4. Summary	86
5. X-ray studies of perovskite films	88
5.1. X-ray study of 2D perovskites	88
5.1.1. Experimental methods.....	90
5.1.2. GIWAXS analysis of (BA) ₂ (MA) ₂ Pb ₃ I ₁₀ and (BA) ₂ (MA) ₃ Pb ₄ I ₁₃ films.....	91
5.2. Dependence of the phase transition temperature of CH ₃ NH ₃ PbI ₃ on HI additive.....	96
5.2.1. Halide perovskites lattice structure	98
5.2.2. Variable temperature XRR on CH ₃ NH ₃ PbI ₃ films.....	99
6. GIWAXS study of ternary organic photovoltaic films with fluorinated small molecule donor.....	103
7. Summary	111
References	115
8. Appendix A	140
8.1. Synthesis of MeO-PMI	140
8.2. Synthesis of Na ₂ [Mo ₃ S ₁₃] · 5H ₂ O.....	142
8.3. Hydrogen production experiments.....	142
8.4. Peak matching for unit cell parameter deduction	143
8.5. X-Ray Reflectivity and Grazing Incidence X-Ray Scattering	144

8.6. Numerical integration procedure for WAXS intensity	145
8.7. WAXS peak position shifts and shoulder widths estimation	145
8.8. Tilt angle deduction and scattering from tilted chains	148
8.9. Molecular Orbitals and Partial Charges of the Monomer.....	149
8.10. UV-vis spectra for various concentrations of MeO-PMI	151
8.11. Cyclic Voltammetry	151
8.12. WAXS sensitivity to structural details	152
8.13. Statistical errors on GIWAXS fitted parameters	156
9. Appendix B	158
10. Appendix C	160

List of Figures

Figure 2.1. A-B) σ - and π - polarization geometries of X-ray scattering from a single electron. C) 3D schematic depiction of real and reciprocal basis vectors. d is the dipole moment.....	23
Figure 2.2. A) Transmission geometry for wide-angle X-ray scattering (WAXS) measurement. B) Reflection geometry for grazing incidence wide-angle X-ray scattering (GIWAXS) measurement.....	26
Figure 2.3. A) Reflection and refraction from a single interface. B) Geometry of X-ray reflectivity measurement for the slab model of the electron density.....	27
Figure 3.1. Schematic depiction of the excitation of a PMI molecule, with charge separation and electron propagation across the stack until transfer to a water splitting catalyst present in the solution.....	31
Figure 3.2. Schematic depiction of molecular and nano-structure of PMI system along with its catalytic efficiencies for various substituent groups. (Here turnover number (TON) is defined as the number of moles of H ₂ produced divided by the number of moles of the catalyst ([Mo ₃ S ₁₃] ²⁻) for 18 hours of irradiation. TOF is defined as TON / time of the irradiation).	33
Figure 3.3. Hierarchy of structural scales affecting catalytic efficiency of PMI nanostructures.	33
Figure 3.4. A) Pictures of vials containing 1 mM MeO-PMI monomer dissolved in DMSO (left), and assembled nanostructure in water (7.25 mM, right). B) Normalized UV-Vis absorbance spectra for MeO-PMI in DMSO (1 mM) blue, and in water (7.25 mM) red. C) AFM height mode image of MeO-PMI spin-coated from 8.7 mM aqueous solution onto freshly cleaved mica. D) Height line cut of AFM image	

in c (blue line). **E**) Cryo-TEM of 8.7 mM aqueous solution. **F**) SAXS data with Porod analysis and minima sensing the thickness of the nanosheets. 37

Figure 3.5. **A)** GIWAXS reciprocal space data of drop-cast dry sample. q_z is the out-of-plane component of the scattering vector and the in-plane component is $q_r = \sqrt{q_x^2 + q_y^2}$. **B)** Reciprocal space schematic representation of a form factor (red cylinder) at a particular reciprocal lattice vector Gi . Parallelogram outlined by dashed blue lines represents unit cell in reciprocal space..... 40

Figure 3.6. **A)** T-shape projection model of the MeO-PMI. Red arrow indicates dipole moment. **B)** in-plane line-cut of GIWAXS data and model fit to the data with $R^2 = 0.952$. (See Figure A9 for log plot.) Miller indices of diffraction peaks are also shown. Blue dashed line indicates the difference between data and model fit. It is offset for clarity. **C)** Projection of the basis onto the plane of the 2D sheet with selected parameters values determined from the analysis. Longer outlined rectangles represent the perylene fused rings, solid rectangles the carboxypentyl chain above the 2D plane and faded rectangles below, **D)** idealized unit cell with solid and dashed wedges representing carboxypentyl chains above and below the plane of the sheet, correspondingly, **E)** tilt angles of $\pi-\pi$ stacked perynes (longitudinal and transverse shifts are not shown)..... 44

Figure 3.7. **A)** Solution WAXS experimental and fitted curves with peaks indexed for full range of q values. **B)** Expanded view of the (11) peak along with the fit..... 48

Figure 3.8. Graphical illustration of FEs and CTEs in PMI systems. A FE localized at $n = 0$ is shown in the top left corner. This FE can directly couple to a variety of FE and CTE states through the various matrix elements J_c , t_e , and t_h . For example, the exciton can transfer to site $n = 1$ via the long-range excitonic coupling J_c , as shown in the top right corner. The exciton can also dissociate via the charge transfer

integrals t_e and t_h . As shown in the lower left corner, t_h facilitates hole transfer to a neighboring site while the electron remains at the parent molecule. The analogous processes for electron transfer is facilitated by t_e , as illustrated in the lower right corner. Note that the charge transfer process can repeat to yield larger-radius CTEs	50
Figure 3.9. A) 3D slab model of the electron density of PMI molecule. Green sphere models the short chain, while brown cylinder the carboxypentyl chain, B) in-plane projection of the electron density, C) side view of the electron density (solid square corresponds to the attachment point of the carboxypentyl group, while the solid circle to the short chain at position 9), D) top view of the model.	52
Figure 3.10. WAXS patterns, best fits and inferred molecular packing of HO-PMI.....	54
Figure 3.11. Solution WAXS patterns of alkylamino-PMIs. Water background scattering is not fully subtracted.	55
Figure 3.12. GIWAXS patterns for A) propyl, B) isopropyl, C) pentyl, D) 3-pentylamine fresh, E) 3-pentylamine anneal. F) Horizontal line-cuts for each data set.	56
Figure 3.13. Side views of grown single crystal of 3-pentylamino-PMI (orthorhombic symmetry group: P b c a; a = 23.97 \AA , b = 16.51 \AA , c = 35.32 \AA).	57
Figure 3.14. A) Background subtracted WAXS data and model fits for 3-pentylamine PMI. The model is described by a basis set of 4 molecules that occupy a quadrant (parallelogram shown in C) of the oblique 2D unit cell (C) with lattice parameters a and b being twice the edge lengths of the basis set	

parallelogram shown above. The listed (hk) indices are for $a > b$. **D**) Deduced declination angle of the perylene slab with respect to the normal to nanosheet plane.....57

Figure 3.15. Absorbance spectrum of fresh, amorphous 3-pentyl CA (purple trace) in comparison to its crystalline form and the other three chromophores. All traces taken at 7.25 mM.....58

Figure 3.16. Photocatalytic hydrogen evolution experiments for propyl, isopropyl, n-pentyl, fresh 3-pentyl, and annealed 3-pentyl nanostructures gelled with poly (diallyl dimethylammonium) chloride in the presence of ascorbic acid (sacrificial donor) and a molybdenum sulfur cluster. No H_2 was observed if the nanostructures, ascorbic acid, or molybdenum cluster was not present.....58

Figure 3.17. **A)** Molecular structure of T3-PMI chromophore amphiphile, **B)** photographs of 7.25 mM T3-PMI solution with 50 mM NaCl before (left) and after (right) annealing, **C)** cryo-TEM of 7.25 mM T3-PMI with 50 mM NaCl showing ribbons 15 ± 4 nm wide, **D)** cryo-TEM of annealed T3-PMI solution revealing scrolls of 90 ± 13 nm wide, **E)** solution WAXS patterns of freshly dissolved, 50 mM NaCl, and annealed solution of T3-PMI, **F)** absorbance spectra of freshly dissolved T3-PMI with a maximum at 490 nm and a shoulder at 558.5 nm, 50 mM NaCl (α -phase) with a blue shifted absorbance maximum at 420 nm, and the annealed (β -phase) with a maximum at 523 nm and a new feature at 565 nm..60

Figure 3.18. Solution SAXS and WAXS patterns of α - and β - phases. Both graphs have Porod slope of -2, indicating 2D sheet structure.....61

Figure 3.19. **A)** Variable temperature (VT) X-ray scattering patterns of 7.25 mM T3-PMI solution with 50 mM NaCl. Samples were heated at $1^\circ\text{C}/\text{min}$ and data collected every minute, **B)** normalized intensity vs. temperature plots for the 8.3 and 16 nm^{-1} peaks in (A), **C)** VT absorbance spectra of 50 mM NaCl

T3-PMI solution in a 50 μm demountable cuvette monitored at 565 nm. Temperature was ramped at 1°C/min.....	62
Figure 3.20. Solution WAXS patterns of α - and β -phases of T3-PMI along with their fits. Inferred molecular packing and mesoscopic morphology are shown as well.....	64
Figure 4.1. Operating principle of DSSC (DS TiO ₂ = dye sensitized anatase electrode).	67
Figure 4.2. Schematic depiction of electron transfer from donor group to TiO ₂ conduction band upon absorption of photon by a dye molecule.	69
Figure 4.3. Schematic depiction of various dyes covalently bound to ALD deposited TiO ₂ on Si/SiO _x	70
Figure 4.4. Structure of TTAR based dyes.....	71
Figure 4.5. UV-vis absorption spectra of TTAR dyes and their corresponding molar absorption coefficients measured in <i>o</i> -DCB in concentration of 10 ⁻⁵ M.....	72
Figure 4.6. Structure of N719 dye.....	72
Figure 4.7. Electronic structure characterization of organic dyes. A) <i>J-V</i> curves of dyes 1-4 , B) band alignment diagram with respect to conduction band of TiO ₂ , where the HOMO levels were determined from the onset of first oxidation peak and CV experiments, and LUMO levels are derived from film optical bandgap, C) molecular orbital energy diagrams and isodensity surface plots of the HOMO and LUMO for the dyes	73
Figure 4.8. A) and B) AFM images of ALD deposited TiO ₂ on poorly and well hydroxylated Si wafer. C) Lateral inhomogeneity of TiO ₂ thin film on poorly hydroxylated Si manifests itself as a double layer on	

XRR data. Solid black line is a fit for two slab model. D) XRR data for TiO ₂ thin film on well hydroxylated Si. Solid black line is a fit for a single slab model.....	74
Figure 4.9. A) XRR data and model fits. The top three curves are vertically offset for purposes of clarity. Scattering vector $q = 4\pi \sin(2\theta/2) / \lambda$. B) The electron density vs. depth of the sample.....	75
Figure 4.10. A) XRR data and model fits for dye films deposited on ~120Å TiO ₂ . B) The electron density of the organic dyes vs. depth of the sample.	76
Figure 4.11. A) XRR data and model fits for dye films deposited on ~16Å TiO ₂ . B) The electron density vs. depth of the sample. ..	78
Figure 4.12. DFT-optimized geometry of TTAR dyes showing top view (left) and side view (right).....	79
Figure 4.13. XRR data and best fit for N719 dye monolayer on TiO ₂ alongside the extracted characteristics of the film.	79
Figure 4.14. Structure of branched TTAR dyes.	80
Figure 4.15. Orbital energy levels of molecules 1-3 . A) DPV-derived HOMO and LUMO energy levels, B) DFT derived molecular orbitals, C) optimized molecular structures with dihedral angles shown.	81
Figure 4.16. A) UV-vis absorption spectra of dyes 1-3 and their corresponding molar absorption coefficients measured in <i>o</i> -C ₆ H ₄ Cl ₂ at a concentration of 10 ⁻⁵ M, B) absorption spectra of the dye-sensitized nanocrystalline TiO ₂ films.....	81
Figure 4.17. The photocurrent current density–voltage (<i>J-V</i>) characteristics of the DSSCs with various dyes, measured under 1 sun illumination.	82

Figure 4.18. A) Configuration of the cell with the 3-D photonic crystals (inserted in photo- and SEM images of 3D PhC), B) The photocurrent current density–voltage (J - V) and D) power-voltage (P - V) characteristics of the DSSCs with TTAR-b8 and 3D PC under 1 sun illumination	83
Figure 4.19. A) XRR experimental data (circles, red - TTAR-b8 , green - TTAR-9 , blue - TTAR-15) and best fitting curves (solid black lines), B) electron density profiles determined from the fits. Dashed lines indicate the density profiles of the dye layers after subtracting the TiO_2 profile (the red dashed line is for the layer adjacent to TiO_2).....	84
Figure 4.20. Schematic depictions of plausible models conforming to the deduced parameters and XRR determined profiles from Figure 4.19B for TTAR-15 (TTAR-9) and TTAR-b8	86
Figure 5.1. Unit cell structure of methylammonium lead perovskite ($\text{CH}_3\text{NH}_3\text{PbI}_3$). A) (001) view, B) side view. (I 4 c m, $a = 8.849 \text{ \AA}$, $c = 12.642 \text{ \AA}$).....	89
Figure 5.2. Lattice structure of $(\text{BA})_2(\text{MA})_{n-1}\text{Pb}_n\text{I}_{3n+1}$ for $n = 3, 4$	89
Figure 5.3. A, B) GIWAXS patterns for polycrystalline room-temperature-cast (A) and hot-cast (B) near-single-crystalline $(\text{BA})_2(\text{MA})_3\text{Pb}_4\text{I}_{13}$ perovskite films with Miller indices of the most prominent peaks shown in white. Color scale is proportional to X-ray scattering intensity, q is the wavevector transfer, q_z is perpendicular to the sample, q_y is parallel to both the sample and the detector. C) Schematic representation of the (101) orientation, along with the (111) and (202) planes of a 2D perovskite crystal, consistent with the GIWAXS data.....	91
Figure 5.4. A) Triclinic unit cell embedded in the Cartesian frame, B) Laue condition for a polycrystalline powder oriented with the plane $p_n \perp \hat{n}$	93

Figure 5.5. Simulated GIWAXS pattern for $(BA)_2(MA)_3Pb_4I_{13}$ with (101) plane parallel to the substrate. Labels have the following format: {Miller indices hkl , intensity in arbitrary units}.	96
Figure 5.6. $CH_3NH_3PbI_3$ phase transition sequence. At high temperatures, it crystallizes in the pseudo-cubic phase ($P4mm$ space group). Upon cooling, it transforms into the tetragonal structure ($I4cm$ space group) at approximately 330 K. Lowering the temperature further results in an additional phase transition to the orthorhombic phase ($Pbn2_1$ space group) around 160 K ¹⁵¹ .	99
Figure 5.7. Simulated X-ray diffraction patterns of $CH_3NH_3PbI_3$: 3D powder of the tetragonal phase ($I4cm$) at 293 K (black), 3D powder of the pseudo-cubic phase ($P4mm$) at 400 K (red), and the ($I4cm$) textured phase with preferred orientation along the (022) plane at 293 K (blue) ¹⁵³ . The $I4cm \rightarrow P4mm$ transition results in suppression of the (211) reflection at 23.54° ($Cu K_\alpha$) whereas a preferred orientation in the $I4cm$ phase suppresses the (211) reflection as well as the (114), (222) and (310) reflections at 31.7°..	100
Figure 5.8. Cu $K\alpha$ X-ray powder diffraction patterns of $CH_3NH_3PbI_3$ films on ITO/PEDOT:PSS prepared with the indicated HI concentrations. The * asterisks represent ITO peaks from the substrate. The # represents PbI_2 peak. The intensity is normalized to that of (110) reflection at 13.9°.	100
Figure 5.9. 2D view of peak reflectivity (intensity) vs. temperature and scattering angle for various HI weight fractions, of characteristic (211) reflection at $2\theta = 23.3^\circ$ for $CH_3NH_3^+PbI_3^-$ films, demonstrating the $I4cm \rightarrow P4mm$ phase transformation.	102
Figure 5.10. Background subtracted peak integral reflectivity vs. temperature	102
Figure 6.1. Phenyl-C61-butrylic acid methyl ester (PCBM)	103

Figure 6.2. A) Molecular structures of **PH** and **PF₂** used in this study. B) CV-derived HOMO levels and optical absorption-derived LUMO levels of both donor materials. C) Solution and film UV-vis spectra of **PH** and **PF₂** exhibiting virtually identical bandgaps due to the minimal backbone effect of fluorination.

105

Figure 6.3. A) Current density versus voltage and B) EQE curves of solar cells based on binary and ternary blends of **PH** and **PF₂** with **PC₆₁BM**. C) Trends in PCE, J_{sc} , and D) V_{oc} with composition of ternary blend.

107

Figure 6.4. A) 2-D GIWAXS patterns of blend films containing **PH**, **PF₂**, and **PCBM** at various ternary ratios, B) zoomed GIWAXS pattern of 10:90 blend.....108

Figure 6.5. A) Diffuse reflectance UV-vis absorption measurements for binary and ternary **PH:PF₂** blends with **PC₆₁BM**. 3-D Bubble plots depicting the spacing and intensity of crystalline diffractions and the relative size of the crystallite domains as determined by Scherrer analysis of B) **PH**, C) **PF₂**, and D) the optimal ternary blend.....109

Figure 6.6. A) Ratio of intensities of edge-on to face-on aligned stacks for low q peak corresponding to the spacing ~17-18Å, B) domain size in a direction parallel to substrate extracted by Scherrer formula.

109

Figure 6.7. A) Horizontal ($q_z \approx 0$) and B) vertical ($q_r \approx 0$) line-cuts taken from the 2D GIWAXS patterns of ternary blend films containing **PH**, **PF₂** and **PCBM**.....110

Figure 8.1. **A)** Specular X-ray reflectivity of drop-cast samples on Si wafer and glass. Annealing of the dried sample was performed in a vacuum oven at 40°C for 24 hours. **B)** Normalized specular X-ray reflectivity

of spin cast films, **C)** X-ray diffraction pattern of drop-cast samples at a fixed grazing incident angle of 1° for the glass substrate and 2° for the Si wafer. The top curves are vertically offset in **A-C** for purposes of clarity. q is the wavevector transfer. Scattered X-ray counts in **A-C** were collected by a point detector on a Rigaku SmartLab instrument in the NU X-ray Diffraction Facility. **D)** Vertical line-cut in GIWAXS pattern of Figure 3.5A with constraint: $-0.05\text{\AA}^{-1} < q_y < 0.05\text{\AA}^{-1}$ (here $q = \sqrt{q_x^2 + q_y^2 + q_z^2}$) 144

Figure 8.2. Peak asymmetry illustration and shoulder widths definition. ½ for the high-q shoulder is introduced to account for decrease in the form factor along the normal to the sheet. 146

Figure 8.3 RSS as a function of number of variables retained in the model. 147

Figure 8.4. **A)** Schematic depiction of the perylene tilt angle, **B)** Geometry of X-ray scattering from a tilted rod (carboxypentyl chain). 148

Figure 8.5. Derived tilt angle as a function of chosen slab height. 148

Figure 8.6. HOMO, LUMO and partial charge distribution of MeO-PMI-Me. 150

Figure 8.7. UV-Vis absorbance spectra of MeO-PMI at concentrations 0.0725, 0.725 and 7.25 mM in water. Green curve manifests disappearance of monomer peak and formation of nanosheets. 151

Figure 8.8. Cyclic voltammogram of MeO-PMI (5 mM) in DCM with 0.1 M tetrabutylammonium hexafluorophosphate as the supporting electrolyte. Ferrocene internal standard was used to calibrate scans. Inset shows an energy diagram constructed from CV and UV-Vis data. 152

Figure 8.9. Best fit to the full model from the main text in the log scale of counts. 153

Figure 8.10. The best fit for a model consisting of plates without carboxypentyl chains 153

Figure 8.11. Best fits for models with the angle of the chain with respect to the plate frozen to normal
during fitting procedure 154

Figure 8.12. Best fit for a model with zero tilt angle (i.e. rotational angle between two plates is 0) 155

Figure 8.13. Best fit for a model with 8.2° tilt angle (i.e. rotational angle between two plates is 16.4°) 155

Figure 8.14. Best fit for a model with 31.4° tilt angle (i.e. rotational angle between two plates is 62.8°)

..... 156

List of Tables

Table 4.1. Characteristics of TTAR based DSSCs	71
Table 4.2. Extracted film parameters from XRR data fits for dye films deposited on Si/SiO _x	75
Table 4.3. Extracted film parameters from XRR data fits for dye films deposited on ~120Å TiO ₂	76
Table 4.4. Summary of XRR-derived parameters for dye films deposited on ~16Å TiO ₂	79
Table 4.5. Photovoltaic parameters of the DSSCs with various dyes.	82
Table 4.6. Photovoltaic parameters of the DSSCs with TTAR-b8 and 3D PC under 1 sun illumination.....	83
Table 4.7. Dye layer parameters inferred from XRR determined electron density profiles.....	84
Table 6.1. OPV performance of PH:PF ₂ :PC ₆₁ BM OPV devices at various donor component weight ratios.	106
Table 8.1. Statistical uncertainties on fit parameters at 95% confidence level.....	157

1. Introduction

Increasing the share of solar energy in the global energy production sector is one of the big challenges for modern economies. The advantage of this form of energy primarily lies in its abundance and low environmental footprint. It also has a potential of ensuring energy independence of advanced economies. Two of the fast-developing areas of solar energy research are organic/hybrid solar cells and solar-to-fuel conversion devices. Various photoactive materials have been investigated for these devices, some of the most efficient ones being serendipity discoveries while others purposefully designed. It is recognized that not only the electronic structure of constituting molecules and bulk crystals but also the morphology of the photoactive material in the final device are of crucial importance. X-ray scattering techniques provide a convenient and powerful means to reveal the morphology and self-assembly modes of these systems from sub-angstrom to micron scale, thereby allowing elucidation of factors responsible for the high efficiency of certain structures.

In our current work we focus on X-ray scattering studies of perylene monoimide (PMI) based nanoribbons for hydrogen producing solar-to-fuel conversion devices and tetrathienoacene based monolayers for dye sensitized solar cells (DSSC), but we will briefly discuss some structural aspects of perovskite films, the new highly efficiency photoactive material of intense interest by the research community, and fluorinated small molecule donors for ternary bulk heterojunction solar cells.

In Chapter 2 we will derive the expressions for differential cross-section of elastic X-ray scattering from small crystals in kinematic approximation for later use in our modelling of wide-angle X-ray scattering from 2D nanosheets. In the same chapter Parratt formalism of X-ray reflectivity from flat surfaces will be presented. Discussion of small- and wide-angle X-ray scattering studies (SAXS and WAXS) of PMI nanoribbons/nanosheets will follow immediately in Chapter 3. We will then proceed to X-ray reflectivity

(XRR) studies of tetrathienoacene-based dye thin films for dye sensitized solar cells (Chapter 4) and end with grazing incidence wide-angle X-ray scattering studies (GIWAXS) of perovskite and fluorinated organic films (Chapters 5 and 6).

2. Overview of elastic X-ray scattering theory

2.1. Wide-angle X-ray scattering

Scattering of X-rays from a charged object is conventionally characterized by differential cross section, which is the ratio of scattered energy per unit time (power) in specified solid angle and magnitude of the

Poynting vector of the incoming beam: $d\sigma = \frac{d\bar{P}_{scatt}}{\bar{S}_{in}} = \frac{|\vec{E}_{scat}|^2 R^2}{|\vec{E}_{in}|^2}$, where R is the distance from the sample

to the detector, \vec{E} is the electric field strength vector and overbar denotes time averaging. Differential cross section for elastic X-rays scattering from a free electron in the simple Thomson scattering approximation can be written as following¹⁻²:

$$\frac{d\sigma}{d\Omega} = r_0^2 |\hat{\epsilon} \cdot \hat{\epsilon}'|^2 \quad (2.1)$$

where $\hat{\epsilon}$ and $\hat{\epsilon}'$ are the polarizations of incoming and scattered beams, respectively, and $r_0 = \frac{e^2}{4\pi\epsilon_0 mc^2} =$

$2.82 \cdot 10^{-5} \text{ \AA}$ is the Thomson scattering length (also known as classical electron radius). For the case of σ polarization of the incoming beam (Figure 2.1A): $P = |\hat{\epsilon} \cdot \hat{\epsilon}'|^2 = 1$, and for π polarization (Figure 2.1B):

$P = |\hat{\epsilon} \cdot \hat{\epsilon}'|^2 = \cos^2 2\theta$. Polarization factor P for fully unpolarized beam is given by the following expression:

$$P = \overline{|\hat{\epsilon} \cdot \hat{\epsilon}'|^2} = \frac{1}{2}(1 + \cos^2 2\theta) \quad (2.2)$$

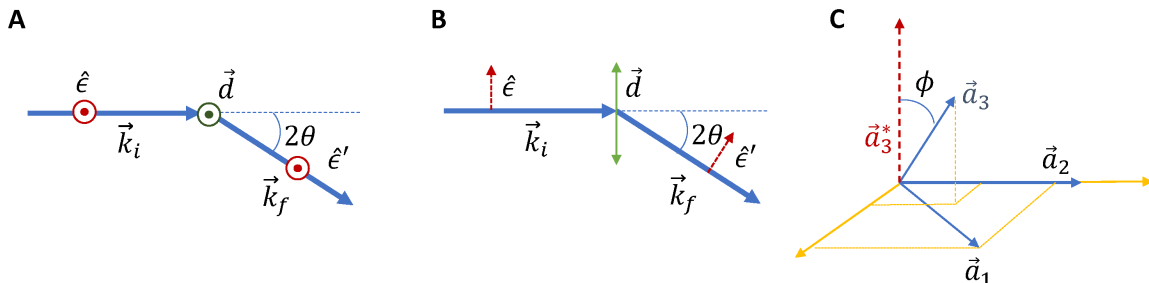


Figure 2.1. **A-B)** σ - and π - polarization geometries of X-ray scattering from a single electron. **C)** 3D schematic depiction of real and reciprocal basis vectors. \vec{d} is the dipole moment.

We now proceed from a fixed single electron to considering the scattering from an extended structure with the spatial electron number density $\rho(\vec{r})$. If the incoming X-ray beam has a frequency far from excitation edges (fundamental frequencies of the system of charges) then in a first order approximation (neglecting secondary scattering events) the differential cross section can be written as following:

$$\frac{d\sigma(\vec{q})}{d\Omega} = r_0^2 P \left| \int \rho(\vec{r}) \cdot e^{i\vec{q} \cdot \vec{r}} d^3 r \right|^2 \quad (2.3)$$

where wavevector transfer $\vec{q} = \vec{k}_{scat} - \vec{k}_{in}$ and $q = \frac{4\pi}{\lambda} \sin\left(\frac{2\theta}{2}\right)$ at the X-ray wavelength λ and scattering angle 2θ .

Scattering differential cross section of a small single crystal described by a primitive lattice with $2N + 1$ unit cells and a single basis at each lattice point, can be calculated by assigning a position vector \vec{R}_i to each lattice point and position \vec{r}' to an electron density element within the basis (i.e., primitive unit cell) with respect to the corresponding lattice point. Hence, the absolute position of the density element $\vec{r} = \vec{r}' + \vec{R}_i$. With this notation, we recast the expression 2.3 as following:

$$\begin{aligned} \frac{d\sigma(\vec{q})}{d\Omega} &= r_0^2 P \left| \int_{\vec{r} \subset V} \rho(\vec{r}) e^{i\vec{q} \cdot \vec{r}} d^3 r \right|^2 = r_0^2 P \left| \sum_{i=-N}^{i=N} \int_{\vec{r} \subset \Delta V_i} \rho(\vec{r}' + \vec{R}_i) \cdot e^{i\vec{q} \cdot (\vec{r}' + \vec{R}_i)} d^3 r' \right|^2 \\ &= r_0^2 P \left| \sum_{i=-N}^{i=N} e^{i\vec{q} \cdot \vec{R}_i} \int_{\vec{r}' \subset \Delta V} \rho(\vec{r}') e^{i\vec{q} \cdot \vec{r}'} d^3 r' \right|^2 \end{aligned}$$

We define the structure factor of the basis (or primitive unit cell) as the integral in the above expression:

$$F(\vec{q}) = \int_{\vec{r}' \subset \Delta V} \rho(\vec{r}') e^{i\vec{q} \cdot \vec{r}'} d^3 r' \quad (2.4)$$

With unit cell sides \vec{a}_k , real space lattice vector $\vec{R}_i = \sum_{k=1}^n n_k \vec{a}_k$, where n is the dimensionality of the system and index i enumerates the sets of integers $\{n_k; k = 1..n\}$. Hence:

$$\frac{d\sigma(\vec{q})}{d\Omega} = r_0^2 P \cdot |F(\vec{q})|^2 \prod_{k=1}^n \left(\frac{\sin[1/2 \vec{q}_k \cdot \vec{a}_k (2N_k + 1)]}{\sin[1/2 \vec{q}_k \cdot \vec{a}_k]} \right)^2 \quad (2.5)$$

where $\vec{q}_k \parallel \vec{a}_k^*$ for reciprocal basis vector \vec{a}_k^* ($\vec{q} = \sum_{k=1}^n \vec{q}_k$). For purposes that will become apparent later, we approximate the 1D interference function under the product operator around the zeros of its denominator ($x = \pi j$, where $j \in \mathbb{Z}$) by a Gaussian which has the same height at the zeros³:

$$\frac{\sin^2 N x}{\sin^2 x} \rightarrow N^2 e^{-(N(x-\pi j))^2/\pi} \quad (2.6)$$

Justification for this substitution is further strengthened by the equality of their integrals:

$\int_{-\pi/2+\pi j}^{\pi/2+\pi j} \frac{\sin^2 N x}{\sin^2 x} dx = \pi N = \int_{-\infty}^{\infty} N^2 e^{-(N(x-\pi j))^2/\pi} dx$. Comparing expressions 2.5 and 2.6, we identify

$x = 1/2 \vec{q}_k \cdot \vec{a}_k$ and $N = 2N_k + 1$. For simplicity, we relabel $2N_k + 1 \rightarrow N_k$. Hence (Figure 2.1C):

$$\begin{aligned} N(x - \pi j) &\rightarrow N_k/2 (\vec{q}_k \cdot \vec{a}_k - 2\pi j_k) = \frac{N_k \cdot 2\pi}{2a_k^*} (q_k - j_k a_k^*) = N_k a_k / 2 \cdot \cos \phi \cdot (q_k - G_k) \\ &= L_k / 2 (q_k - G_{k,j_k}) \end{aligned}$$

where L_k is the domain length in a direction $\hat{L}_k \parallel \vec{a}_k^*$ and $j, j_k \in \mathbb{Z}$. With these identities, expression 2.5 reduces to:

$$\frac{d\sigma(\vec{q})}{d\Omega} = r_0^2 P \cdot |F(\vec{q})|^2 \sum_j \prod_{k=1}^n N_k^2 e^{-\frac{(q_k - G_{k,j_k})^2}{2\sigma_k^2}} \quad (2.7)$$

where $\sigma_k = \sqrt{2\pi} / L_k$ and j enumerates sets of integers $\{j_k; k = 1..n\}$. If all domain lengths are equal, then differential cross-section of a single domain can be written as follows:

$$\frac{d\sigma(\vec{q})}{d\Omega} = r_0^2 P \cdot |F(\vec{q})|^2 e^{-q^2 c_{DW}} \cdot N^2 \sum_j e^{-\frac{(\vec{q} - \vec{G}_j)^2}{2\sigma^2}} \quad (2.8)$$

where summation is over reciprocal lattice vectors and N is the number of unit cells in the domain under beam illumination. We also introduced the Debye-Waller factor $e^{-q^2 C_{DW}}$ to account for thermal fluctuations of atoms around equilibrium points.

The last two expressions for X-ray scattering from a small single crystal, with the appropriate ensemble averaging over a collection of domains, will be the working formulas for our modeling of the wide-angle X-ray scattering (WAXS) from 2D nanoribbons. WAXS technique is based on illuminating the sample with X-ray beam either in transmission (Figure 2.2A), or reflection (Figure 2.2B) geometry at a small incidence angle (typically less than a degree), and recording the diffraction pattern by a 2D detector.

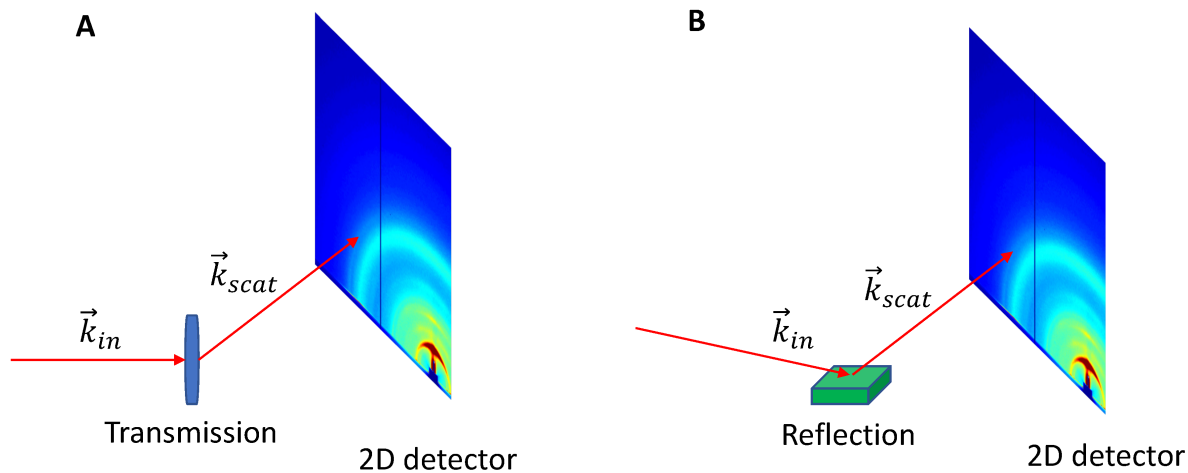


Figure 2.2. **A)** Transmission geometry for wide-angle X-ray scattering (WAXS) measurement. **B)** Reflection geometry for grazing incidence wide-angle X-ray scattering (GIWAXS) measurement.

2.2. X-ray reflectivity

The frequency of X-ray beams used in scattering experiments is much higher than most of the absorption resonance frequencies of atoms. Consequently, the refraction index for X-rays is less than unity, but extremely close to it ($n = 1 - \delta$, where $\delta \sim 10^{-6}$). Total external reflection (TER) is routinely

observed in X-ray reflectivity (XRR) experiments when the incident angle θ is less than the critical angle deduced from Snell's Law: $\theta_c = \sqrt{2\delta}$.

Strictly speaking the index of refraction is complex ($n = 1 - \delta + i\beta$, where δ accounts for refraction effects and β for absorption effects). The refraction index can be expressed through atomic form factor $f^0(\vec{q})$ or, for higher accuracy with small dispersion corrections: $f(\vec{q}) = f^0(\vec{q}) + f' + if''$, yielding²:

$$n = 1 - \frac{2\pi r_0}{k^2} \left(\sum_m \rho_m (f_m^0(0) + f'_m + if''_m) \right) \quad (2.9)$$

where ρ_m is the atom number density of the type m atoms in the film ($k = \frac{2\pi}{\lambda}$). For small wavevector transfers $f_m^0(\vec{q}) \approx f_m^0(0) = Z_m$, where Z_m is the atomic number. From expression 2.9: $\delta = \frac{2\pi r_0}{k^2} \sum_m \rho_m (f_m^0(0) + f'_m)$ and $\beta = -\frac{2\pi r_0}{k^2} \sum_m \rho_m f''_m$.

Reflectivity experiments are performed in θ - 2θ specular mode, i.e. the incidence and take-off angles are equal at each point of the scan, thereby wavevector transfer is always aligned along the normal to the surface (Figure 2.3).

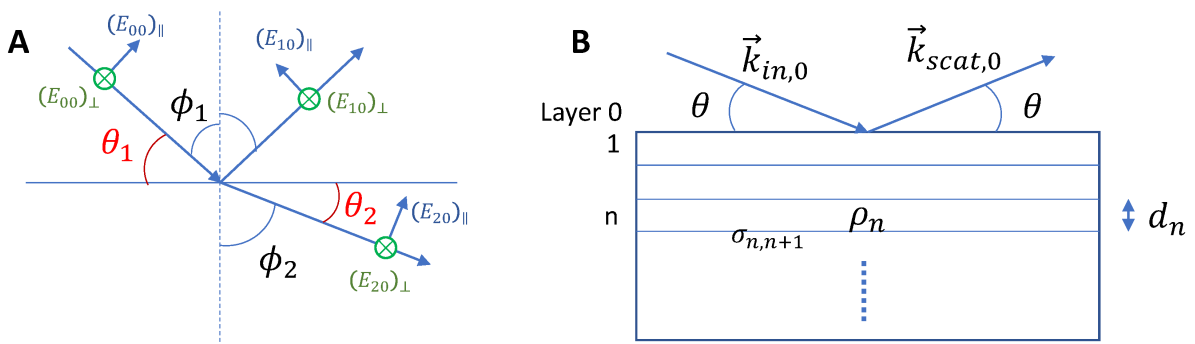


Figure 2.3. **A)** Reflection and refraction from a single interface. **B)** Geometry of X-ray reflectivity measurement for the slab model of the electron density.

Reflectivity is defined as a ratio of intensities of scattered and incident beams: $R = I_{scat}/I_{in}$. For a single flat interface, Fresnel theory establishes the relation between reflected and incident E -field amplitudes (Figure 2.3A):

$$(E_{10})_{\parallel} = \frac{\sin 2\phi_1 - \sin 2\phi_2}{\sin 2\phi_1 + \sin 2\phi_2} (E_{00})_{\parallel} \quad (2.10)$$

$$(E_{10})_{\perp} = -\frac{\sin(\phi_1 - \phi_2)}{\sin(\phi_1 + \phi_2)} (E_{00})_{\perp} \quad (2.11)$$

For grazing angles, we keep only the first order terms:

$$(E_{10})_{\parallel} = \frac{\theta_1 - \theta_2}{\theta_1 + \theta_2} (E_{00})_{\parallel} \quad (2.12)$$

$$(E_{10})_{\perp} = \frac{\theta_1 - \theta_2}{\theta_1 + \theta_2} (E_{00})_{\perp} \quad (2.13)$$

We notice that for small angles normal projection of the wavevector $k_z = k\theta$. Hence, the ratio of reflected and incident E -field amplitudes for both polarizations can be combined into the following expression:

$$r = \frac{k_{z,1} - k_{z,2}}{k_{z,1} + k_{z,2}} \quad (2.14)$$

Let's consider reflection at a limit $\theta_2 \gg \theta_c$ with $n_1 = 1$, $\beta_2 = 0$ and $\theta_c = \sqrt{2\delta_2}$. We still assume that the angle θ_2 is small enough to justify Taylor expansion $\cos \theta_2 \approx 1 - \theta_2^2/2$. Hence, Snell's law reduces to $\theta_2^2 = \theta_1^2(1 + \theta_c^2/2) - \theta_c^2$. By substituting this result into expressions 2.12 and 2.13, E-field amplitude ratio takes the following form:

$$r = \frac{\theta_1 - \sqrt{\theta_1^2 - \theta_c^2}}{\theta_1 + \sqrt{\theta_1^2 - \theta_c^2}} = \frac{\frac{\theta_1}{\theta_c} - \sqrt{\left(\frac{\theta_1}{\theta_c}\right)^2 - 1}}{\frac{\theta_1}{\theta_c} + \sqrt{\left(\frac{\theta_1}{\theta_c}\right)^2 - 1}} \quad (2.15)$$

Denoting $Q \equiv \frac{\theta_1}{\theta_c}$, expansion of the above expression around infinity yields ($r = r_F + O(Q^{-4})$):

$$r_F = (2Q)^{-2} \quad (2.16)$$

And the resulting reflectivity from an ideal sharp interface (Fresnel reflectivity) is given by the following:

$$R_F = (2Q)^{-4} \quad (2.17)$$

In view of this result it is convenient to deal with the dependence of Rq^4 on q instead of $R(q)$, i.e. to factor out the Fresnel reflectivity. We will follow this convention in our presentation.

To advance beyond the single interface to a set of parallel interfaces depicted in Figure 2.3B, Parratt constructed a recursive algorithm to calculate reflectivity from a thin film supported on a substrate with a given electron density profile along the normal to the interfaces. The sample is divided into horizontal slabs with thicknesses d_n and densities ρ_n . The interfaces between the layers have roughnesses $\sigma_{n,n+1}$. In the first order approximation, the normal component of the refracted wavevector in the n th slab can be expressed as following:

$$k_{z,n} = \sqrt{k_{0,z}^2 - 2(\delta_n - \delta_0)k_0^2 + 2i(\beta_n - \beta_0)k_0^2} \quad (2.18)$$

From the Fresnel equations, reflected E-field amplitude ratio from $(n, n+1)$ interface can be written as^{2,4}:

$$r_{n,n+1} = \frac{k_{z,n} - k_{z,n+1}}{k_{z,n} + k_{z,n+1}} e^{-2k_{z,n}k_{z,n+1}\sigma_{n,n+1}^2} \quad (2.19)$$

However, if roughness is taken into account implicitly through finer horizontal divisions of the film, amplitude ratio is given by the expression 2.14:

$$r_{n,n+1} = \frac{k_{z,n} - k_{z,n+1}}{k_{z,n} + k_{z,n+1}} \quad (2.20)$$

By introducing coefficient $\beta_n = k_{z,n}d_n$, we define a characteristic matrix for the n th layer:

$$c_n = \begin{bmatrix} e^{\beta_n} & r_n e^{\beta_n} \\ r_n e^{-\beta_n} & e^{-\beta_n} \end{bmatrix} \quad (2.21)$$

Total reflectivity from the top interface then is expressed through these characteristic matrices for each layer:

$$M = \prod_0^n c_n \quad (2.22)$$

$$R = \left| \frac{M_{00}}{M_{10}} \right|^2 \quad (2.23)$$

This algorithm allows efficient numerical implementations even for a large number of slabs.

3. X-ray studies of molecular packing of amphiphilic PMI nanosheets

3.1. Motivation

Amphiphilic perylene monoimide (PMI) compounds, containing ionizable groups, have the ability to self-assemble into 2D nanostructures, which gel and develop strong X-ray diffraction peaks in the presence of charge-screening ions. These systems have been suggested as bioinspired photocatalytic scaffolds for water splitting reactions due to their ability to support mobile excitons, propagating along the π - π stacking direction of the nanostructures⁵⁻⁶. Figure 3.1 depicts schematically the formation of a Frenkel exciton (Fig. 3.1 middle) upon photon absorption by a PMI molecule. Depending upon the coupling strengths, the Frenkel exciton can either dissociate (top) or remain bound (bottom). If it dissociates, the delocalized electron propagates through the PMI stack until it transfers to catalytic molecule, which triggers water molecule splitting. If the exciton remains bound, it will ultimately recombine without producing a hydrogen molecule. Coupling strengths of these competing states depend crucially on packing modes of individual stacks and nanostructure morphology as a whole.

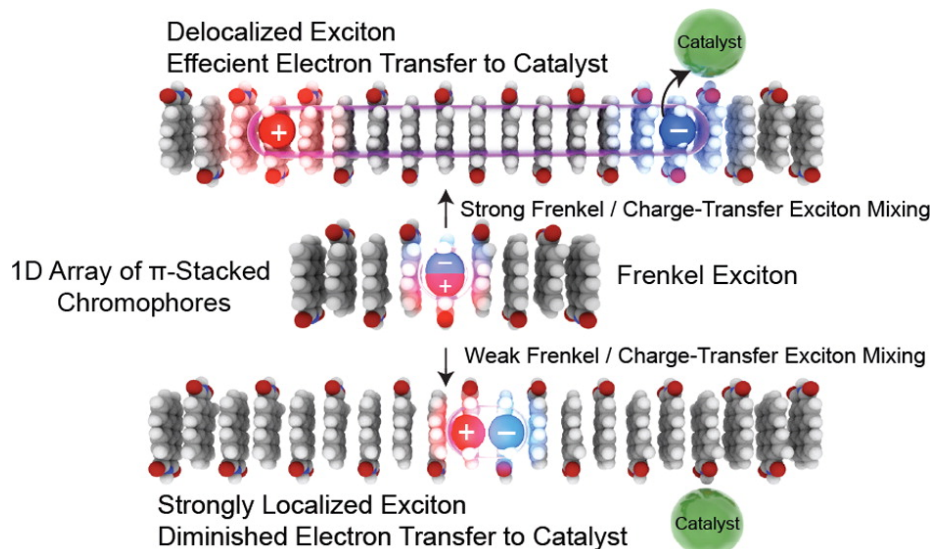


Figure 3.1. Schematic depiction of the excitation of a PMI molecule, with charge separation and electron propagation across the stack until transfer to a water splitting catalyst present in the solution (reprinted with permission from Hestand, et al. ⁶).

The highly ordered nature of the nanostructures allows in-depth analysis of how different crystal packing arrangements impact the catalytic ability of such materials, a feature not possible for amorphous assemblies⁷. It is known that the electronic and self-assembly properties of rylene-based compounds can be controlled by addition of substituent groups at various locations on the aromatic core⁷⁻¹². This provides an opportunity to create a library of different amphiphilic PMIs, which assemble into distinct crystalline packing arrangements with corresponding unique photophysical and catalytic properties.

PMI molecules form monomolecular solutions in polar organic solvents (e.g. DMSO). Electronic properties of individual molecules can be investigated in these solutions through various spectroscopic techniques. Quantum chemical computations give further reliable predictions of conformation of PMI molecules, both in solution and in gas form. However, molecular packing and mesoscopic morphology in these light harvesting 2D assemblies in aqueous solution are key factors for conversion efficiency (Figure 3.2, Figure 3.3). Structure-function correlations on this scale have yet to be fully established. This is partly due to the difficulties in extracting the molecular arrangements from the complex 3D powder averaged diffraction patterns of 2D lattices, obtained via in-situ wide-angle X-ray scattering.

In order to establish a clear structure-property relationship, small- and wide-angle X-ray scattering techniques (SAXS and WAXS) are vital methods for elucidating the structure of 2D PMI materials, which typically do not form 3D single crystals. Furthermore, single crystal data would not necessarily replicate the assembly state in solution, hence in situ solution WAXS experiments are of primary interest for studying such materials as it removes the risk of structural modifications caused by environment change. The development of X-ray scattering theory-based models will allow for an improved understanding of the crystal structures of self-assembled 2D-nanostuctures and facilitate the discovery of photocatalytic scaffolds with superior properties.

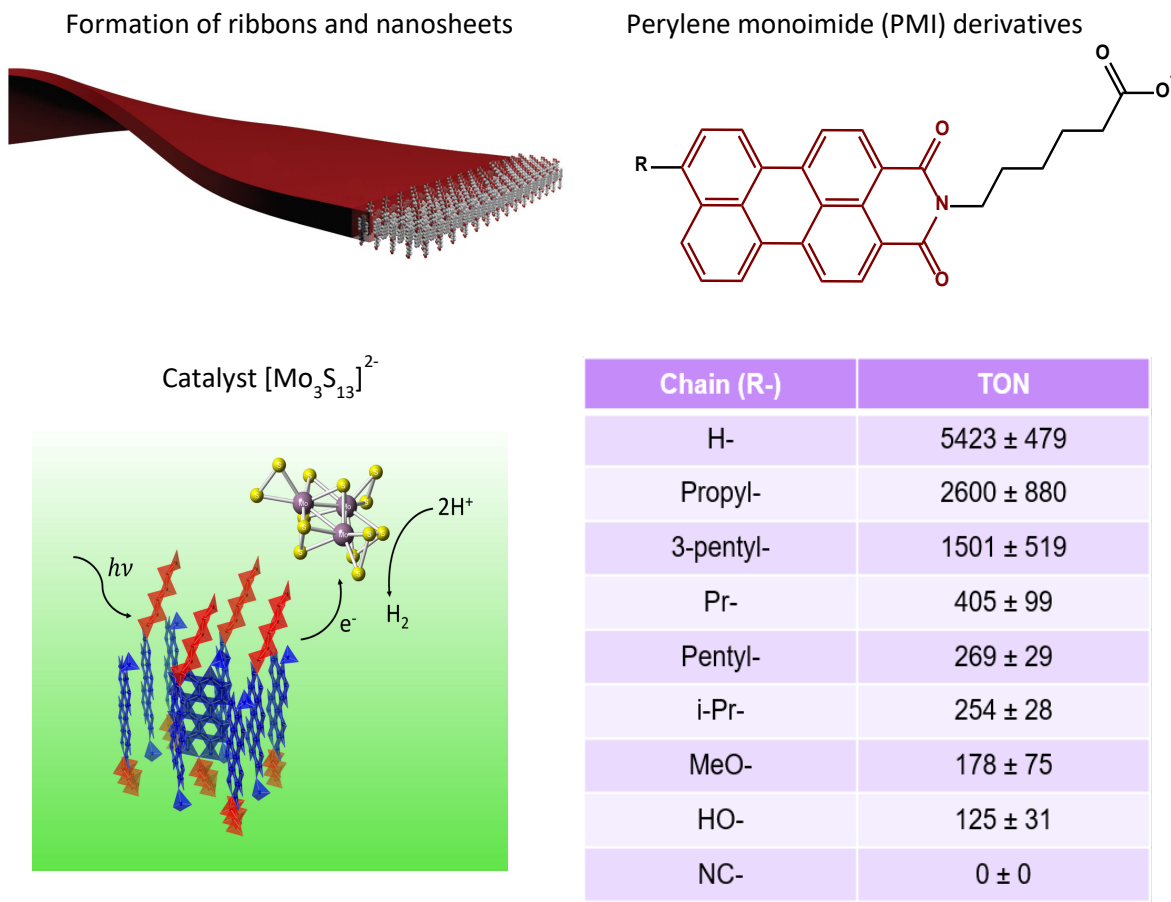


Figure 3.2. Schematic depiction of molecular and nano-structure of PMI system along with its catalytic efficiencies for various substituent groups. (Here turnover number (TON) is defined as the number of moles of H_2 produced divided by the number of moles of the catalyst ($[Mo_3S_{13}]^{2-}$) for 18 hours of irradiation. TOF is defined as TON / time of the irradiation).

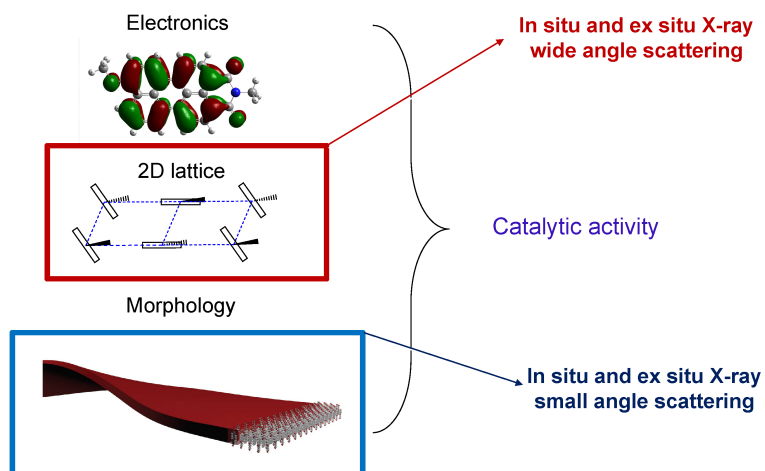


Figure 3.3. Hierarchy of structural scales affecting catalytic efficiency of PMI nanostructures.

In next section (3.2) we develop a scattering theory formalism and couple it with a simple geometrical model for the PMI molecules. We apply the formalism to a particular PMI chromophore: 9-methoxy-N-(sodium hexanoate) perylene-3,4-dicarboximide¹³ (MeO-PMI). Nanostructures formed by MeO-PMI exhibit fairly complex WAXS patterns. This generally applicable method fully reproduces the measured diffraction patterns, including the asymmetric line-shapes for the Bragg reflections and yields the molecular packing arrangement within a 2D crystal structure with a remarkable degree of detail. We find an approximate edge-centered herringbone structure for the PMI fused aromatic rings and ordering of the carboxypentyl chains above and below the nanosheets. Such a packing arrangement differs from the more symmetric face-to-face orientation of the unsubstituted PMI rings. This structural difference is correlated to our measurement of the reduced catalytic performance of MeO-PMI nanosheets as compared to the mesoscopically similar unsubstituted PMI assemblies. Furthermore, we investigate the light harvesting capacity and photocatalytic activity of this molecular assembly in solution with a transition-metal based catalyst. In Section 3.3 we will refine our model and apply it to various other PMI assemblies, some of which exhibit exceptionally high catalytic yields.

3.2. Investigation of MeO-PMI

3.2.1. Experimental Methods

Synthesis and catalysis. MeO-PMI was synthesized by Buchwald-Hartwig type coupling of 9-bromo-N-(methyl hexanoate)perylene-3,4-dicarboximide with dry methanol with subsequent hydrolysis by sulfuric acid (see Appendix A, 8.1). See Appendix A, 8.2 for $\text{Na}_2[\text{Mo}_3\text{S}_{13}]\cdot 5\text{H}_2\text{O}$ synthesis and Appendix A, 8.3 for hydrogen production experiments. All chemical synthesis and hydrogen production experiments were performed by Adam Dannenhoffer.

Wide-angle X-ray scattering (WAXS) and small-angle X-ray scattering (SAXS). X-ray measurements were performed at the DuPont-Northwestern-Dow Collaborative Access Team (DND-CAT) 5ID-D station at the Advanced Photon Source (APS). An X-ray energy of 12.00 keV corresponding to a wavelength of 1.033 Å was selected using a double-crystal monochromator. Data was collected simultaneously across three Rayonix CCD detectors. Sample to detector distances were 201 mm for WAXS, 1013 mm for MAXS, and 8500 mm for SAXS. The scattered intensity was recorded in the interval $0.002 < q < 3.147 \text{ \AA}^{-1}$. The wavevector transfer is defined as $q = (4\pi/\lambda) \sin(2\vartheta/2)$, where 2ϑ is the scattering angle. Exposure time was 1 second. Samples of 7.25 mM MeO-PMI were oscillated with a syringe pump during exposure to prevent beam damage. Background samples containing water or 50 mM NaCl were also collected in order to perform background subtractions.

Grazing-incidence wide-angle X-ray scattering (GIWAXS). Data was collected at APS station 8ID-E. The beam energy was 7.35 keV, sample-to-detector distance 212 mm, and the incident angle 0.2°. Samples were prepared by drop-casting 30 µL of MeO-PMI (7.25 mM) solution onto a clean glass substrate. The solutions were allowed to dry in air overnight. X-ray scattering was measured using a Dectris Pilatus 1M detector. 2D data were processed using GIXSGUI.¹⁴ Pixel-by-pixel corrections have been applied for Pilatus and Rayonix detectors: $I_{corrected} = I_{raw} \cdot E_m E_d F C_s P^{-1}$, where E_m and E_d are medium and detector efficiency correction (which includes absorption correction), flat-field correction F removes sensitivity variation among the pixels, C_s is the solid angle correction, P is the polarization correction, which is horizontal in these experiments.

Atomic force microscopy (AFM). AFM characterization was performed at Northwestern's NUANCE Facility using a Bruker Dimension ICON atomic force microscope at ambient conditions. Tapping mode was utilized with single-beam silicon cantilevers with nominal oscillation frequency of 300 kHz. Solutions of 7.25 mM MeO-PMI were spin-coated (10 µL) on freshly cleaved mica substrates at 2000 rpm.

Ultraviolet – Visible Absorbance Spectroscopy. Absorbance spectroscopy on chromophore amphiphile (CA) solutions (7.25 mM) was performed at the NUANCE Facility in a 0.05 mm path length, closed demountable quartz spectrophotometer cell (Starna Cells) using a Shimadzu UV-1800 Spectrophotometer.

Cryogenic transmission electron microscopy (Cryo-TEM). Cryo-TEM imaging was performed on a JEOL 1230 microscope at the NUANCE Facility, operating at 100 kV. A 6.5 μ L droplet of 8.7 mM MeO-PMI was placed on either a lacey carbon copper grid or C-flat grid (CF-4/2-4C-25, Electron Microscopy Science). The grid was held by tweezers mounted on a Vitrobot Mark IV equipped with a controlled humidity and temperature environment. The temperature was set to 24°C and humidity was held at 90%. The specimen was blotted and plunged into a liquid ethane reservoir cooled by liquid nitrogen. The vitrified samples were transferred to a Gatan 626 cryo-holder through a cryo-transfer stage cooled by liquid nitrogen. During observation of the vitrified samples, the cryo-holder temperature was maintained below -180°C. The images were recorded with a CCD camera.

3.2.2. Results and Discussion

MeO-PMI is bright red and fluorescent when dissolved in disassembling organic solvents such as DCM or DMSO, but appears brownish after assembly in water (Figure 3.4A). The absorbance of the monomer shows a broad featureless band centered around 520 nm, which undergoes a significant blue shift in water indicating the formation of a strongly H-aggregated species (Figure 3.4B, see also Appendix A, Figure 8.7). AFM imaging of MeO-PMI spin-coated on a freshly cleaved mica from aqueous solution reveals the presence of well-defined nanosheets with widths on the order of 100 nm and heights of roughly 2.0 nm (Figure 3.4C, D). Cryogenic transmission electron microscopy (cryo-TEM) confirms the sheet morphology

(Figure 3.4E). Solution SAXS data (Figure 3.4F) has a Porod slope of -2, characteristic of 2D objects^{2,15}, and minima corresponding to a 2.1 nm thickness, consistent with the AFM results.

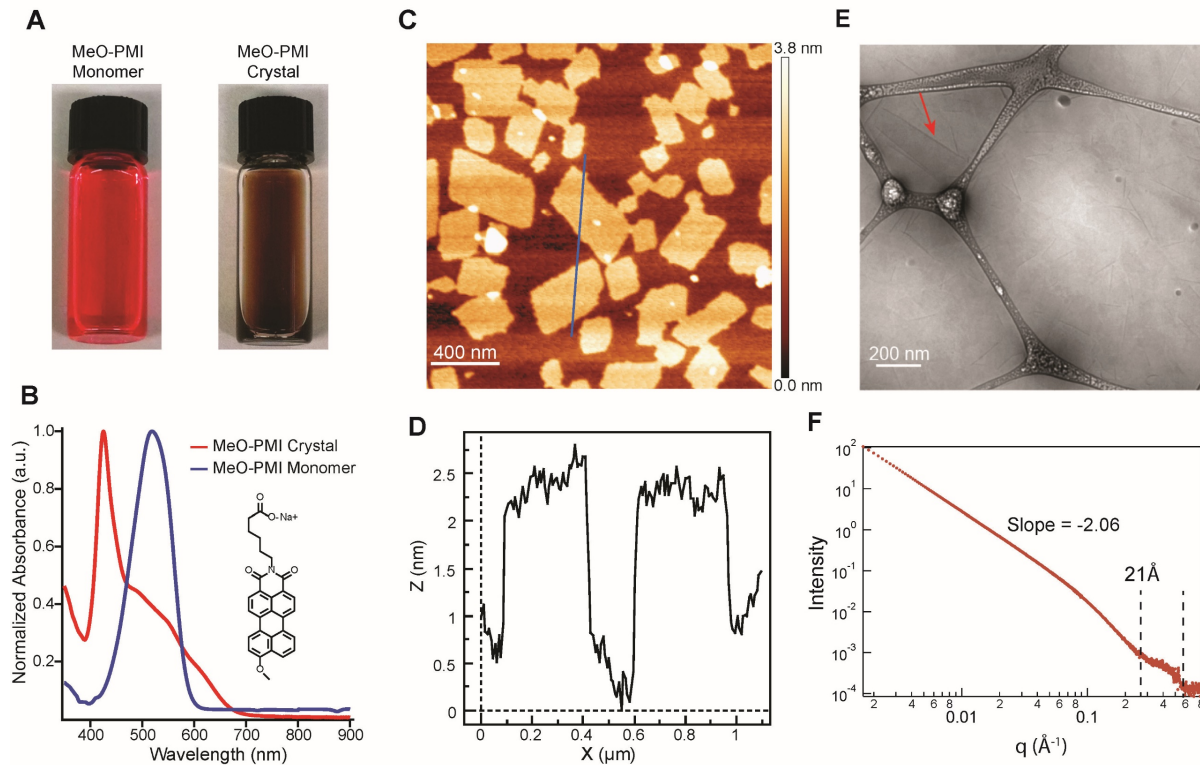


Figure 3.4. **A)** Pictures of vials containing 1 mM MeO-PMI monomer dissolved in DMSO (left), and assembled nanostructure in water (7.25 mM, right). **B)** Normalized UV-Vis absorbance spectra for MeO-PMI in DMSO (1 mM) blue, and in water (7.25 mM) red. **C)** AFM height mode image of MeO-PMI spin-coated from 8.7 mM aqueous solution onto freshly cleaved mica. **D)** Height line cut of AFM image in c (blue line). **E)** Cryo-TEM of 8.7 mM aqueous solution. **F)** SAXS data with Porod analysis and minima sensing the thickness of the nanosheets.

To evaluate the potential catalytic activity of MeO-PMI nanosheets, proton reduction samples were prepared by addition of a cationic polymer (polydiallyldimethylammonium chloride) to an 8.7 mM aqueous solution. A solution of sacrificial electron donor (1.7 M ascorbic acid) and 3.5 μ M Na₂[Mo₃S₁₃] · 5H₂O catalyst were added. The samples were subsequently purged with argon for 10 minutes and placed on an illumination source for 18 hours. The headspace of each vial was examined using gas

chromatography to determine the amount of hydrogen gas produced. The MeO-PMI produced 0.62 µmoles of H₂, which corresponds to a catalyst turnover number (TON) of 178 ± 75. MeO-PMI samples were compared to the previously studied system of unsubstituted PMI amphiphile which produced 5.85 µmoles of H₂ under the same experimental conditions, corresponding to an order of magnitude more H₂ produced and a TON of 1695 ± 314⁵. We attribute this difference in hydrogen production ability between PMI and MeO-PMI to different crystal structures formed by each species, as discussed later. It is known that the crystal packing of these photocatalytic materials greatly influences the hydrogen production by changing the materials ability to support long-lived excited states⁶. As such it is important to determine the different crystal structures adopted by various substituted and unsubstituted PMIs with a high degree of accuracy to better understand their effect on the material properties.

MeO-PMI nanosheets form 2D crystal lattices in freshly prepared solutions even without the addition of charge screening ions. This is a behavior different from the amphiphile with no substituent at the 9 position⁵ and can be attributed to a substantially larger electric dipole moment for the MeO-PMI monomer (see below). 2D MeO-PMI nanosheets exhibit multiple diffraction features both in the ex situ grazing incidence wide angle X-ray scattering (GIWAXS) of the drop-cast films on glass substrates, as well as in solution WAXS experiments. We develop a model, which reproduces all peaks in the GIWAXS and the WAXS diffraction patterns in peak position and intensity. Furthermore, the analysis replicates the asymmetric line shapes for the diffraction peaks from PMI assemblies in solutions, observed *via* WAXS. The unusual asymmetric peak shape was previously observed for diffraction from graphite flakes with small surface absorbed molecules, and is a characteristic for randomly oriented 2D crystals¹⁶⁻¹⁹. Our method extends the WAXS analysis to the case of assembly of large, complex molecules and allows extraction of structural information with a remarkable degree of detail not previously possible. It should be noted that solution WAXS contains all the information to reconstruct the 2D crystal structure and

analysis can be applied to it standalone, independent of the GIWAXS. We will proceed with the analysis of both cases in sequence.

PMI nanosheets lack the rigidity of 3D crystallites, making atom-by-atom diffraction refinement unfeasible. However, we demonstrate that it is possible to use slab models, which emulate reasonably well both the electron density distribution of the lattice basis, and degrees of freedom of modified PMI molecule. This assumption validates itself with excellent fits to the experimental data. As will be shown below, the identified structure is not what one would expect by simply juxtaposing π - π stacked PMI molecular threads side-by-side in rows, but rather an edge-centered herringbone lattice bearing resemblance to other organic herringbone structures observed in thin film²⁰ and single crystal diffraction²¹⁻²⁴.

The GIWAXS pattern of a drop-cast sample manifests rods parallel to the q_z axis (Figure 3.5A), a distinctive feature of 2D crystals lying flat on a substrate with crystal domains having an azimuthal rotational randomness. Intense spots along the q_z axis (centered at $q_r = 0$) indicate multilayering with a period of 20.6 Å (Figure 3.5A), close to the height of a single sheet revealed by AFM (Figure 3.4D) and SAXS minima (Figure 3.4F). The number of layers in a single specular domain, estimated by the Scherrer equation, is $N = 6$. However, this spacing period is dependent upon the evaporation conditions of drop-casting, and has been observed to vary between 20-25 Å. Spin-casting, which efficiently removes the water between the layers, yields a value of 20.5 Å (see Appendix A, 8.5).

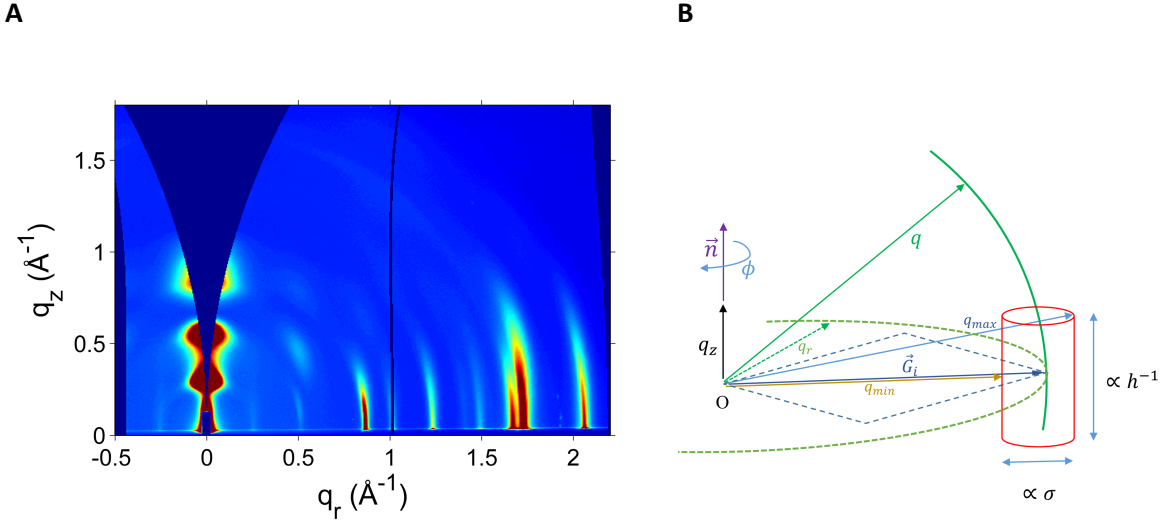


Figure 3.5. **A)** GIWAXS reciprocal space data of drop-cast dry sample. q_z is the out-of-plane component of the scattering vector and the in-plane component is $q_r = \sqrt{q_x^2 + q_y^2}$. **B)** Reciprocal space schematic representation of a form factor (red cylinder) at a particular reciprocal lattice vector \vec{G}_l . Parallelogram outlined by dashed blue lines represents unit cell in reciprocal space.

The diffraction condition for a particular reciprocal lattice vector \vec{G}_l is depicted on Figure 3.5b. The red cylinder shows schematically the Fourier transform of the electron density of the sheet in reciprocal space at a 2D lattice vector \vec{G}_l . Non-zero diffraction intensity results when scattering vector \vec{q} intersects the cylinder (generalized Laue condition). The diameter and height of this cylinder are restricted correspondingly by the domain size and the component of the form factor along the normal \vec{n} to the sheet (h is the height of the sheet). The latter gives rise to the rods in GIWAXS. To enforce rotational randomness of drop-cast sheets around normal \vec{n} , integration of intensity needs to be carried out only over azimuthal angle ϕ of vector \vec{q} , as rotation of the lattice at fixed \vec{q} is equivalent to fixing the lattice and rotating the vector \vec{q} . On the other hand, in solution WAXS, spherical randomness of nanosheets requires averaging over the solid angle (i.e. both over azimuthal and polar angles) which results in a mapping of the 2D GIWAXS information onto 1D diffraction pattern and coupling of lateral and specular information.

We start with formalizing the model for the GIWAXS data from the nanosheets. The in-plane line-cut through the data (Figure 3.6B, red line) at $q_z \approx 0$, where the scattering vector \vec{q} lies in the plane of the nanosheets, is only sensitive to the 2D projection of the (electron density) structure. From the experimental peak positions, the 2D lattice is determined to be oblique with lattice parameters $a = 12.41 \text{ \AA}$, $b = 8.95 \text{ \AA}$ and $\gamma = 89.5^\circ$ for MeO-PMI (see Appendix A, 8.4). From the assigned hk Miller indices (vertical dashed lines in Fig. 3b) one can see that peaks differing only in the sign of their $h \times k$ product (e.g. 3 1 and $\bar{3} 1$) have a small q separation. This small peak splitting would disappear if the unit cell were rectangular. However, fixing γ at 90° causes a 50% increase to the value of χ^2 generated by the numerical fitting procedures described below.

As depicted in Figure 3.6a the width of an individual PMI molecule is 6.6 \AA , while the estimate of $\pi\text{-}\pi$ stacking distance²⁵ is $\sim 4 \text{ \AA}$. This together with the lattice constants indicates that the basis (Figure 3.6C) of the 2D crystal structure (Figure 3.6D) consists of four molecules. After determining the lattice parameters from the peak positions, deducing the 2D crystal structure then reduces to the task of establishing the arrangement of molecules in the basis from analyzing the intensities and line shapes of the set of diffraction peaks.

The in-plane scattered intensity can be written in a form of the following integral (eq. 2.8):

$$I(q) \propto \sum_i \int_0^{2\pi} e^{-\frac{1}{2\sigma^2}(\vec{q}-\vec{G}_i)^2} |F(\vec{q})|^2 d\phi \quad (3.1)$$

where F is the form factor of the basis projected onto the plane of the nanosheet, and the summation is over reciprocal 2D lattice vectors \vec{G}_i . The latter is easily expressed in terms of unit cell parameters a , b , and γ . The first factor of the integrand is a result of a Gaussian approximation to the sum over repeated unit cells within a single domain, and is characterized by the spread σ , which is inversely proportional to

the domain size³. This factor imposes the in-plane width constraint in reciprocal lattice (diameter of the red cylinder in Figure 3.5B). For the mesoscale PMI assemblies in our case, σ is small. Therefore, the form factor of the molecule, with all dimensions less than 2 nm, does not substantially vary in the relevant integration space and can be pulled out of the integral, which then can be resolved analytically, yielding:

$$I(q) \propto 2\pi \sum_i e^{-\frac{1}{2\sigma^2}(q^2+G_i^2)} B_0\left(\frac{q G_i}{\sigma^2}\right) |F(\vec{G}_i)|^2 \quad (3.2)$$

where $B_0(x)$ is the modified Bessel function of the first kind. Since $\frac{q G_i}{\sigma^2} \gg 1$ for almost all of the WAXS region, an asymptotic expansion for the Bessel function, $B_0(z) \xrightarrow{z \rightarrow \infty} \frac{e^z}{\sqrt{2\pi z}}$, can be used, resulting in:

$$I(q) \propto \sum_i \frac{\sigma}{\sqrt{q G_i}} e^{-\frac{1}{2\sigma^2}(q-G_i)^2} |F(\vec{G}_i)|^2 \quad (3.3)$$

Since lattice vibrational effects in 2D systems make the Lorentzian distribution a better descriptor of the peak shape than Gaussian,²⁶⁻²⁷ we recast expression (3.3) as:

$$I(q) \propto \sum_i \frac{\sigma}{\sqrt{q G_i}} \cdot \frac{1}{1 + \frac{(q - G_i)^2}{\sigma^2}} \cdot |F(\vec{G}_i)|^2 \quad (3.4)$$

The Lorentz factor $\frac{1}{\sqrt{q G_i}}$ plays a significant role in WAXS data fitting when the q -range is large.

To construct a parametrized projected form factor F for basis we model each of the four PMI molecules with two rectangular solid boxes, a thin plate for the fused rings²⁸ and an narrow rod for the carboxypentyl chain pinned to the center of the top side of the plate. The form factors for the projections of the plate and chain oriented with their longer projected sides along the x-axis (i.e. side a of the unit cell) are correspondingly:

$$f_p(\vec{q}, \vec{l}_p) = n_p \operatorname{sinc}\left(\frac{q_x l_{p,x}}{2}\right) \operatorname{sinc}\left(\frac{q_y l_{p,y}}{2}\right) \quad (3.5a)$$

$$f_c(\vec{q}, \vec{l}_c) = n_c \operatorname{sinc}\left(\frac{q_x l_{c,x}}{2}\right) \operatorname{sinc}\left(\frac{q_y l_{c,y}}{2}\right) e^{\frac{i q_x l_{c,x}}{2}} \quad (3.5b)$$

where n_p and n_c are correspondingly the total number of electrons in the plate and carboxypentyl chain, \vec{l}_p and \vec{l}_c are the corresponding sizes of sides. Each of the four plates and rods are given an individual rotational angle α_τ around the normal \vec{n} to the 2D lattice sheet, which in the case of the rod, models the rotational freedom of the carboxypentyl group about the C-N σ bond. The fitted width of the plate indirectly accounts for the possible tilt of the molecule (polar angle to \vec{n} , Figure 3.5B). Hence, the basis form factor can be written in the following general form:

$$F(\vec{q}) = \sum_{\tau=1}^4 f_p[\hat{R}(-\alpha_{p,\tau})\vec{q}, \vec{l}_p] \cdot e^{i\vec{q}\vec{r}_\tau} + \sum_{\tau=1}^4 f_c[\hat{R}(-\alpha_{c,\tau})\vec{q}, \vec{l}_c] \cdot e^{i\vec{q}\vec{r}_\tau} \quad (3.6)$$

where α is the rotation angle of each individual plate and chain around the normal \vec{n} , \hat{R} is the 2D orthogonal rotation matrix around normal \vec{n} , r_τ are the positions of four molecules of the basis with respect to the origin of the latter. Ab-initio DFT (B3LYP) optimization with 6-31G basis for the plate (MeO-PMI with carboxypentyl group replaced by methyl; see Appendix A, 8.9) indicates a large dipole moment of 8.6 D, thereby strongly favoring an anti-parallel arrangement of neighbors. As a comparison, an amphiphile with no substituent at the 9 position has a dipole moment of 6.7 D. This effect is due to the electron donating ability of the methoxy group to the aromatic system.

The obtained analytical expression for the scattering intensity (eqs. 3.4 and 3.6) facilitates numerical fitting procedures by allowing deployment of not only local, but also global optimization techniques, such as Random Search²⁹ and Differential Annealing³⁰ methods. Figure 3.6B shows the fit to the experimental

data with rotational angles and plate width as the sought out fitting parameters (the sides of the rods were fixed to be 1.8 Å (the H-H distance) and 4.8 Å (the projected length of carboxypentyl chain)).

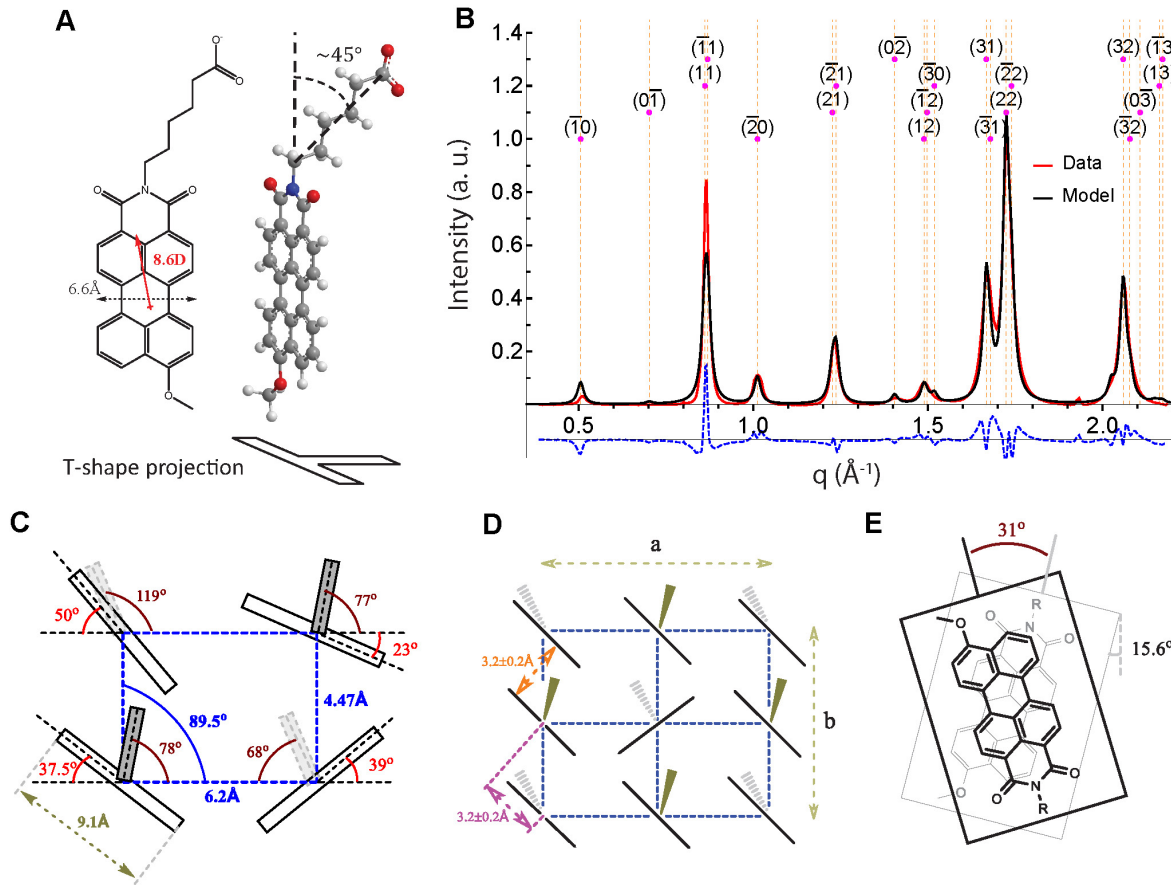


Figure 3.6. **A)** T-shape projection model of the MeO-PMI. Red arrow indicates dipole moment. **B)** in-plane line-cut of GIWAXS data and model fit to the data with $R^2 = 0.952$. (See Figure A9 for log plot.) Miller indices of diffraction peaks are also shown. Blue dashed line indicates the difference between data and model fit. It is offset for clarity. **C)** Projection of the basis onto the plane of the 2D sheet with selected parameters values determined from the analysis. Longer outlined rectangles represent the perylene fused rings, solid rectangles the carboxypentyl chain above the 2D plane and faded rectangles below, **D)** idealized unit cell with solid and dashed wedges representing carboxypentyl chains above and below the plane of the sheet, correspondingly, **E)** tilt angles of $\pi-\pi$ stacked perylenes (longitudinal and transverse shifts are not shown).

Figure 3.6C depicts the obtained angles and plate width. Figure 3D shows the idealized unit cell where inferred angles were equalized within $\pm 10^\circ$ margin to demonstrate the closest most symmetric 2D lattice, which for the plates is an edge-centered herringbone structure. The inferred π - π stacking distance and transverse shift are both $3.2 \pm 0.2 \text{ \AA}$ (Figure 3.6D, orange and purple arrows, respectively). Moreover, the chains themselves arrange in symmetric lattices both above and below the plane of the sheet. This latter ordering further manifests itself in a spot on the GIWAXS pattern (Figure 3.5A) at $q_r = 0.5 \text{ \AA}^{-1}, q_z = 0.45 \text{ \AA}^{-1}$, corresponding to in-plane spacing $\frac{2\pi}{0.5} = 12.6 \text{ \AA}$ and polar angle $\tan^{-1}\left(\frac{0.45}{0.5}\right) = 42^\circ$, in good agreement with $a = 12.4 \text{ \AA}$ and $180^\circ - \angle N-C-(C_4H_8COO^-) = 45^\circ$ (Figure 3.6A,D, see Appendix A, 8.8). Carboxyalkyl chains can affect the geometry of approach of the catalyst to the stacked aromatic rings, which carry the propagating photogenerated electrons.

Simpler models, which either do not take chains into account or fix chain-plate angles, fail to reproduce the combined intensity of the (31) and ($\bar{3}1$) peaks (see Appendix A, 8.12 and 8.13). The emergence of a faint rod at $q_r = 0.25 \text{ \AA}^{-1}$ in Figure 3.5A, corresponding to a doubling of lattice constant a , indicates a small distortion that if accounted for would result in further doubling of the basis. However, our model does not consider these effects to avoid overfitting with too large of a number of parameters.

The obtained projected width of 9.1 \AA is significantly larger than the actual 6.6 \AA width of PMI as a result of tilting of the molecule. The computed tilt angle from geometrical sizes of the molecules, is 15.6° , therefore the rotational angle between two stacked molecules is 31° (Figure 3.6E) which is in good agreement with single crystal diffraction and computational results on cognate compounds^{25, 31-33} (see Appendix A, 8.8).

Compared to the above described GIWAXS, the peaks in the solution WAXS experiments for 2D lattices exhibit only slightly shifted peak positions, but have characteristic asymmetric line-shapes arising from

the 3D randomness of the orientation of the nanosheets²⁶ (Figure 3.7). This is mathematically equivalent to solid angle averaging of rods located at 2D reciprocal lattice vectors \vec{G}_i . Figure 3.5B gives a qualitative understanding of the phenomenon: as the magnitude of \vec{q} increases, the $|\vec{q}| = \text{const}$ sphere intersects the non-zero form factor region (red cylinder, q_{\min}) and scattering intensity starts to rise sharply as both the form factor (due to movement toward the reciprocal lattice point \vec{G}_i) and the surface area cut by the cylinder increase. The width of the rise, which is of the order of σ contains the information regarding the domain size. After passing the maximum point (which is not necessarily at G_i because of the combination of the mentioned two factors), a long tail emerges, even beyond $G_i + \sigma$, as there are still corners of the cylinder with higher q_z values that intersect the $|\vec{q}| = \text{const}$ sphere. Therefore, the decrease of scattered intensity in the tail is both due to moving away from the G_i position as well as the reduced form factor at higher q_z . It is possible to show that peak shift and high- q tail width are non-linear combinations of h and σ , with only a weak dependence on G_i (see Appendix A, 8.7). Spherically averaged intensities for solution WAXS can be expressed as:

$$I(q) \propto \sum_i \int_0^{2\pi} \int_0^\pi e^{-\frac{1}{2\sigma^2}(\vec{q}-\vec{G}_i)^2} |F(\vec{q})|^2 \sin \theta d\theta d\phi \quad (3.7)$$

where angle θ is the polar angle of \vec{q} with respect to normal \vec{n} . If in solution there is a preferential orientation of nanosheets (e.g. because of solvent flow through a narrow capillary) the integration range of ϕ and θ would be arcs (possibly weighted) smaller than 2π and π , respectively. However, by assuming that the domains are sufficiently large, the exponential factor will essentially confine the non-vanishing region of the integrand within the tight vicinity of the reciprocal lattice vector, thereby allowing the extension of the integration limits to those in eq. (3.7). Within that region the in-plane variation of the form factor F can be neglected, resulting in:

$$I(q) \propto \sum_i \int_0^{2\pi} \int_0^\pi e^{-\frac{1}{2\sigma^2}(\vec{q}-\vec{G}_i)^2} |F(\vec{G}_i, q_z)|^2 \sin \theta d\theta d\phi \quad (3.8)$$

We carry out the ϕ integration as before, reducing the integral to only an integration over θ . The out-of-plane resolution of solution WAXS does not allow refinement of density profile along the normal \vec{n} in sufficient detail to distinguish between the perylene plate and carboxypentyl chain, hence one can use a single slab model to describe the electron density profile along the normal \vec{n} , which is a simple *sinc* function in reciprocal space as in eqs. (3.5). This simplifying assumption decouples projected and normal components of the form factor, resulting in:

$$I(q) \propto \sum_i |F_{\parallel}(\vec{G}_i)|^2 \int_0^\pi e^{-\frac{1}{2\sigma^2}(q \sin \theta - G_i)^2} \sigma \sqrt{\frac{2\pi \sin \theta}{G_i q}} |F_{\perp}(q \cos \theta)|^2 d\theta \quad (3.9)$$

where F_{\parallel} is given by eq. (3.6) and $F_{\perp}(q) = \text{sinc}\left(q \frac{h}{2}\right)$ where h is the electron density weighted height of the sheet. The integration in eq. (3.9) can be performed numerically by using algebraic summation procedure to make it computationally efficient for multi-parameter fitting (see Appendix A, 8.9). Figure 3.7A shows the fit to the solution WAXS experimental curve for MeO-PMI. The obtained angles are in agreement with our GIWAXS analysis, however the lattice is slightly larger: $a = 12.88 \text{ \AA}$, $b = 9.24 \text{ \AA}$, $\gamma = 89.8^\circ$ which can be attributed to electrostatic screening of charges and dipoles in water and increased entropy of the system.

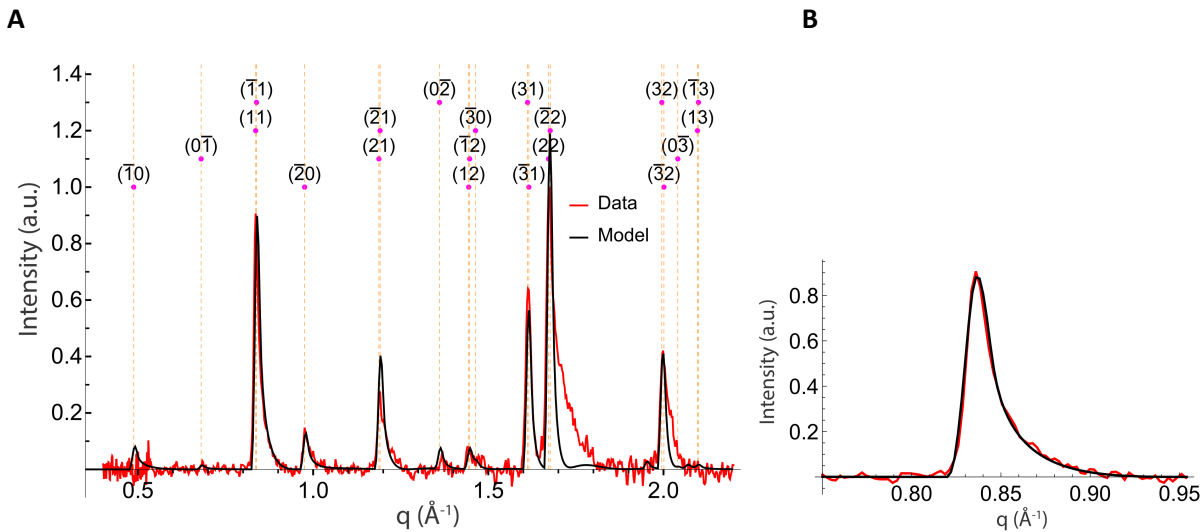


Figure 3.7. **A)** Solution WAXS experimental and fitted curves with peaks indexed for full range of q values. **B)** Expanded view of the (11) peak along with the fit.

The domain size estimate, by the Scherrer formula³, for the sheets in solution is substantially larger than that in drop-cast form, 456 \AA vs 274 \AA , pointing to a high level of stability of MeO-PMI 2D sheets in solution. The fitted thickness of the sheet is 14 \AA , a value smaller than 21 \AA obtained by SAXS and GIWAXS. This is due to the fact that carboxypentyl chains are half as dense in numbers per unit area on each side of the sheet because of anti-parallel geometry of perylene plates (WAXS senses electron density weighted average height in our model), and also due to the hydrated cationic counterion spacer in-between the 2D layers which is present in drop-casted film for GIWAXS, but is not crystallographically correlated with the 2D lattice to make it contribute to solution WAXS. Overall, the presented general approach for 2D molecular crystals reveals the molecular packing in the MeO-PMI assemblies. In particular, we show that the fused aromatic ring plates pack in an edge-centered herringbone lattice, which is substantially different from the face-to-face packing arrangement of these planes in assembly of unsubstituted PMI.

This difference is likely the origin of the reduced hydrogen production in the presence of MeO-PMI as compared to the case of unsubstituted PMI, as discussed next.

The general principle of the photoactivity of the PMI-based assemblies involves absorption of a photon to create a bound electron-hole pair on the same molecule [Frenkel exciton (FE)], which subsequently undergoes charge separation such that the electron and hole reside on different molecules (Figure 3.8). The hydrogen production is mediated by the relocation of the photogenerated electrons *via* these charge separated excitons to the proton reducing catalyst ($\text{Na}_2[\text{Mo}_3\text{S}_{13}]\cdot 5\text{H}_2\text{O}$). The charge transfer between adjacent PMI molecules depends upon the extent of nearest neighbor HOMO-HOMO and LUMO-LUMO overlaps, which are quantified by the charge transfer integrals for electron and hole, t_e and t_h .^{6, 34-35} The distortions from the face-to-face parallel stacking (unsubstituted PMI) to the transversely shifted nearest neighbor arrangements (MeO-PMI) should render these overlap integrals small, and possibly of opposite signs, thereby also reducing the width of charge separated (CT) band of states which is of the order of $4|t_e + t_h|$. Furthermore, the narrow and blue shifted peak in the UV-vis spectrum (Figure 3.4b), which is without accompanying red shifted secondary peak, in contrast to PMI, suggests that the ratio of the energy separation between FE state and CT band of states to the width $4|t_e + t_h|$ is larger for MeO-PMI than for PMI². This reduces the mixing between the CT band of states and FE state, thereby preventing efficient charge separation and as a consequence, lowers the catalytic activity of MeO-PMI scaffold.

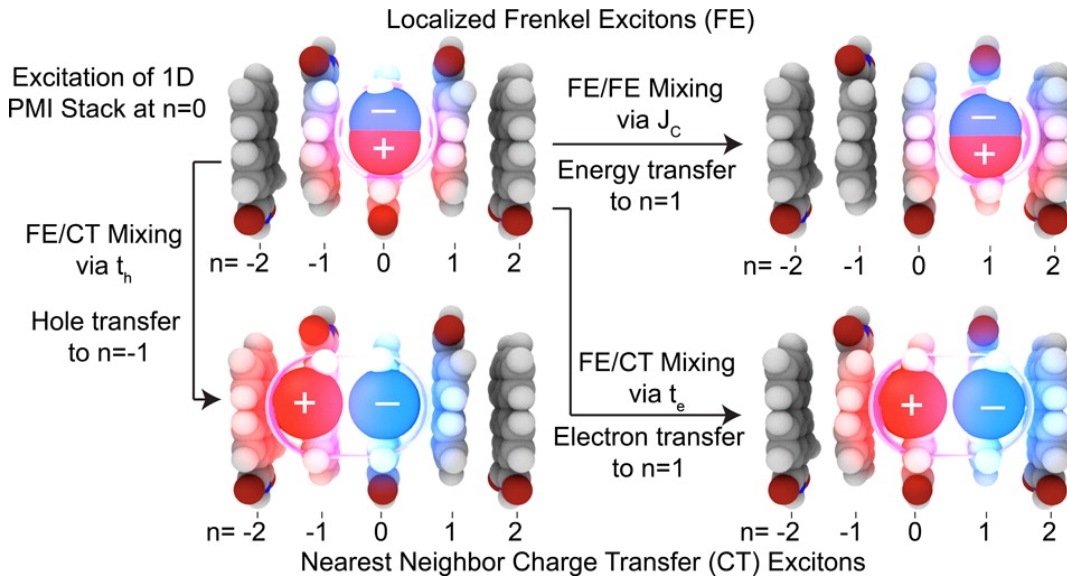


Figure 3.8. Graphical illustration of FEs and CTEs in PMI systems. A FE localized at $n = 0$ is shown in the top left corner. This FE can directly couple to a variety of FE and CTE states through the various matrix elements J_c , t_e , and t_h . For example, the exciton can transfer to site $n = 1$ via the long-range excitonic coupling J_c , as shown in the top right corner. The exciton can also dissociate via the charge transfer integrals t_e and t_h . As shown in the lower left corner, t_h facilitates hole transfer to a neighboring site while the electron remains at the parent molecule. The analogous processes for electron transfer is facilitated by t_e , as illustrated in the lower right corner. Note that the charge transfer process can repeat to yield larger-radius CTEs (reprinted with permission from Hestand, et al.⁶).

3.3. Accounting for the second chain

Existence of the second shorter chain at the 9th position of PMI can further contribute to lattice symmetry breaking and doubling of the unit cell, as noted above. To account for this effect, we model the short chain as a small sphere with the same number of electrons as the chain itself, placed at a location corresponding to the 9th position. To write the form factor of the lattice basis we must first deduce from geometrical considerations the coordinates of the attachment point of this chain on the in-plane projection of the electron density of tilted PMI molecule (Figure 3.9A and B depict the 2D model of the PMI molecule and its projection, respectively). From geometric sizes of rigid PMI plate we can estimate s

and h (Figure 3.9C and D) as 6.6 Å and 10.3 Å. In the following derivations we will assume that molecular tilt is not very large (typically less than 30°) and therefore drop all second order terms, including the product of azimuthal and polar tilts. We can express the tilt angle γ through the constants s and h and fit parameters l and w , as following:

$$\gamma = \arcsin l/d - \arcsin s/d \quad (3.10)$$

where $d = \sqrt{s^2 + h^2}$. The shift of the attachment point of the carboxypentyl group with respect to the center of the in-plane projection of perylene plate then becomes: $\Delta s = h/2 \sin \gamma$, while the shift of the short chain $l_0 = sf \cos \gamma + h \sin \gamma$. From Figure 3.9C we have:

$$\Delta s_c = h/2 \sin \gamma + l_w/2 \sin \alpha_{c,\tau} \quad (3.11a)$$

$$\Delta h = l + w/2 \cos \alpha_{c,\tau} - w/2 \quad (3.11b)$$

By using these expressions to account for phase shifts (exponential factors below), we can write the form factor of the in-plane projection of PMI electron density (with x axis passing through the plate center and aligned parallel to l side) as the following:

$$f_\tau(\vec{q}, l, w, \alpha_{c,\tau}) = n_{sp} e^{-i(l_0(l) - l/2)q_x + iq_y w/2} + f_p[\hat{R}(-\alpha_{p,\tau}) \cdot \vec{q}, l, w] \cdot e^{i\Delta s_c(l)q_x + i\Delta h(l,w)q_y} \quad (3.12)$$

where n_{sp} is the number of electrons on the short chain, while f_p is given by expression (3.5c). Expression 3.6 for the projected form factor of the basis then can be recast as:

$$F(\vec{q}) = \sum_{\tau=1}^n f_\tau[\hat{R}(-\alpha_\tau)\vec{q}, l, w, \alpha_{c,\tau}] \cdot e^{i\vec{q}\vec{r}_\tau} \quad (3.13)$$

where n is the number of molecules in the basis (typically either 1, 2 or 4). Notice, angles $\alpha_{c,\tau}$ of the carboxypentyl chains are defined with respect to the long side of the projection of the perylene plate, hence they will change accordingly when the entire molecular system is rotated by α_τ . The final expression (3.13) will be used in fitting the model to the experimental data under various restrictions on the parameters due to physical considerations.

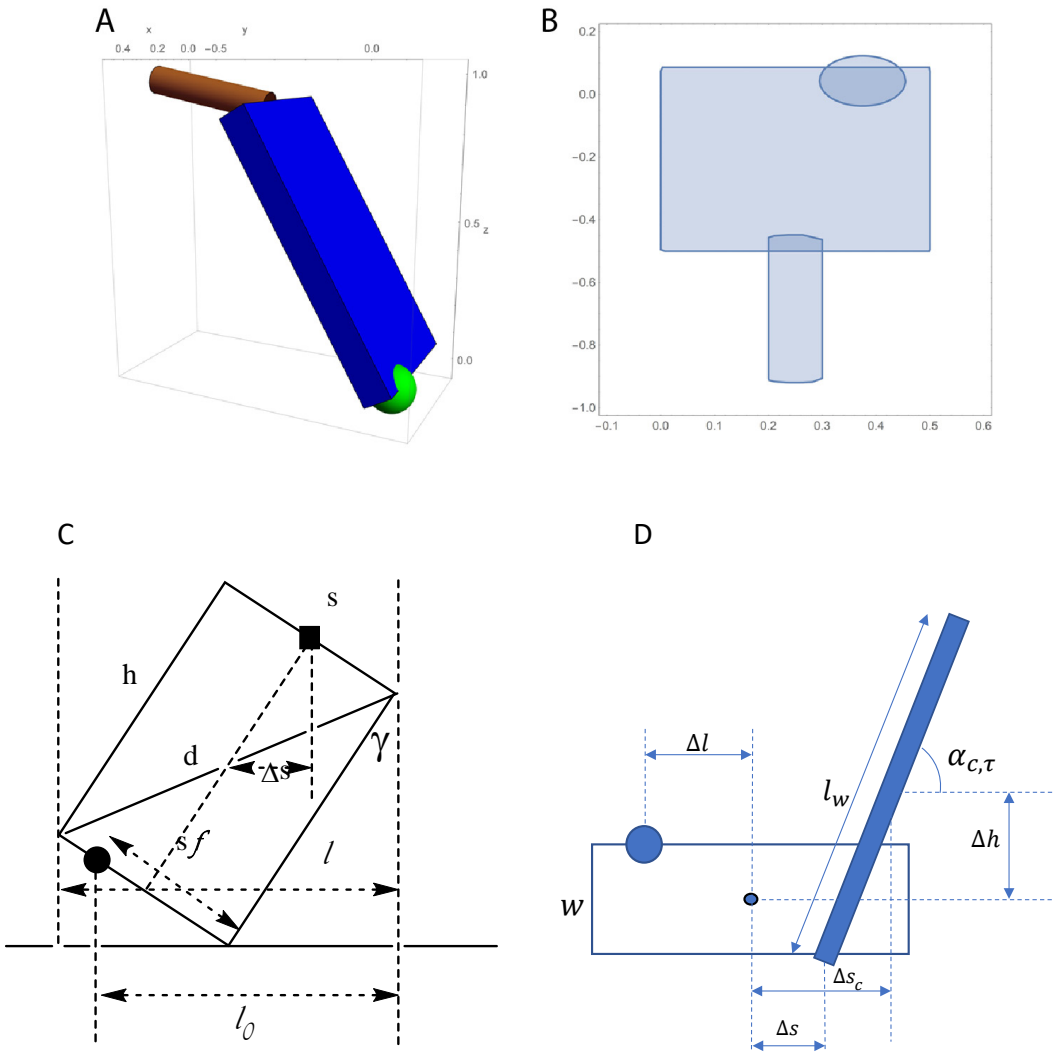


Figure 3.9. **A)** 3D slab model of the electron density of PMI molecule. Green sphere models the short chain, while brown cylinder the carboxypentyl chain, **B)** in-plane projection of the electron density, **C)** side view of the electron density (solid square corresponds to the attachment point of the carboxypentyl group, while the solid circle to the short chain at position 9), **D)** top view of the model.

3.3.1. Applications

The technique developed above for MeO-PMI and further refined by introduction of the 9th position chain model, can be applied to other PMI systems of less complex diffraction pattern. The model best reproducing experimental data with minimum number of parameters within physically meaningful parameter space have been selected. For the systems presented below, we model the molecule of perylene derivative as an orthorhombic slab of uniform density with a rod attached to the center of its upper edge, and a point charge on the lower edge at a quarter side distance from a corner of the slab (the green sphere on the Figure 3.9A). Slabs were initially oriented with their longest dimension along the z-axis, perpendicular to the plane of the sheet, and with a free rotational angle about this axis. The rod sizes were fixed so that the projection on xy plane was 4.8 x 1.8 Å rectangle. Varying projected sizes of the slab itself on xy plane implicitly account for the tilts of the molecule with respect to z axis (Figure 3.9B). The basis of the lattice typically consists of four molecules in almost all systems considered in the following. Molecules, aligned along the shorter side, were assigned equal rotational angle to ensure π-π parallel stacking. The model-based scattered intensity was fitted by the Levenberg–Marquardt algorithm to the background subtracted WAXS experimental data to extract the rotational angles, slab projected widths and the offset.

3.3.1.1. HO-PMI

Though catalytic performance of HO-PMI is similar to MeO-PMI (table in Figure 3.2), its lattice structure and molecular packing exhibits higher level of symmetry. This can be immediately inferred from simpler diffraction pattern. Figure 3.10 shows the fit to the data which reproduces the diffraction pattern almost perfectly. Nanosheets in solution have slightly larger angle between the plate and the carboxypentyl chain. This can be attributed to solvent effects as chains are negatively charged.

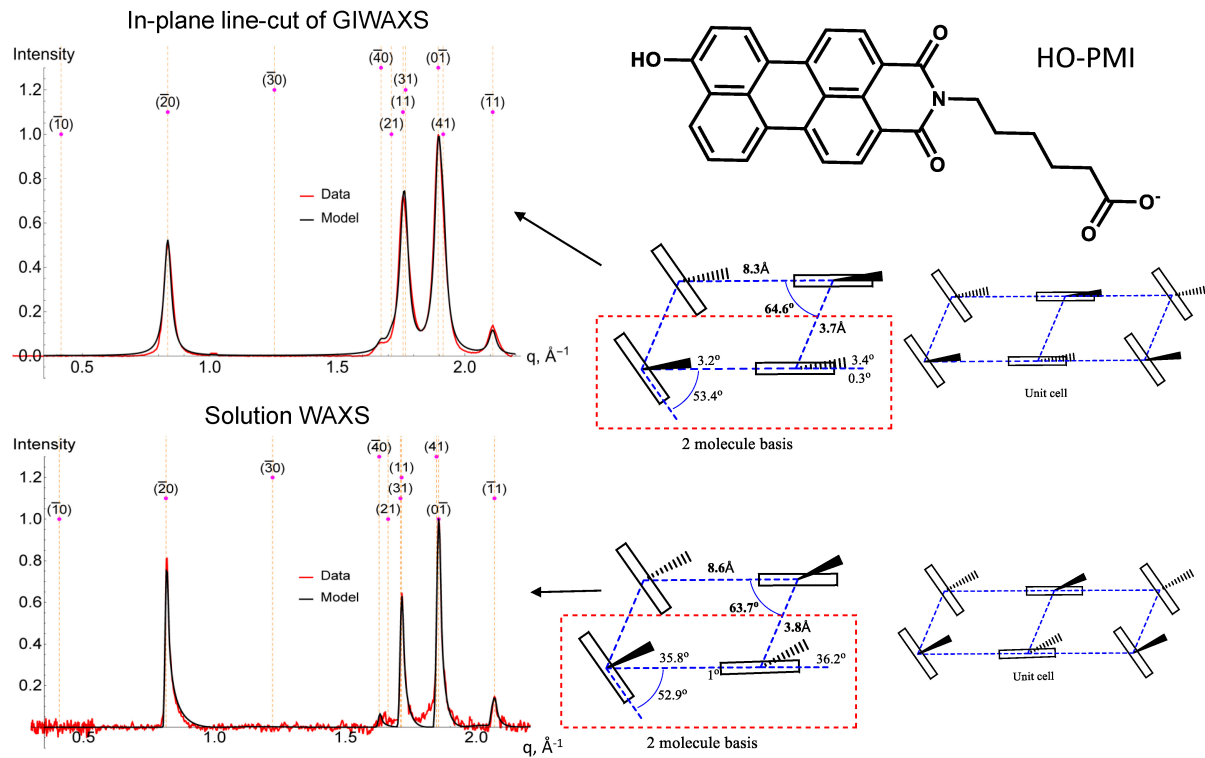


Figure 3.10. WAXS patterns, best fits and inferred molecular packing of HO-PMI. Basis and unit cell are depicted for projection of electron density on the plane of the sheet.

3.3.1.2. Alkylamino-PMIs

We investigate propyl-, isopropyl-, *n*-pentyl-, and 3-pentyl- amino-PMIs homologs. These systems form 2D crystals in water even without addition of salt, presumably caused by enhanced dipole moments due to the presence of amino group. Their diffraction patterns in solution and on drop-cast dry films exhibit substantial differences (Figure 3.11, Figure 3.12). However, it was not possible to identify a single 2D lattice that would reproduce the positions of all peaks with an exception of 3-pentylamino-PMI. This might be indicative of multiphase system.

3-pentylamino-PMI had markedly distinct characteristics. Only after annealing did it exhibit diffraction features. Figure 3.14 shows the solution WAXS pattern alongside its best fit and the inferred unit cell. We

restricted the angle between the plate and the carboxypentyl chain to be 90° . The obtained $4.9 \text{ \AA} \times 7.1 \text{ \AA}$ in-plane projected widths of the perylene plate (parameters l and w in the expression 3.13) (Figure 3.9D) indicate 28.5° declination with respect to the normal to nanosheet (polar angle of the plane of the nanosheet) (Figure 3.14D) and only negligible tilt towards side a ($a = 11.4 \text{ \AA}$, $b = 7.1 \text{ \AA}$, and $\lambda = 106.8^\circ$). It was possible to grow single crystals of 3-pentylamino PMI with chloroform inclusions by evaporating a solution of 3:1 chloroform/methanol. Figure 3.13 shows the side views of a fragment of the crystal and the arrangement of two stacked molecules. This single crystal structure is matching closely the WAXS inferred structure, with the only difference being the lack of tilt for the nanoribbons in solution.

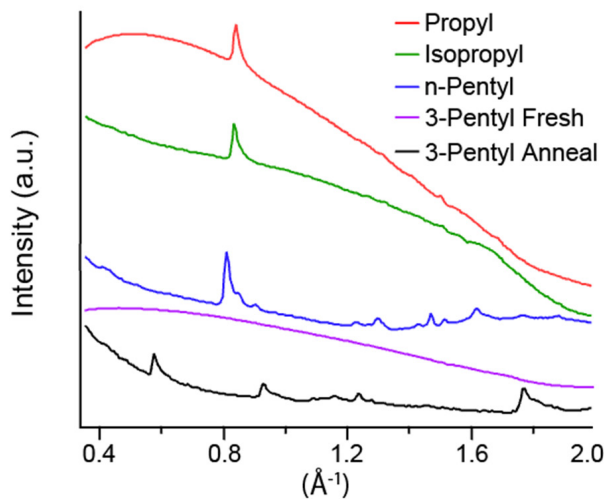


Figure 3.11. Solution WAXS patterns of alkylamino-PMIs. Water background scattering is not fully subtracted (provided by Adam Dannenhoffer).

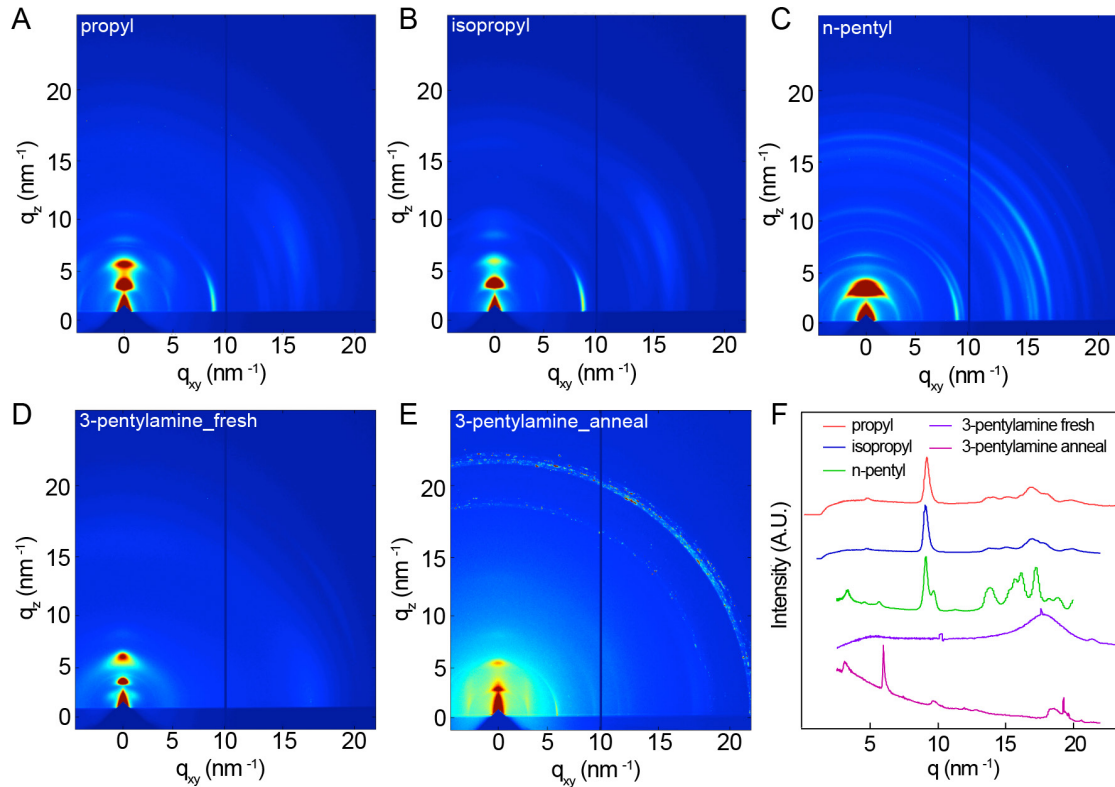


Figure 3.12. GIWAXS patterns for **A**) propyl, **B**) isopropyl, **C**) pentyl, **D**) 3-pentylamine fresh, **E**) 3-pentylamine anneal. **F**) Horizontal line-cuts for each data set (provided by Adam Dannenhoffer).

3-pentylamino PMI upon heating gives rise to a strong red shifted peak in UV-vis spectrum which is absent for other alkylamino PMIs. This transition is irreversible, and the peak does not disappear upon cooling (Figure 3.15). Theoretical work has attributed this to mixing of charge transfer states (CT) and transition dipole moments (TDM)^{6,36} and presence of highly mobile excitons able to dissociate and diffuse through the nanoribbon. Hydrogen production was almost 3 times higher for crystalline 3-pentylamino PMI compared to all other alkylamino-PMIs (including non-crystalline form of 3-pentylamino PMI), reaching TON = 1501±519 (Figure 3.16). These considerations indicate the importance of molecular packing in its effect on TDM/CT mixing and the design of light absorbing supramolecular scaffolds.

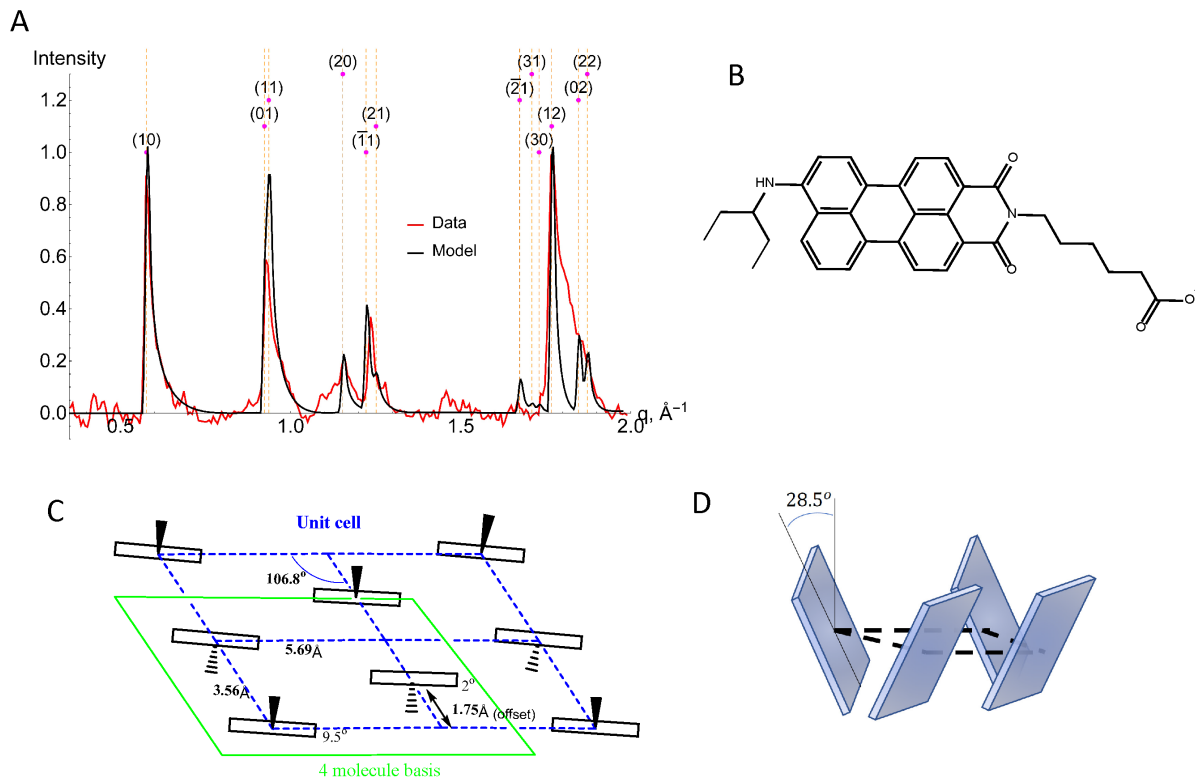


Figure 3.14. **A)** Background subtracted WAXS data and model fits for 3-pentylamine PMI. The model is described by a basis set of 4 molecules that occupy a quadrant (parallelogram shown in **C**) of the oblique 2D unit cell (**C**) with lattice parameters a and b being twice the edge lengths of the basis set parallelogram shown above. The listed (hk) indices are for $a > b$. **D)** Deduced declination angle of the perylene slab with respect to the normal to nanosheet plane.

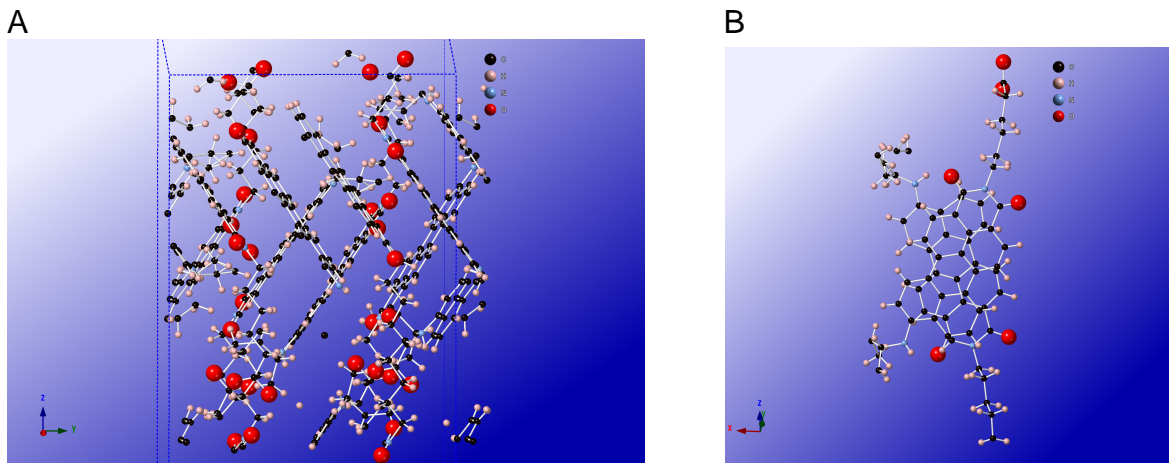


Figure 3.13. Side views of grown single crystal of 3-pentylamino-PMI (orthorhombic symmetry group: $P\ b\ c\ a$; $a = 23.97\text{\AA}$, $b = 16.51\text{\AA}$, $c = 35.32\text{\AA}$).

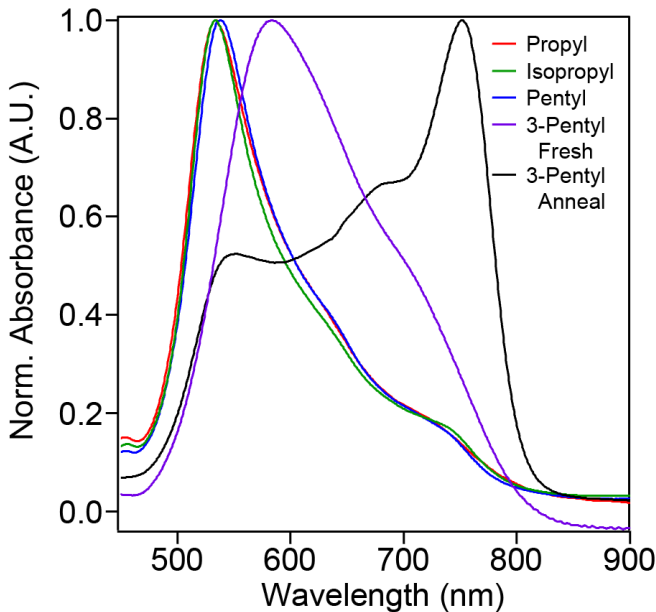


Figure 3.15. Absorbance spectrum of fresh, amorphous 3-pentyl CA (purple trace) in comparison to its crystalline form and the other three chromophores. All traces taken at 7.25 mM (provided by Adam Dannenhoffer).

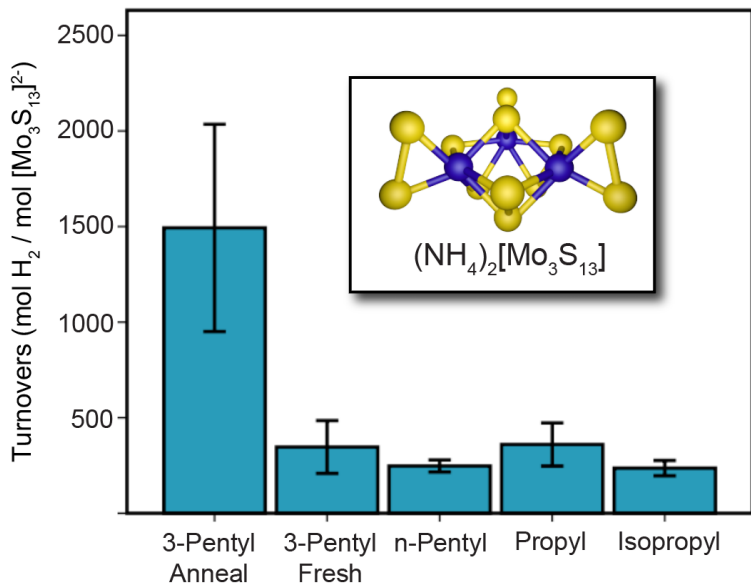


Figure 3.16. Photocatalytic hydrogen evolution experiments for propyl, isopropyl, n-pentyl, fresh 3-pentyl, and annealed 3-pentyl nanostructures gelled with poly (diallyl dimethylammonium) chloride in the presence of ascorbic acid (sacrificial donor) and a molybdenum sulfur cluster. No H₂ was observed if the nanostructures, ascorbic acid, or molybdenum cluster was not present. (Provided by Adam Dannenhoffer.)

3.3.1.3. Phase transition in *n*-C₃H₇-PMI

Thermodynamic stability oftentimes is the guiding force for self-assembly of various organic monomers and is well investigated in many systems³⁷⁻³⁸, especially those relevant in biological setting. However, many unanswered questions remain on kinetic barriers of their formation³⁹⁻⁴². Existence of certain systems can be primarily dictated by kinetic factors⁴³⁻⁴⁷. Here we study a rare case of phase transition in amphiphilic supramolecular nanostructures⁴⁸⁻⁵¹, i.e. phase transition of n-C₃H₇-PMI (T3-PMI) nanoribbon in water⁵². This compound dissolves in water with formation of red solution of long narrow ribbons (~200nm by cryo-TEM), which, upon addition of 50mM NaCl, change the color to pale orange and form ~400 ± 90 nm long nanoribbons (Figure 3.17A-D). This change is accompanied by transformation of featureless solution WAXS pattern to the one with clearly defined asymmetric diffraction peaks (Figure 3.17E). NaCl reduces the Coulombic repulsion between negatively charged PMI molecules and allows crystallization and lateral growth. Gradual heating of the solution to 80°C leads to darkening of the color (Figure 3.17B) and alteration of the diffraction pattern (Figure 3.17E). Cryo-TEM reveals a formation of nanosheets of scroll morphology (we call it β-phase) (Figure 3.17D). The scrolls manifest themselves in oscillations on SAXS curve (Figure 3.18).

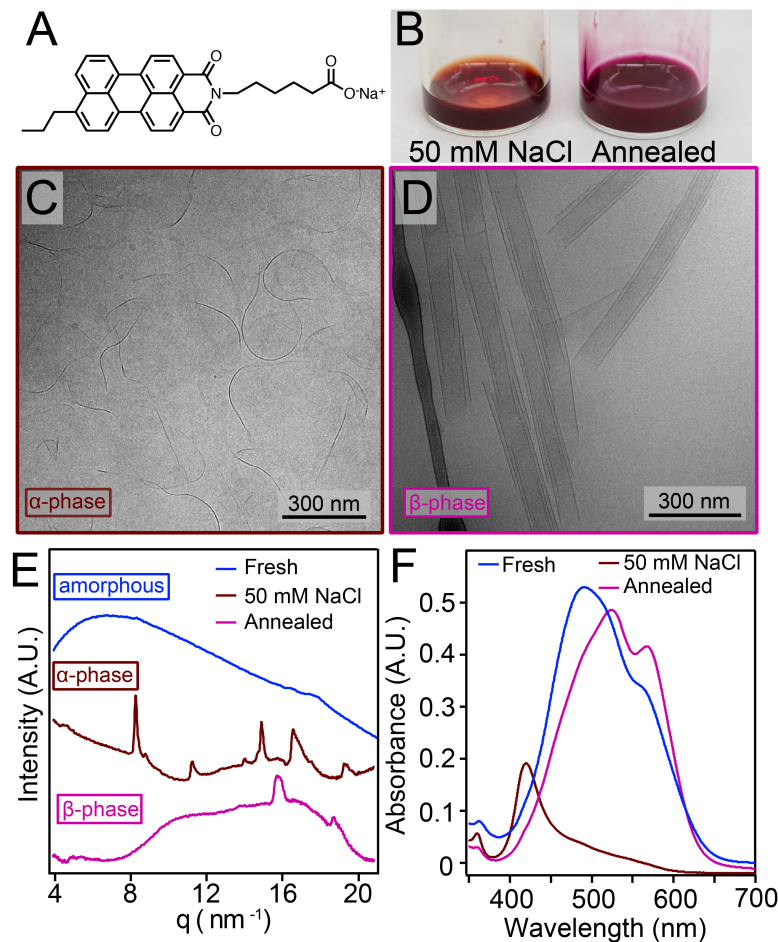


Figure 3.17. **A)** Molecular structure of T3-PMI chromophore amphiphile, **B)** photographs of 7.25 mM T3-PMI solution with 50 mM NaCl before (left) and after (right) annealing, **C)** cryo-TEM of 7.25 mM T3-PMI with 50 mM NaCl showing ribbons 15 ± 4 nm wide, **D)** cryo-TEM of annealed T3-PMI solution revealing scrolls of 90 ± 13 nm wide, **E)** solution WAXS patterns of freshly dissolved, 50 mM NaCl, and annealed solution of T3-PMI, **F)** absorbance spectra of freshly dissolved T3-PMI with a maximum at 490 nm and a shoulder at 558.5 nm, 50 mM NaCl (α -phase) with a blue shifted absorbance maximum at 420 nm, and the annealed (β -phase) with a maximum at 523 nm and a new feature at 565 nm. (Adapted from Kazantsev, et al.⁵².)

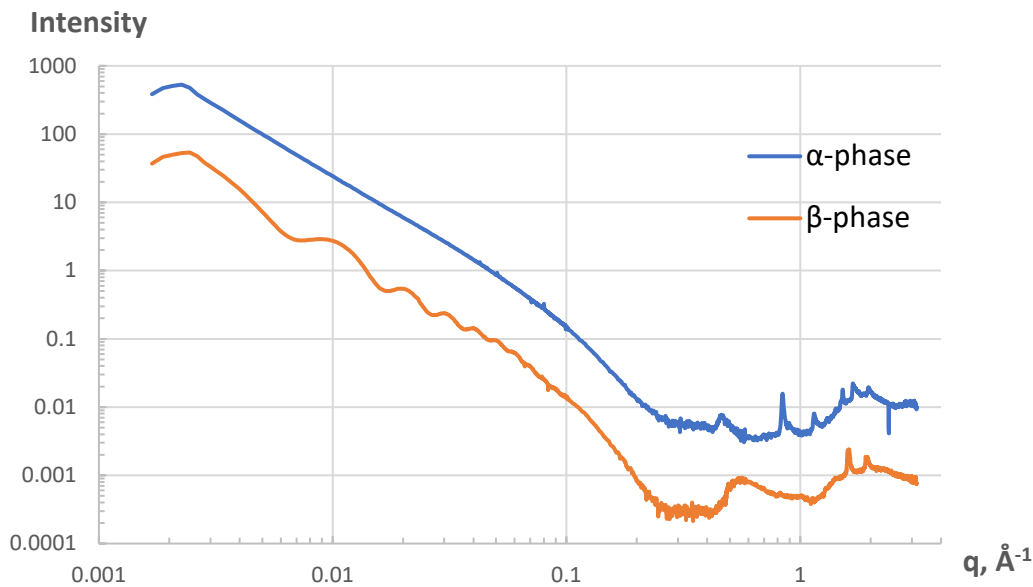


Figure 3.18. Solution SAXS and WAXS patterns of α - and β - phases. Both graphs have Porod slope of -2, indicating 2D sheet structure.

This phase transition is irreversible, suggesting that β -phase is thermodynamically more stable than α -phase (Figure 3.19). In UV-vis spectrum addition of NaCl leads to blue shift (490 nm absorption peak is blue shifted to 420nm) which upon annealing red shifts to $\lambda_{\text{max}} = 523$ nm and a narrower satellite peak at 565 nm (Figure 3.17F). Interestingly, if annealing is performed in 1mM NaCl, the morphology is helical instead of scroll (revealed by AFM and cryo-TEM) which, however, have identical WAXS patterns. Upon cooling the helices grow dramatically.

Hydrogen production with $[\text{Mo}_3\text{S}_{13}]^{2-}$ catalyst⁵³ yields TON in 18h for β^{helix} - and β^{scroll} - phases equal to 2600 ± 880 and 1900 ± 530 , respectively, while for α -phase only 790 ± 230 TON. Similar TON values for β^{helix} - and β^{scroll} -phases are to be expected as they have identical WAXS patterns, hence identical molecular packing.

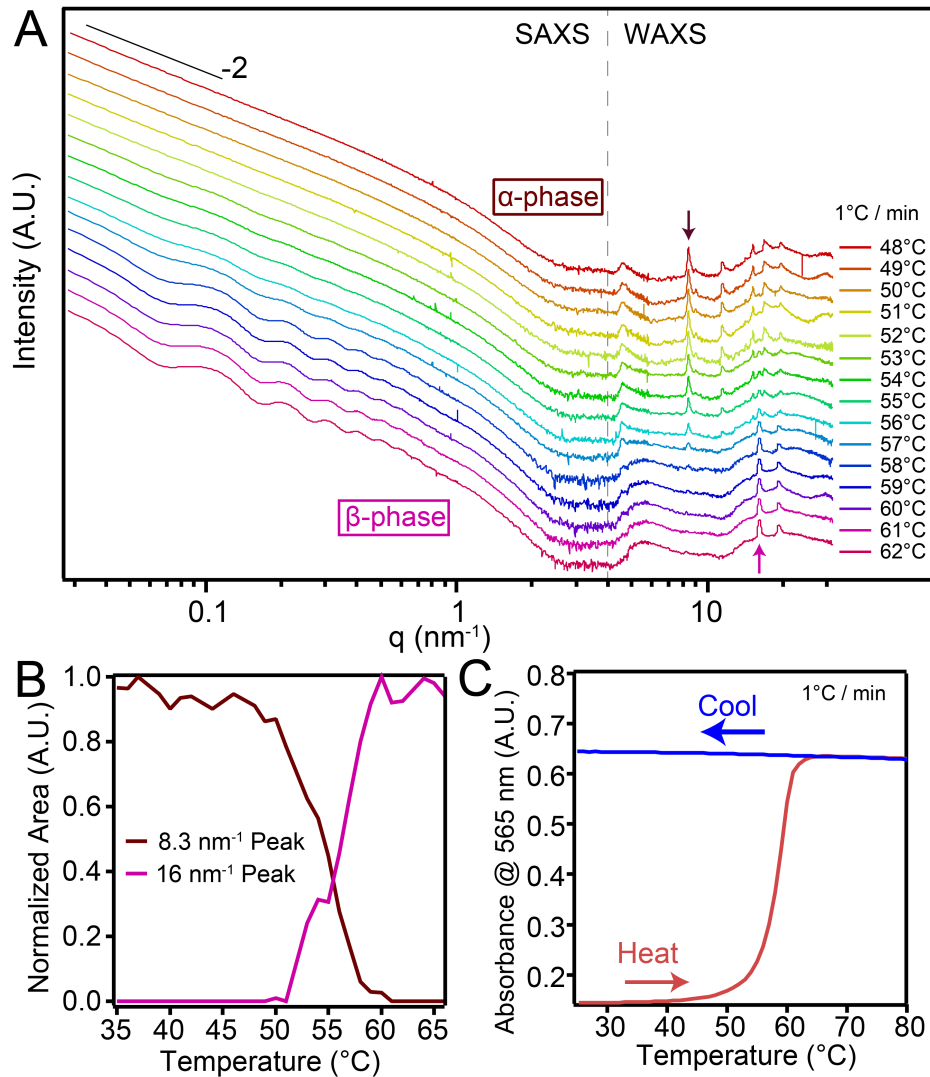


Figure 3.19. **A)** Variable temperature (VT) X-ray scattering patterns of 7.25 mM T3-PMI solution with 50 mM NaCl. Samples were heated at $1^\circ\text{C}/\text{min}$ and data collected every minute, **B)** normalized intensity vs. temperature plots for the 8.3 and 16 nm^{-1} peaks in (A), **C)** VT absorbance spectra of 50 mM NaCl T3-PMI solution in a $50 \mu\text{m}$ demountable cuvette monitored at 565 nm . Temperature was ramped at $1^\circ\text{C}/\text{min}$. (Adapted from Kazantsev, et al.⁵².)

The WAXS peak positions were used to determine the lattice parameters (a , b , and γ) for the 2D oblique unit cells of both phases of T3-PMI. For the α -phase $a = 8.1 \text{\AA}$, $b = 4.4 \text{\AA}$, $\gamma = 122^\circ$ and for the β -phase $a = 7.5 \text{\AA}$, $b = 4.6 \text{\AA}$, $\gamma = 121^\circ$ (Figure 3.20). To subtract background, polynomials were fitted segment-wise to the shoulders of peaks to produce a background function that was subtracted from each of the data

points. The background subtracted data is shown in Figure 3.20. As before, this PMI was modeled as an orthorhombic slab of uniform density with a rod attached at a right angle (which was fixed during fitting) to the center of its upper edge, and a point charge on the lower diametrically opposing edge at a quarter side distance from a corner of the slab. The rod and point charge model carboxypentyl and propyl chains, respectively. The fitting procedure followed closely to HO-PMI case, with an exception of offset introduction, which was one of the fitting parameters.

The β -phase, however, was only possible to fit with simpler model consisting of slabs without rods. This might be indicative of removal of ordering (melting) of carboxypentyl chains during α -phase to β -phase transition. With chains present the simulated pattern always had a diffraction peak with low q value as a result of 4 molecule basis which breaks the symmetry. Melted chains led to higher symmetry as the actual basis of β -phase became half of that of α -phase. But to preserve consistency of peak indexing between two phases we formally assumed four-molecule basis. The obtained parameters demonstrate a herringbone lattice structure for α -phase (Figure 3.20).

Reasonable fits could also be obtained with edge-centered herringbone structure but only with large distortions of π - π parallel alignment. Solution WAXS does not have sufficient resolution to clearly distinguish between distorted edge-centered herringbone and herringbone lattices in this system.

The obtained results clearly demonstrate the transformations in molecular packing taking place during annealing. These molecular rearrangements have profound impact on catalytic activity.

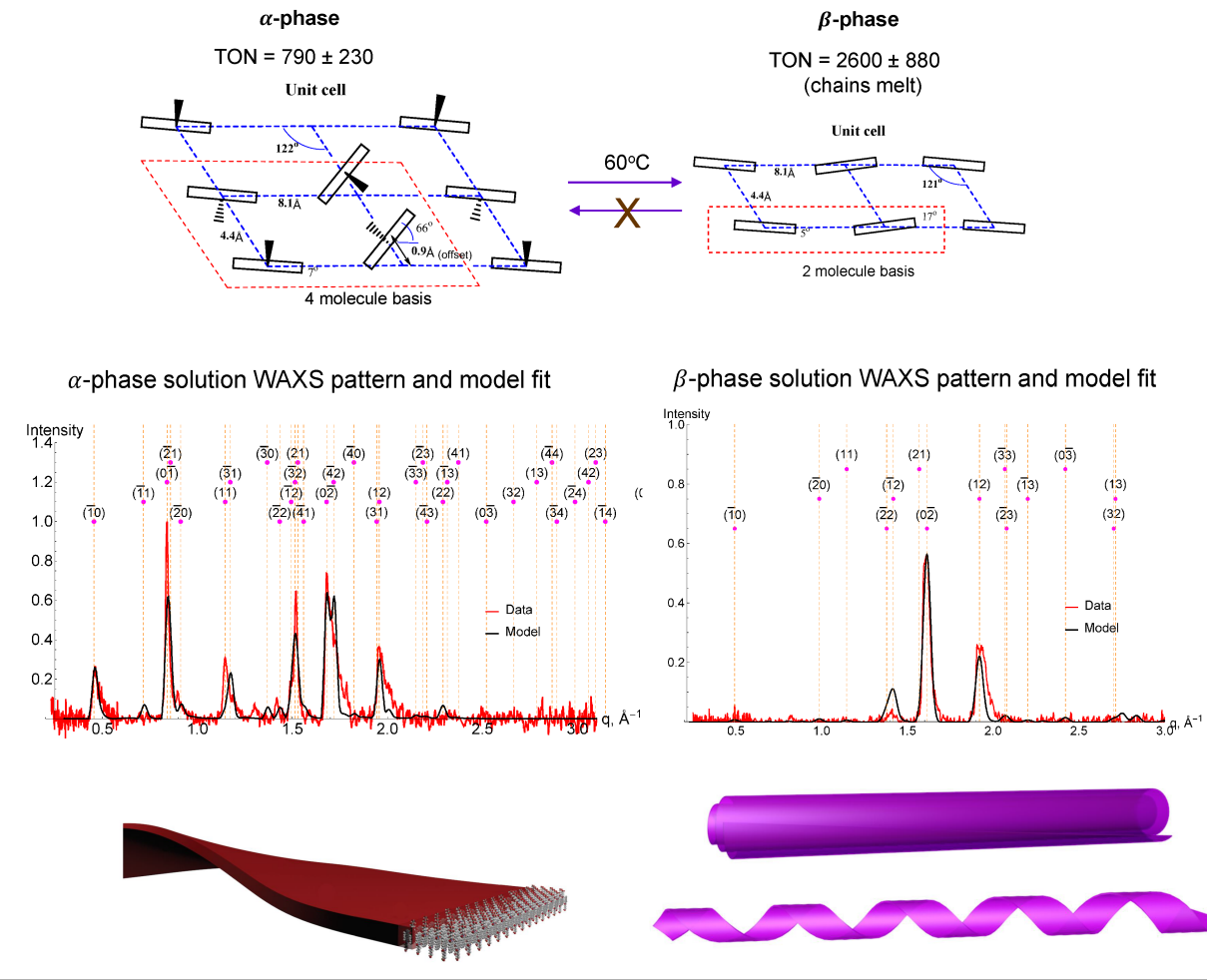


Figure 3.20. Solution WAXS patterns of α - and β -phases of T3-PMI along with their fits. Inferred molecular packing and mesoscopic morphology are shown as well.

3.4. Summary

Molecular packing of PMI photocatalytic nanostructures is a key parameter controlling catalytic yield. The presented general approach for extracting the molecular packing details in 2D molecular crystals from WAXS patterns established the ordering modes of aromatic and chain fragments of various PMI systems. The diffraction theory successfully reproduced the asymmetric line-shape of diffraction peaks in solution WAXS by incorporating the form factor of the basis, and further yielded the electron density averaged

height of the sheet *in situ*. Herringbone arrangement of aromatic rings was revealed, with various degrees of transverse shift and tilt of the molecules. Information on domain size was demonstrated to be contained in the low q shoulder of the peaks, while the high q shoulder had a nonlinear coupling of the height and domain size. We showed that the diffraction peaks in solution WAXS are shifted from the positions of reciprocal lattice vectors. This approach is applicable to crystalline 2D structures both in bulk solutions and at interfaces, and is adaptable for testing detailed theory-based atomic-scale models.

4. X-ray reflectivity studies of tetrathienoacene based dyes for dye sensitized solar cells

4.1. Introduction

Efforts have been made since late 1960s to use photoactive dyes as active components in solar cells. The guiding paradigm was to utilize semiconductor interfaces of high smoothness for capturing the photogenerated electron from photo-excited dye molecule⁵⁴⁻⁵⁷. But even dyes with the best light absorbing characteristics, i.e. phtalocyanines and porphyrins, would still result in efficiencies less than 1%⁵⁸. The realization that drastic increase in surface area of electron capturing electrode (upon which dye monolayers assemble) has a potential to enhance conversion efficiencies by an order of magnitude, led to the creation of new systems with substantially higher interface areas⁵⁹⁻⁶⁰. This ultimately resulted in the first high efficiency (7-8%) dye sensitized solar cell (DSSC) based on porphyridal ruthenium (II) dye⁶¹. The key step of this work by O'Regan and Graetzel⁶¹ was the creation of high surface area porous TiO₂ by deposition from a colloidal solution and subsequent annealing to convert TiO₂ from amorphous to anatase phase which has a suitable bandgap for electron capture into its conduction band. Introduction of new metal based complexes further improved the efficiency, currently reaching over 13%⁶². However, metal free dyes have a crucial advantage over transition metal complexes in that they are structurally more tunable with broader spectrum of possible molecular designs, thereby in principle allowing synthesis of dyes with better characteristics at lesser manufacturing cost⁶³⁻⁶⁵. More efforts are necessary to achieve this goal as metal free dyes still have lower efficiencies compared to their metal containing counterparts, mostly due to large recombinational losses⁶⁶⁻⁶⁷.

4.1.1. Operation principle

The first step of the electron transfer cycle in DSSC (Figure 4.1) involves absorption of a photon by a dye molecule which is covalently bound to an electrode (TiO_2 in anatase phase). The excited molecule (S^*) then transfers an electron onto the conduction band of the semiconductor electrode (TiO_2). The electron passes through the external resistance and returns to the counter-electrode and channels through the electrolyte (R/R^- , e.g. I^-/I_3^- couple) to the positively charged dye molecule (S^+) neutralizing it. This concludes the cycle⁶⁸.

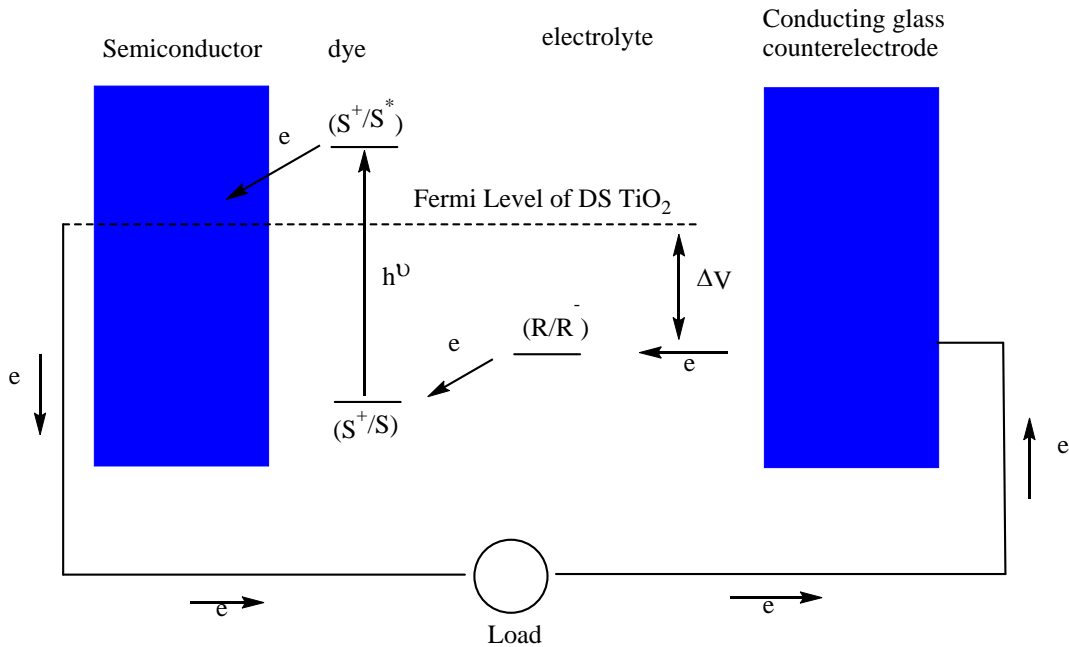


Figure 4.1. Operating principle of DSSC (DS TiO_2 = dye sensitized anatase electrode). (Adapted from Hagfeldt, et al.⁶³)

The conversion efficiency of a solar cell is defined through the following expression:

$$\eta = \frac{P_{max}}{P_{in}} \quad (4.1)$$

where P_{max} is the maximum power of the cell, P_{in} is the intensity of the incident light. A parameter, called fill factor, is defined through the open-circuit photovoltage (V_{oc}) and short-circuit current J_{sc} :

$$FF = \frac{P_{max}}{J_{sc}V_{oc}} \quad (4.2)$$

With this parameter, which takes the values between 0 and 1, one can cast the expression of efficiency in the following manner:

$$\eta = \frac{J_{sc}V_{oc}FF}{P_{in}} \quad (4.3)$$

Another characteristic of the cell is the incident photon flux to current conversion efficiency (IPCE):

$$IPCE = \frac{J_{sc}(\lambda)}{e \Phi(\lambda)} \quad (4.4)$$

where e is the elementary charge.

4.2. Donor- π -acceptor (D- π -A) dye design and TiO_2 electrode

D- π -A organic dyes that we will investigate, feature a hydrophobic electron-donating (triphenylamine (**TPA**)) moiety bridged through the π -conjugated (tetrathienoacene) unit to a hydrophilic electron-accepting (cyanoacrylic acid) group covalently bound to TiO_2 surface.⁶⁹⁻⁷⁷ Absorption of a photon causes a jump of the electron from the donor group through the bridge to the low lying energy level of the acceptor fragment which then transfers the electron to the conduction band of the TiO_2 .^{71, 77-82}

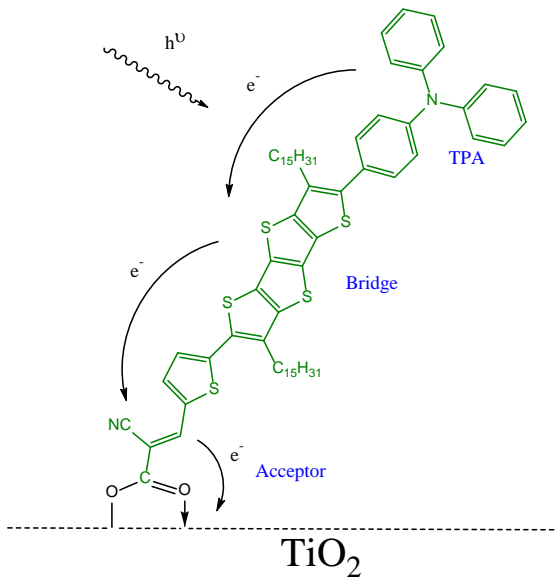


Figure 4.2. Schematic depiction of electron transfer from donor group to TiO₂ conduction band upon absorption of photon by a dye molecule.

A design of efficient metal-free DSSC should consider all aspects of the cell structure, including both the molecular orbital shape and energy levels of individual molecules as well the morphology of dye assembly on mesoporous TiO₂ spheres. While methods for electronic and conformational study of individual molecules are well established, the arrangement of dyes on mesoporous TiO₂ surface is difficult to investigate with existing techniques. To address this shortcoming, we created a model surface of TiO₂ by atomic layer deposition (ALD) onto freshly cleaned hydrophilic Si wafer. The resulting surface is sufficiently smooth (\sim 3-5 Å roughness). The amorphous film can then be annealed to convert to anatase phase. Dipping it into dye solution and subsequent washing with solvents creates a dye monolayer film with low roughness, readily amenable to investigation by X-ray reflectivity (Figure 4.3). Because the curvature of mesoporous TiO₂ sphere is relatively large compared to the scale of dye molecules, we can reasonably assume that our model surface gives a good approximation to the actual electrode surface.

Many DSSC dyes do not form strict order, thereby giving no diffraction patterns characteristic to 2D lattices. XRR morphological studies therefore are especially relevant in these cases.

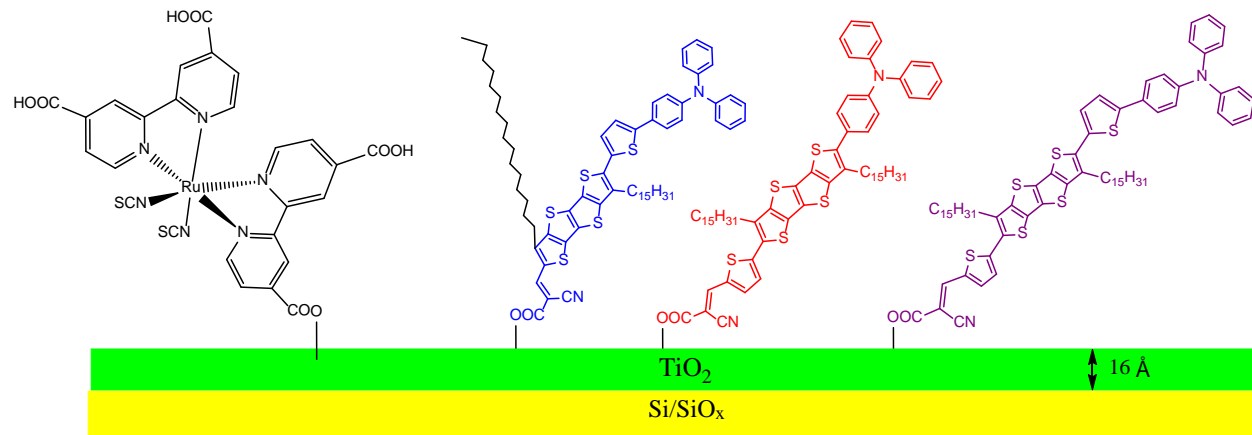


Figure 4.3. Schematic depiction of various dyes covalently bound to ALD deposited TiO_2 on Si/SiO_x .

4.3. TTAR dyes

In our work we will investigate newly synthesized (by the group of Prof Ming-Chou Chen) dyes with tetrathienoacene (TTAR) bridge between triphenylamine (TPA) donor and cyanoacrylic acceptor (A). We will insert thiophene rings between the bridge and the donor group, the bridge and the acceptor group or both⁸³⁻⁸⁵ (Figure 4.4). This extension of π -conjugation leads to a decrease in the bandgap but also induces conformational changes which, alongside modified intermolecular interactions, affect the assembly modes of the dyes on TiO_2 surface. We will investigate the packing of these particular dyes by XRR on ALD deposited TiO_2 . Table 4.1 shows the basic parameters of DSSCs built with these dyes. TPA-TTAR-T-A dye demonstrates the highest efficiency of 10.1%. As it will be revealed below, morphology seems to be playing a key role in its high efficiency.

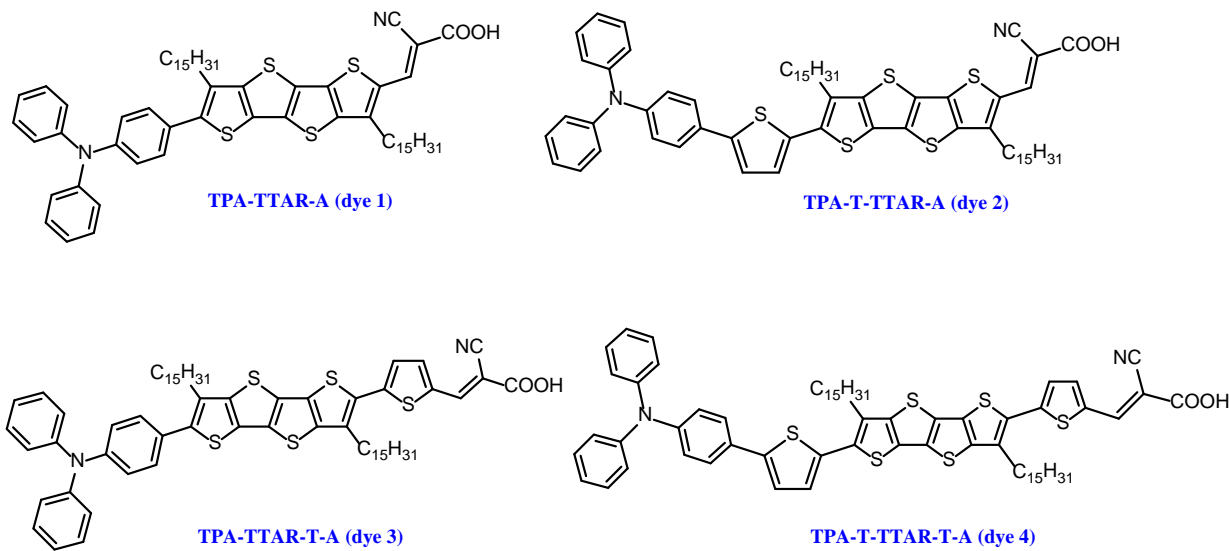


Figure 4.4. Structure of TTAR based dyes.

Table 4.1. Characteristics of TTAR based DSSCs

Dye	V_{oc} (V)	J_{sc} (mA/cm ²)	FF (%)	PCE, η (%)
TPA-TTAR-A (1)	0.946	7.66	65.8	4.76
TPA-T-TTAR-A (2)	0.893	10.1	68.1	6.15
TPA-TTAR-T-A (3)	0.833	16.5	73.7	10.1
TPA-T-TTAR-T-A (4)	0.832	11.8	70.3	6.91

The UV-vis spectra of the four dyes in 1,2-dichlorobenzene (*o*-DCB) are plotted on Figure 4.5. Two peaks correspond to charge-transfer (CT) light absorption and higher energy $\pi-\pi^*$ transition. The insertion of thiophenes induces red-shifts as a result of extension of conjugation. The molar extinction coefficients at their absorption maxima are ~3-4 times higher than those of Ru(II) polypyridyl complexes (N719; 1.40×10^4 M⁻¹cm⁻¹), an efficient metalorganic dye⁸⁶. This adds to the higher ability of TTAR dyes to harvest light compared to N719 (Figure 4.6). HOMO-LUMO bandgap deduced from cyclic voltammogram and optical spectrum demonstrate the expected red-shifts (Figure 4.7). Figure 4.7C visualizes the electron density

localization of HOMO and LUMO orbitals of all four dye molecules, showcasing the redistribution of electron density from TPA moiety onto cyanoacrylic group upon excitation.

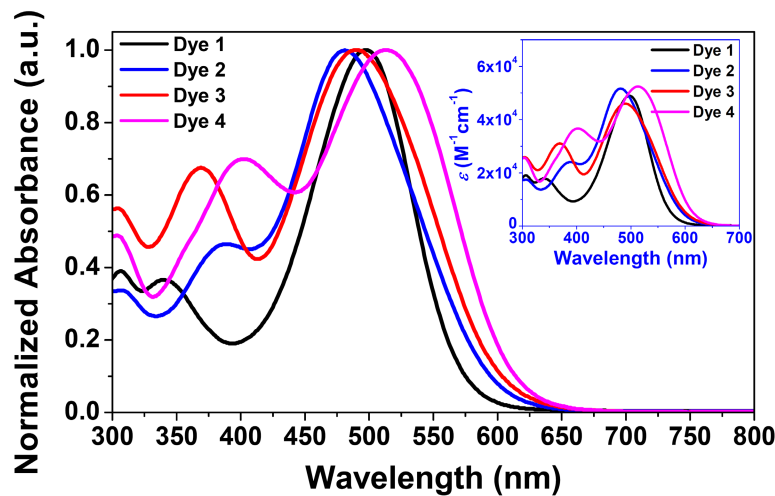


Figure 4.5. UV-vis absorption spectra of TTAR dyes and their corresponding molar absorption coefficients measured in *o*-DCB in concentration of 10^{-5} M. (Adapted from Zhou, et al.⁸³.)

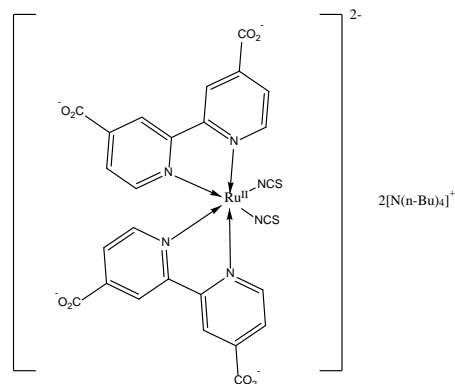


Figure 4.6. Structure of N719 dye.

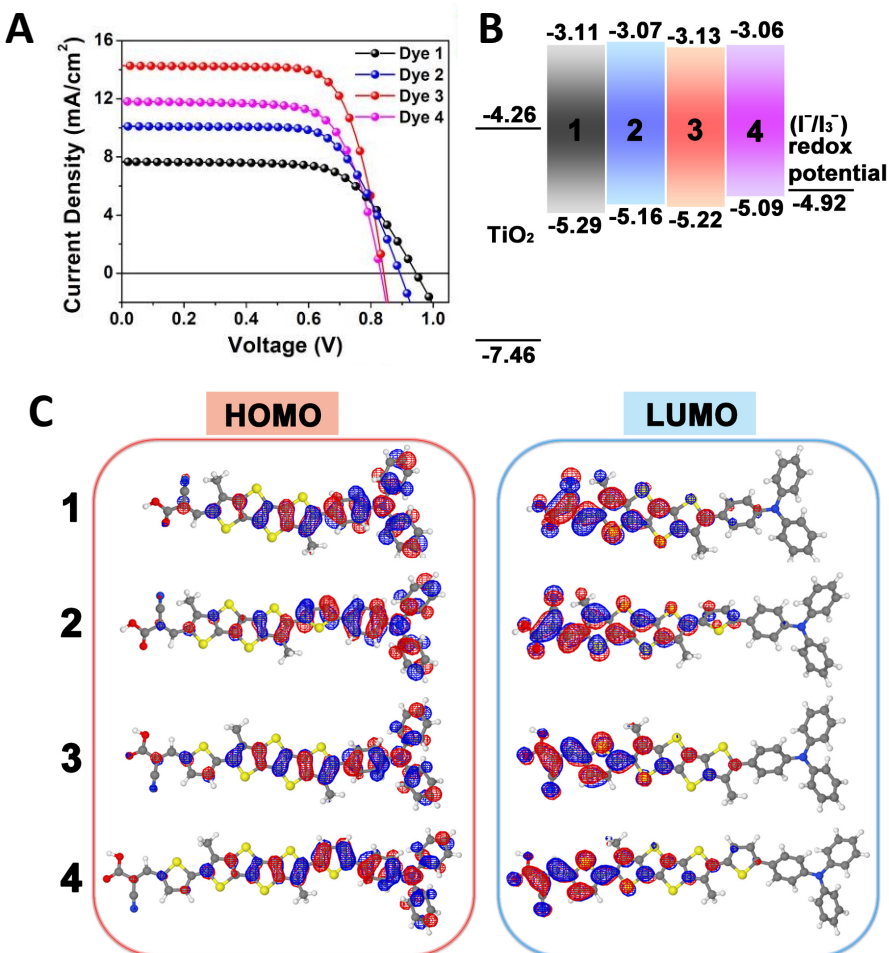


Figure 4.7. Electronic structure characterization of organic dyes. **A**) $J-V$ curves of dyes **1-4**, **B**) band alignment diagram with respect to conduction band of TiO_2 , where the HOMO levels were determined from the onset of first oxidation peak and CV experiments, and LUMO levels are derived from film optical bandgap, **C**) molecular orbital energy diagrams and isodensity surface plots of the HOMO and LUMO for the dyes. (Adapter from Zhou, et al.⁸³.)

4.3.1. Experimental methods

Si wafer preparation. Si wafers were washed with propanol and placed in heated piranha (98% H_2SO_4 : 50% H_2O_2 = 2:1) on low heat for half an hour. They were retrieved and washed with purified deionized water and submerged into 30% hydrochloric acid for 5 minutes and washed again with purified deionized water.

ALD deposition of TiO₂. Tetrakis-dimethyl-amido titanium⁸⁷ was used as a precursor of TiO₂ for atomic layer deposition (ALD). Depending on the desired thickness, appropriate number of cycles were chosen. Films with thicknesses less than 15 Å had high roughness and are not suitable for XRR studies. Full hydroxylation of Si wafer is crucial for obtained smooth thin films of TiO₂ (Figure 4.8).

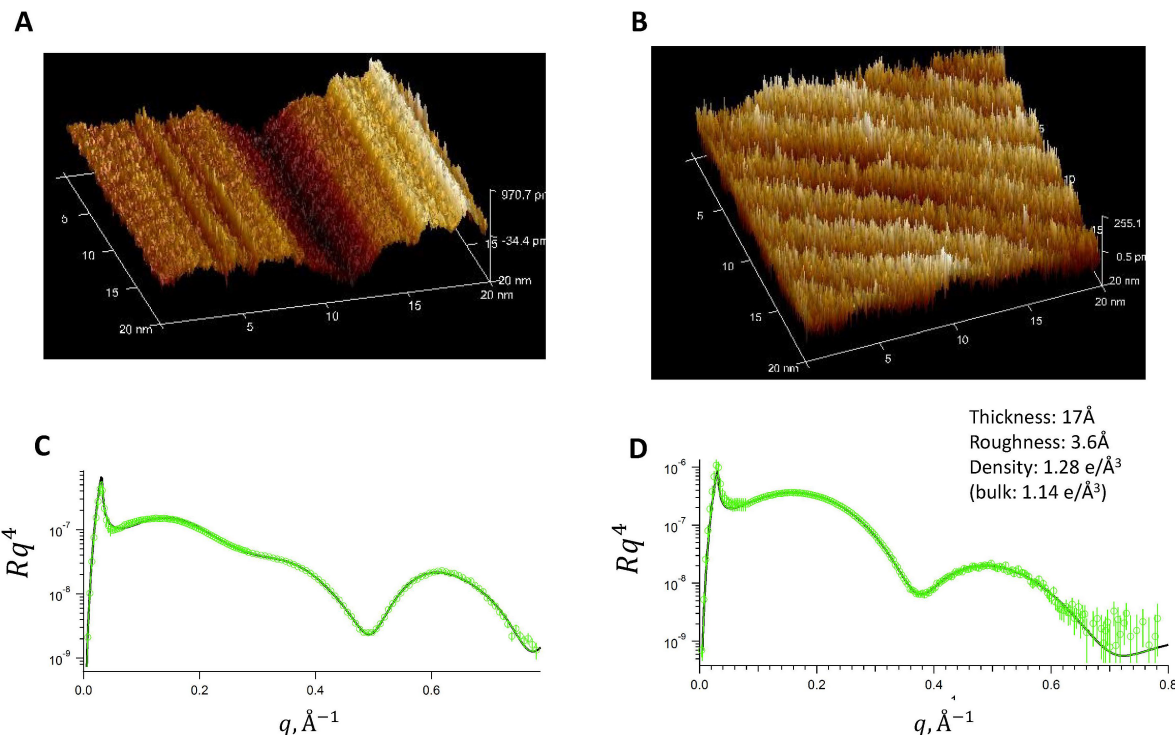


Figure 4.8. **A)** and **B)** AFM images of ALD deposited TiO₂ on poorly and well hydroxylated Si wafer. **C)** Lateral inhomogeneity of TiO₂ thin film on poorly hydroxylated Si manifests itself as a double layer on XRR data. Solid black line is a fit for two slab model. **D)** XRR data for TiO₂ thin film on well hydroxylated Si. Solid black line is a fit for a single slab model.

XRR Measurements⁸³: XRR data were collected on Rigaku Smartlab with standard slits for 300mm goniometer. Curves of Rq^4 vs q were fitted by Motofit with errorbars including counting, systematic errors and edge effect uncertainties for small q region⁸⁸ (Chapter 2.2). TiO₂ thin films ~16-17 Å thick were prepared via ALD on Si substrates treated as described above, and subsequently sintered at 500 °C for 2 hrs under pure oxygen-nitrogen mix (1:4) to obtain anatase TiO₂ phase. XRR samples were prepared by

immersing the TiO_2 coated substrates into THF/EtOH solution (1:1) of dye four dyes and allowed self-assembly monolayer growth over 24 hours. The substrates were subsequently washed by pure solvents.

4.3.2. Assembly study of TTAR dyes on Si/SiO_x

We first begin with a study of monolayer morphology of the four TTAR dyes on Si wafer itself (with hydroxylated native oxide). All steps would follow the procedures of deposition described above but without the ALD deposition step. By comparing the obtained results to those on TiO_2 film, we will be able to discern the effect TiO_2 surface has on the monolayer packing. Figure 4.9A shows the XRR data with their best fits and Figure 4.9B the extracted electron density profiles. As one can immediate notice by inspecting the density profiles, TPA-TTAR-T-A dye forms the best packed structure, with the lowest footprint (Table 4.2).

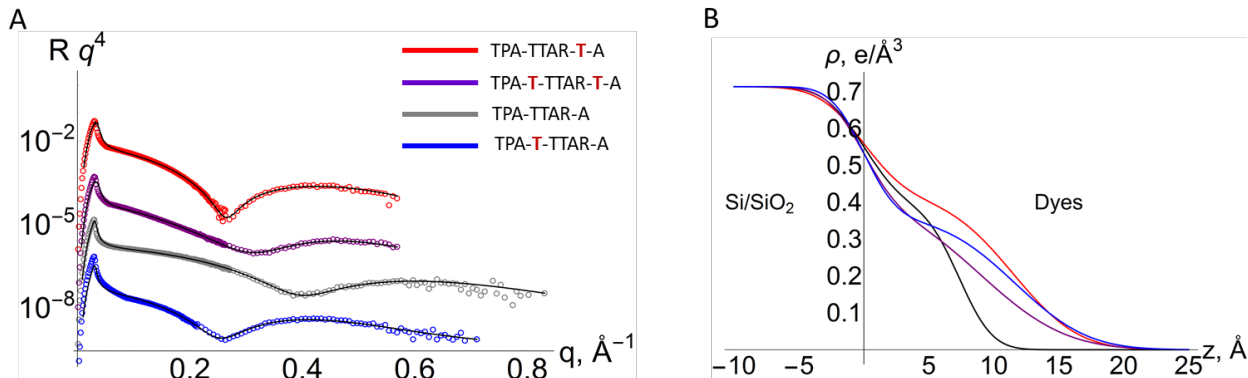


Figure 4.9. **A)** XRR data and model fits. The top three curves are vertically offset for purposes of clarity. Scattering vector $q = 4\pi \sin(2\theta/2)/\lambda$. **B)** The electron density vs. depth of the sample.

Table 4.2. Extracted film parameters from XRR data fits for dye films deposited on Si/SiO_x .

Dye	Thickness (\AA)	Electron density, ρ ($e \text{\AA}^{-3}$)	Roughness of Si film (\AA)	Roughness of dye coated Si substrates (\AA)	Native SiO_2 layer thickness (\AA)	Molecular footprint (\AA^2)
TPA-TTAR-A (1)	7.3	0.39	2.5	2.0	5.0	174
TPA-T-TTAR-A (2)	11.7	0.36	2.0	4.4	6.2	132
TPA-TTAR-T-A (2)	11.6	0.41	2.8	4.0	10.0	116
TPA-T-TTAR-T-A (3)	9.0	0.41	2.2	5.2	15.0	161

4.3.3. Assembly study of TTAR dyes on TiO₂ films

In our first attempt we deposited ~120 Å TiO₂ film on SiO_x/Si. XRR data proved the high quality of the obtained film (Figure 4.10A). After sintering the TiO₂ films showed weak and broad diffraction peak at 1.786 Å⁻¹ (anatase (011) peak) both in grazing incidence in-plane scattering as well as in reflectivity scan. However, because of large discrepancy between the dye film (~15 Å) and TiO₂ thicknesses, it was impossible to extract information about dye morphology in a statistically significant manner on these thick TiO₂ films (Figure 4.10B).

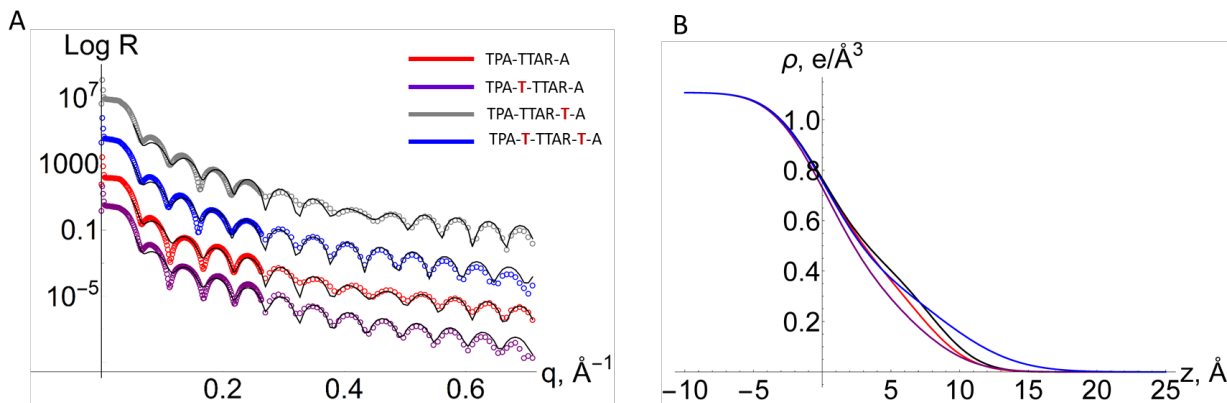


Figure 4.10. **A)** XRR data and model fits for dye films deposited on ~120 Å TiO₂. **B)** The electron density of the organic dyes vs. depth of the sample.

Table 4.3. Extracted film parameters from XRR data fits for dye films deposited on ~120 Å TiO₂.

Dye	Thickness (Å)	Electron density, ρ (e Å ⁻³)	Roughness of Si/TiO ₂ (Å) (fixed)	Roughness of the film (Å)	TiO ₂ layer thickness (Å)	Footprint of the molecule (Å ²)
TPA-TTAR-A (1)	8.1	12	3	2.7	114	145
TPA-T-TTAR-A (2)	8.8	12	3	4.3	117	143
TPA-TTAR-T-A (3)	7.43	12	3	2.9	115	143
TPA-T-TTAR-T-A (4)	7	10.5	3	3.4	116	181

To gain better insights into dye orientation, coverage and aggregation on the TiO₂ surface, X-ray reflectivity measurements were performed on monolayer dye-sensitized TiO₂ surface of much lower thickness (~16 Å). The substrates were washed after dye deposition by pure solvents (EtOH and THF) to remove non-covalently bound layers on top of the monolayer. During fitting of the curves we imposed constraints: electron densities of the films are not much lower than the electron density of cyclohexane and roughnesses of interfaces are greater than 2 Å. Figure 4.11 and Table 4.4 summarize the results of the fitting. Interestingly, dyes without thiophene spacer close to the cyanoacrylic anchoring group (dyes **1** and **2**) exhibit relatively small thicknesses of 7.3 Å and 6.6 Å, indicating that the TiO₂ bound dye molecules are not perpendicular to the surface, but significantly tilted (estimated tilt angles with respect to the substrate normal are ~65° and ~69° for dyes **1** and **2**, correspondingly)⁸⁹. The addition of thiophene ring between the cyanoacrylic acid and tetrathienoacene bridge significantly changes the orientation of the dye molecules. Despite similar molecular lengths of dye **2** and **3**, dye **3** is more than 2 times thicker than dye **2**. In addition, dye **3** exhibits significantly smaller molecular footprint, suggesting a more vertical dye orientation (estimated binding tilt angle of ~39°) and denser packing on TiO₂, which not only can enhance dye loading for more efficient light harvesting, but can also prevent direct contact between TiO₂ and electrolyte, reducing recombination losses. Despite its largest backbone, dye **4** shows slightly smaller monolayer thickness and larger molecular footprint.

To measure dye desorption from TiO₂ electrodes a 0.3 mM dye solutions in THF/EtOH (1:1) were used for loading. For each sample, the dye was slowly desorbed from the TiO₂ electrodes in THF for 24 hrs; the amount of the desorbed dye in the THF solution was measured by optical absorbance. For equal area films, the optical absorbance increases linearly with the dye molecule concentration. The relative difference in absorbance is a comparative measure of dye loading on TiO₂ surfaces. Dye **1** and **2** had relatively low dye loading of 2.1×10^{-8} mol/mg and 1.3×10^{-8} mol/mg, respectively, compared to 7.4×10^{-8}

mol/mg and 6.6×10^{-8} mol/mg for dye **3** and **4**. This result is consistent with the higher molecular footprint and larger tilt angle identified by XRR. Clearly, the addition of thiophene close to the cyanoacrylic anchoring group plays a key role in dye orientation and coverage, favoring more vertical alignment and higher dye coverage for dyes **3** and **4**. Meanwhile, the insertion of thiophene between TPA and TTAR groups reduces the packing density for dyes **2** and **4** compared to dyes **1** and **3**, respectively. This is in excellent agreement with the XRR-derived molecular footprint. Introduction of thiophene ring at the donor position causes undesirable twist in molecular backbone (Figure 4.12) and suboptimal dye arrangement on the TiO_2 surface, yielding lower light absorption and higher recombinational losses.

For comparison we performed the same experiment for the well-known N719 dye under the same conditions (Figure 4.13). As could be expected from the presence of heavy Ru atom, it is much denser and thinner.

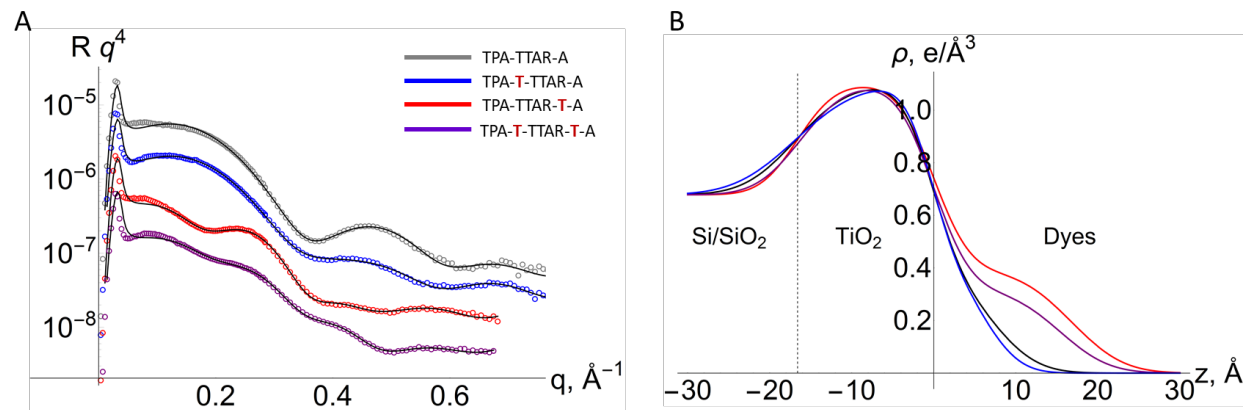
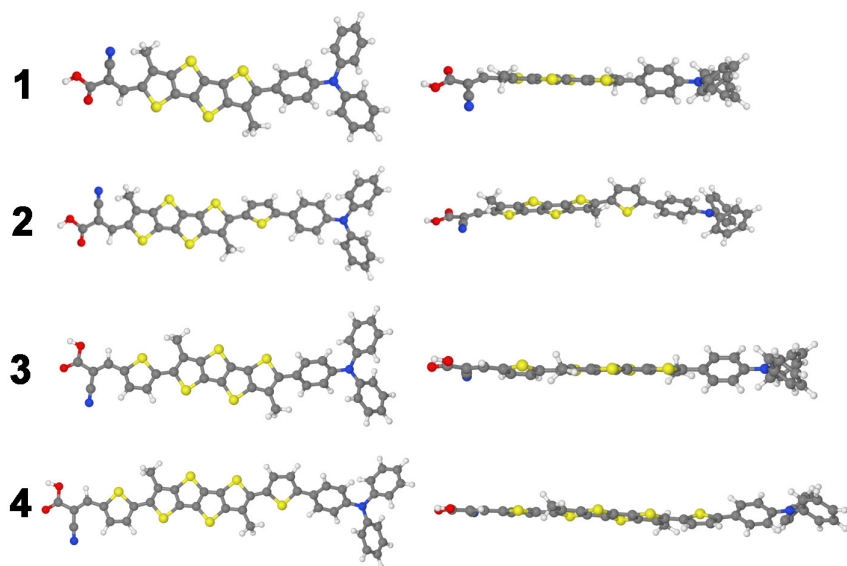
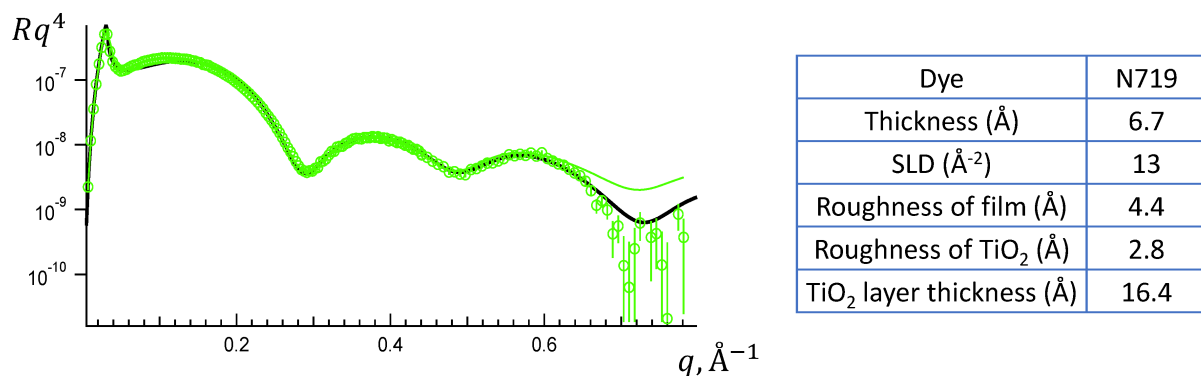


Figure 4.11. **A)** XRR data and model fits for dye films deposited on $\sim 16 \text{\AA}$ TiO_2 . **B)** The electron density vs. depth of the sample.

Table 4.4. Summary of XRR-derived parameters for dye films deposited on $\sim 16\text{\AA}$ TiO_2 .

Dye	Thickness (Å)	Electron density, ρ (e Å ⁻³)	Roughness of Air/dye interface (Å)	Roughness of TiO_2 /dye interface (Å)	TiO_2 layer thickness (Å)	Roughness of $\text{TiO}_2/\text{SiO}_2$ interface (Å)	Molecular footprint (Å ²)
TPA-TTAR-A (1)	7.3	0.41	4.5	3.0	16.4	5.0	152
TPA-T-TTAR-A (2)	6.6	0.41	3.5	2.7	16.5	5.9	183
TPA-TTAR-T-A (3)	16.8	0.39	5.0	3.5	16.6	3.6	79
TPA-T-TTAR-T-A (4)	15.4	0.32	4.7	3.6	16.2	4.3	104

Figure 4.12. DFT-optimized geometry of TTAR dyes showing top view (left) and side view (right). (Adapted from Zhou, et al.⁸³.)Figure 4.13. XRR data and best fit for N719 dye monolayer on TiO_2 alongside the extracted characteristics of the film.

4.3.4. Assembly study of branched TTAR dye

The above investigated TTAR dyes had strategically attached pentadecyl chains to prevent dye aggregation and thereby allow formation of high quality monolayers. They also suppress intermolecular recombination. However, in the case of dense packing, these alkyl chains are not effective in preventing π - π interactions which lowers V_{oc} . To examine the effect of branched alkyl chains vs. linear chains on photovoltaic performance and charge recombination dynamics in DSSCs, we investigate new TTAR dyes⁹⁰ with modified chains (Figure 4.14).

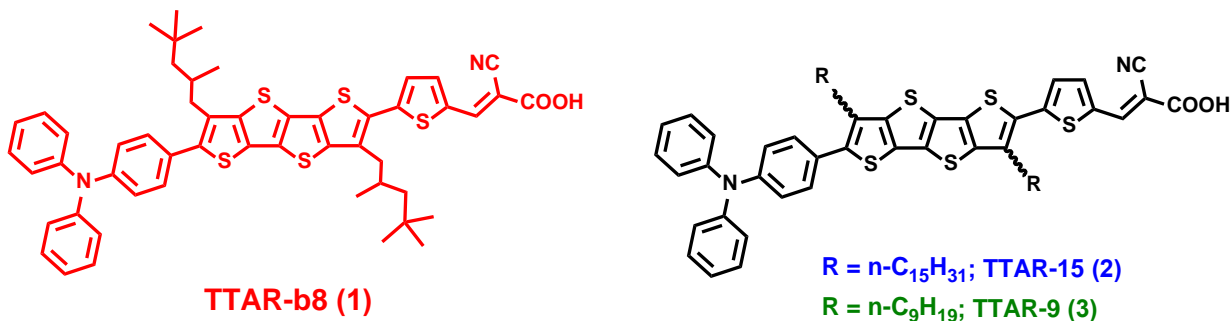


Figure 4.14. Structure of branched TTAR dyes. (Adapted from Ezhumalai, et al.⁹¹.)

DFT calculations (B3LYP/6-31G* level) on individual molecules in vacuum affirm that these chain modifications do not affect the band gap in any substantial manner (Figure 4.15A, B). HOMO is localized on TPA moiety while LUMO on cyanoacrylic end as expected. Absorption of photon leads to redistribution of electron density from TPA to cyanoacrylic group. Branched alkyl chain however induces conformational distortions by altering dihedral angles, as is evident from Figure 4.15C. UV-vis spectra in *o*-C₆H₄Cl₂ are almost identical (Figure 4.16). This suggests that intermolecular interaction are the primary reason for differing photovoltaic characteristics. The spectra of the dyes absorbed on TiO₂ exhibit red shifts. This can be attributed to the formation of covalently bound assemblies on the TiO₂ surface (Figure 4.16B). DFT calculated HOMO and LUMO energy levels differ substantially from HOMO energy measurement by

differential pulse voltammetry (DPV) (-5.19 eV) and LUMO energy inferred from optical absorption spectra (~ 3.28 eV)⁹². This discrepancy is an intrinsic feature of DFT computations for similar systems.

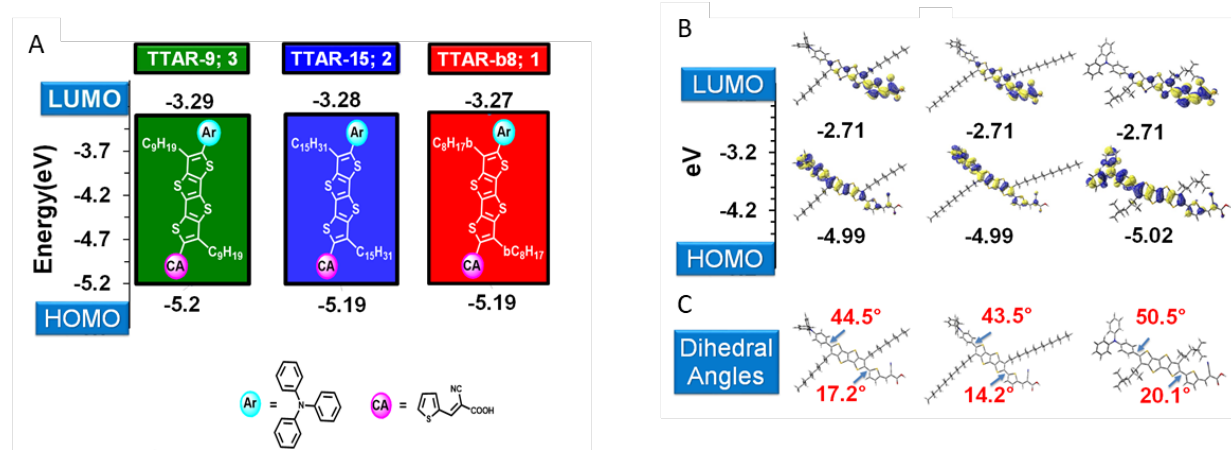


Figure 4.15. Orbital energy levels of molecules 1-3. A) DPV-derived HOMO and LUMO energy levels, B) DFT derived molecular orbitals, C) optimized molecular structures with dihedral angles shown. (Adapted from Ezhumalai, et al.⁹¹.)

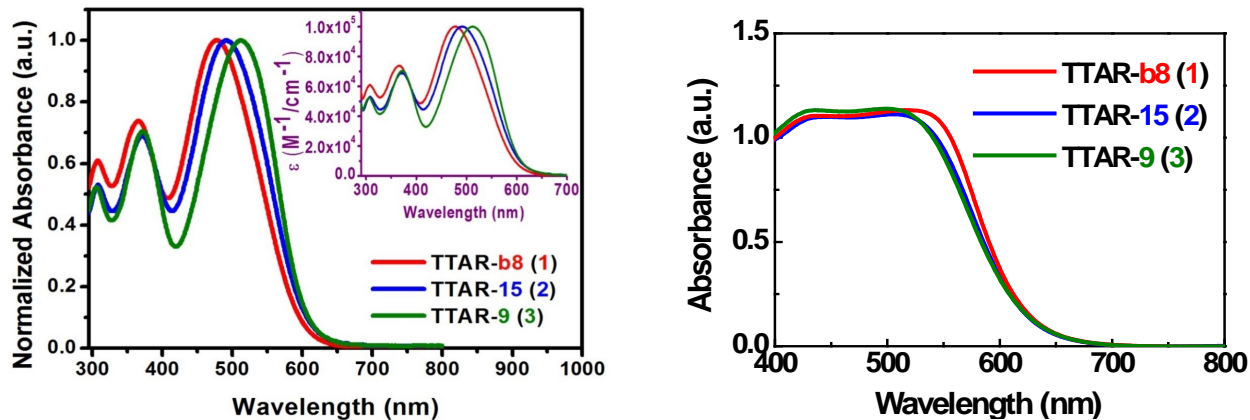


Figure 4.16. A) UV-vis absorption spectra of dyes 1-3 and their corresponding molar absorption coefficients measured in *o*-C₆H₄Cl₂ at a concentration of 10⁻⁵ M, B) absorption spectra of the dye-sensitized nanocrystalline TiO₂ films. (Adapted from Ezhumalai, et al.⁹¹.)

Figure 4.16 and Table 4.5 summarize the photovoltaic characteristic of DSSCs based on these three dyes. TTAR-b8 exhibits both highest FF , V_{oc} and J_{SC} , and as a result, highest overall efficiency η . The efficiency can be substantially enhanced by using stack photonic crystals with a reflector, which reflect

and diffract the incoming light back to dye coated TiO_2 microspheres.⁹³ We placed a double-layer three-dimensional (3D) photonic crystal (PhC) with hole diameter of 375/410nm behind the count electrode^{94,95}. The photovoltaic performance of the TTAR-b8 dye DSSC with 3D PhC layer was measured under AM 1.5G irradiation (100 mW cm^{-2}) of simulated solar light, and the results are plotted in Figure 4.18. The TTAR-b8-based cell had $J_{sc} = 18.79 \text{ mA/cm}^2$, $V_{oc} = 0.811\text{V}$, a fill factor = 73.31%, and $\eta = 11.18\%$. Performance parameters are summarized in Table 4.6. These TTAR-b8-based cells deliver the highest performance of any fused-thiophene-based DSSC reported to date.

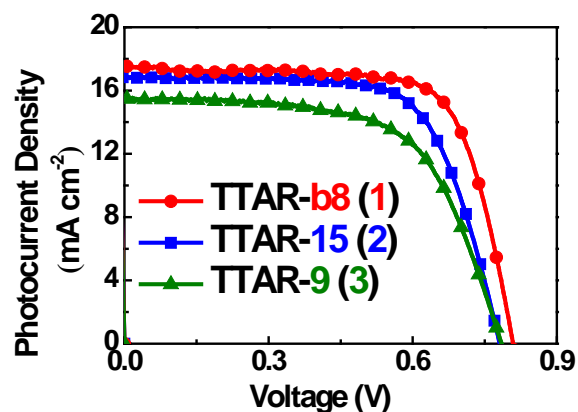


Figure 4.17. The photocurrent current density–voltage (J - V) characteristics of the DSSCs with various dyes, measured under 1 sun illumination (Adapted from Ezhumalai, et al. ⁹¹).

Table 4.5. Photovoltaic parameters of the DSSCs with various dyes.

Dyes	η (%)	V_{oc} (V)	J_{sc} (mA cm^{-2})	FF
TTAR-b8	10.21 ± 0.17	0.81 ± 0.01	17.54 ± 0.05	0.72 ± 0.01
TTAR-15	9.02 ± 0.06	0.78 ± 0.01	16.86 ± 0.17	0.69 ± 0.01
TTAR-9	7.60 ± 0.07	0.78 ± 0.01	15.54 ± 0.06	0.62 ± 0.01

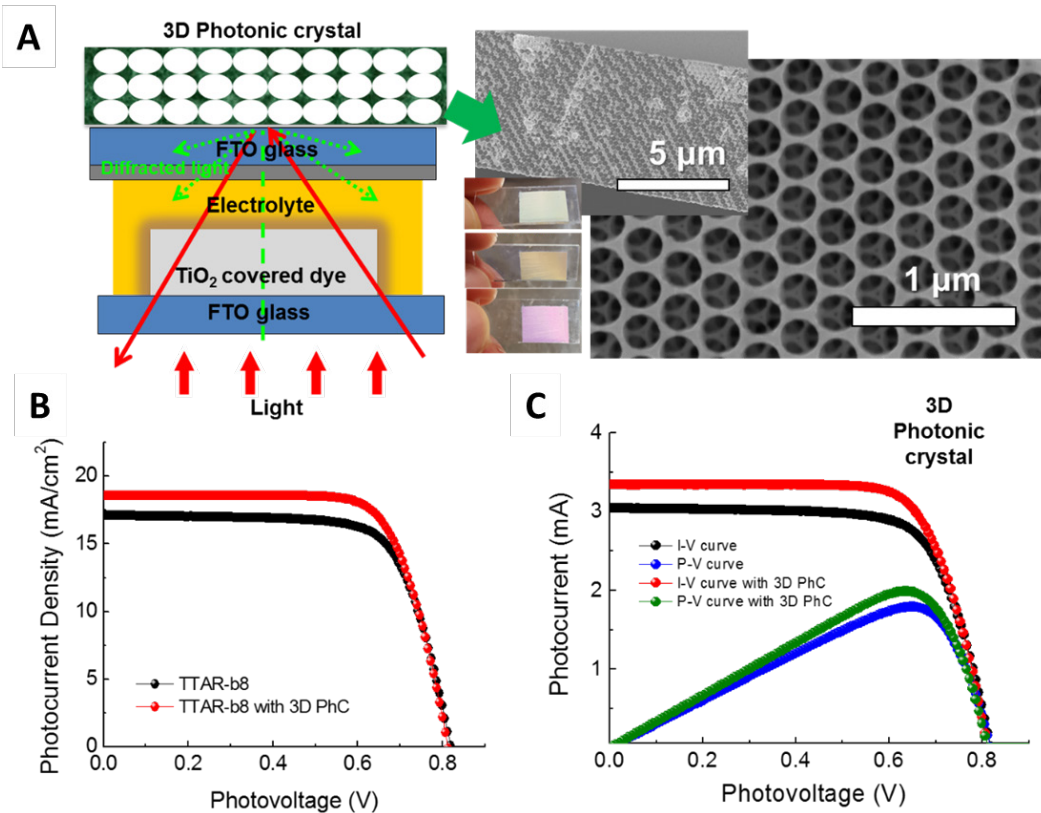


Figure 4.18. **A)** Configuration of the cell with the 3-D photonic crystals (inserted in photo- and SEM images of 3D PhC), **B)** The photocurrent current density–voltage (*J*-*V*) and **D**) power-voltage (*P*-*V*) characteristics of the DSSCs with **TTAR-b8** and 3D PC under 1 sun illumination (Adapted from Ezhumalai, et al.⁹¹).

Table 4.6. Photovoltaic parameters of the DSSCs with **TTAR-b8** and 3D PC under 1 sun illumination.

Dye	<i>V_{oc}</i> (V)	<i>J_{sc}</i> (mA cm ⁻²)	<i>FF</i> (%)	<i>η</i> (%)
TTAR-b8	0.817	17.12	71.96	10.08
TTAR-b8 with 3D PhC	0.811	18.79	73.31	11.18

The above results strongly suggest that morphology of dye assembly on TiO₂ is a key aspect in understanding such substantial difference in efficiencies of these three dyes. Therefore, we perform XRR studies of the three dyes on ALD deposited TiO₂ on SiO_x/Si.

For the XRR studies, 19 Å TiO₂ thin films with flat (low-roughness) surfaces were grown on piranha-cleaned Si/SiO₂ wafers by atomic layer deposition (TDMAT + H₂O). The derived films were then dipped in 0.3 mM solutions of the three separate dyes dissolved in DCM : CAN : t-Butanol = 8:1:1 for 24 h with subsequent washing with ACN and drying under a UHP N₂ stream.

Figure 4.19A shows normalized XRR data as a function of momentum transfer $q = \frac{4\pi}{\lambda} \sin \frac{\theta}{2}$ along with best fitting curves based on Parratt's recursion formulation for a slab model.⁹⁶ The electron density profiles for each of the model fits are shown Figure 4.19B. Table 4.7 lists the structural parameters of the dye films inferred from the XRR analysis.

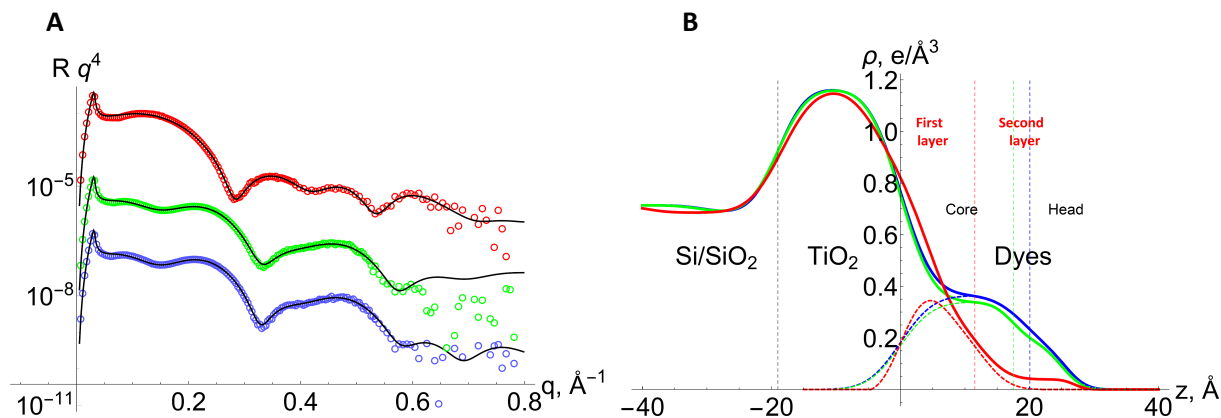


Figure 4.19. A) XRR experimental data (circles, red - TTAR-b8, green - TTAR-9, blue - TTAR-15) and best fitting curves (solid black lines), B) electron density profiles determined from the fits. Dashed lines indicate the density profiles of the dye layers after subtracting the TiO₂ profile (the red dashed line is for the layer adjacent to TiO₂).

Table 4.7. Dye layer parameters inferred from XRR determined electron density profiles.

Dye	Overall weighted thickness, Å	Head thickness, Å	Core thickness, Å	Head electron density, e/Å ³	Core electron density, e/Å ³	Air/head interface roughness, Å	Head/core interface roughness, Å	Core/TiO ₂ interface roughness, Å	TiO ₂ thickness, Å	Molecular footprint, Å ²
TTAR-b8*	27.0	15.4	11.6	0.04	0.35	~1.5 [†]	3.8	4.1	19.0 [‡]	118
TTAR-15	25.3	5.3	20.	0.20	0.37	2.3	4.0	4.0	19.0	74
TTAR-9	24.8	7.3	17.5	0.18	0.34	2.6	2.5	4.0	19.0	67

*Core here refers to the first layer and head to the second sparse layer.

[†]Not reliable.

[‡]Extrapolated from separate experiments.

Inspection of the XRR curves clearly indicates qualitative differences between the adsorbed branched-alkyl dye **TTAR-b8** dye and the two dyes with n-alkyl substituents, **TTAR-15** and **TTAR-9**. The latter two dyes have comparable molecular footprints, thicknesses equal to their molecular backbone lengths, and similar density profiles. Therefore, to occupy the same space the C15 tail must favor a more compact packing than the C9 dye, leading to greater distortions of the face-to-face stacking of the fused aromatic rings and thus less likelihood of pores in the dye monolayer. This morphology also manifests itself in a less pronounced head separation for **TTAR-15**. Such steric hindrance may decrease the excitation quenching probability on neighboring molecules and recombination by charge transfer through pores in the dye monolayer. In contrast, the **TTAR-b8** molecules are significantly tilted (angle with the surface normal is ~60°). XRR data fitting indicates a residual sparse second layer that is not removed by washing with pure solvent. This second layer covers approximately 10% of the surface, and is presumably a result of lateral inhomogeneity in the film, e.g. due to formation of patches (islands) or other form of aggregation which manifests itself in the inferred electron density profile as a sparse layer because of lateral averaging (Figure 4.20). The head group in the first denser layer is not distinguishable on electron density profile. These characteristics indicate a much stronger tendency for intermolecular hydrophobic attraction and a much higher level of face-to-face stacking distortion versus both **TTAR-15** and **TTAR-9**, and thus more efficient suppression of intermolecular quenching and prevention of pore formation in the first layer. These property trends correlate well with the observed monotonic increases in J_{SC} , V_{OC} , and η^{M} in the series **TTAR-9 → TTAR-15 → TTAR-b8**.

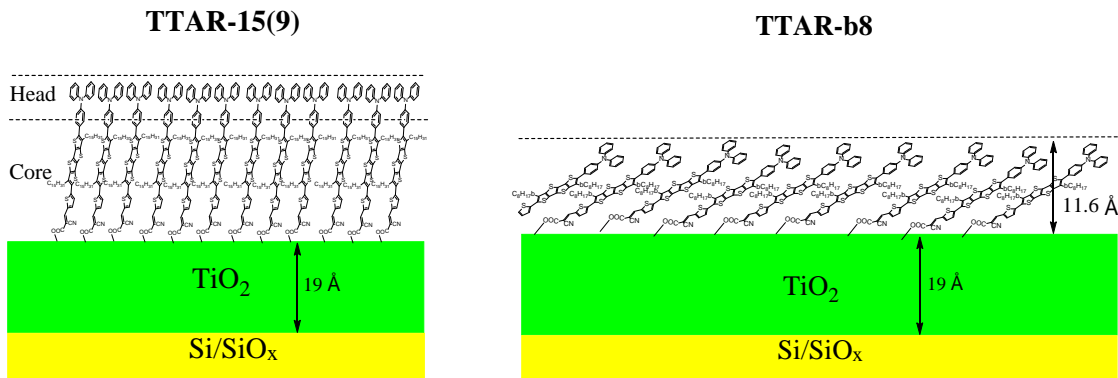


Figure 4.20. Schematic depictions of plausible models conforming to the deduced parameters and XRR determined profiles from Figure 4.19B for **TTAR-15 (TTAR-9)** and **TTAR-b8**.

4.4. Summary

The morphology and molecular packing of dye assemblies on the surface of mesoporous TiO_2 electrode is a key factor, alongside electronic structure, in determining the efficiency of dye sensitized solar cells (DSSC). To investigate the dye monolayer structure, we created a model smooth surface of TiO_2 by atomic layer deposition of titanium dioxide on hydroxylated silicon wafer and used X-ray reflectivity (XRR) technique to extract the electron density profiles along the normal to the TiO_2 surface. To obtain reliable parameters from XRR, the thickness of the TiO_2 should be of the same order as the expected dye thickness. We applied this method of investigation to two series of novel tetrathienoacene (TTAR) dyes of donor- π -acceptor design (TPA-TTAR-A). The first series inserted thiophene rings between three constituting moieties. TPA-TTAR-T-A dye with highest 10.1% efficiency had the tightest packing and smallest molecular footprint as revealed by XRR analysis. TPA-TTAR-A and TPA-T-TTAR-A had low thickness and high molecular footprint. This correlated with the conformational distortions introduced by the thiophene ring and their lower efficiencies. TPA-T-TTAR-T-A dye with two thiophene insertions had the second highest efficiency and the second lowest footprint.

The second series varied the structure of R chain to branched octyl, n-nonyl and n-pentadecyl radicals. The branched dye, which had the highest efficiency of 10.21%, exhibited strong hydrophobic intermolecular attraction, substantial tilting and frustration of face-to-face stacking and therefore lesser recombinational losses. We conclude that this contributed to the enhancement of its efficiency compared to normal alkyl dyes.

5. X-ray studies of perovskite films

5.1. X-ray study of 2D perovskites

Lead perovskites have bandgap (\sim 1.5-2.2eV) and electron-hole diffusion length (\sim 1 micron) well positioned for use as photoactive material in solar cells⁹⁷⁻¹⁰². These unique properties allowed achieving solar cell efficiencies over 20%¹⁰²⁻¹⁰³. For single junction solar cell the theoretical limit is 33.5%¹⁰⁴. However, lead perovskites, exemplified primarily by methylammonium lead perovskite (Figure 5.1), have environmental stability issues¹⁰⁵⁻¹¹¹, e.g. water vapor reacts with methylammonium lead perovskite and leads to its decomposition. To overcome the stability issue, layered perovskites (Ruddlesden–Popper phase of perovskites) have been explored as photoactive element of solar cells but with only poor results for efficiency^{109, 112-113}.

We studied two Ruddlesden–Popper perovskites¹¹⁴: $(BA)_2(MA)_2Pb_3I_{10}$ ($n = 3$) and $(BA)_2(MA)_3Pb_4I_{13}$ ($n = 4$), where BA = butylammonium and MA = methylammonium. The general stoichiometry of these compounds can be written as $(BA)_2(MA)_{n-1}Pb_nI_{3n+1}$, where $[(MA)_{n-1}Pb_nI_{3n+1}]^{2-}$ represents the inorganic layer sandwiched between organic *n*-butylammonium (BA) cations (Figure 5.2). The thickness of each perovskite layer can be adjusted by varying the proportion of BA.

The obstacle in attaining higher efficiency is the parallel alignment of insulator organic spacer to the surface of the electrode. A new method suggested by M. Kanatzidis, et al.¹¹⁴ overcomes this problem and produces films with vertical alignment of organic spacers. This dramatically increased the efficiency, reaching 12.52% for $(BA)_2(MA)_3Pb_4I_{13}$ with long operational stability times. Over 60% of the efficiency is maintained for over 2250 hours under standard (AM1.5G) illumination, and with greater tolerance to 65% relative humidity compared to methylammonium lead perovskite. Encapsulated devices do not exhibit

degradation under constant AM1.5G illumination or high humidity. Below we describe the GIWAXS analyses that we performed to assess the orientation of these layered perovskite films.

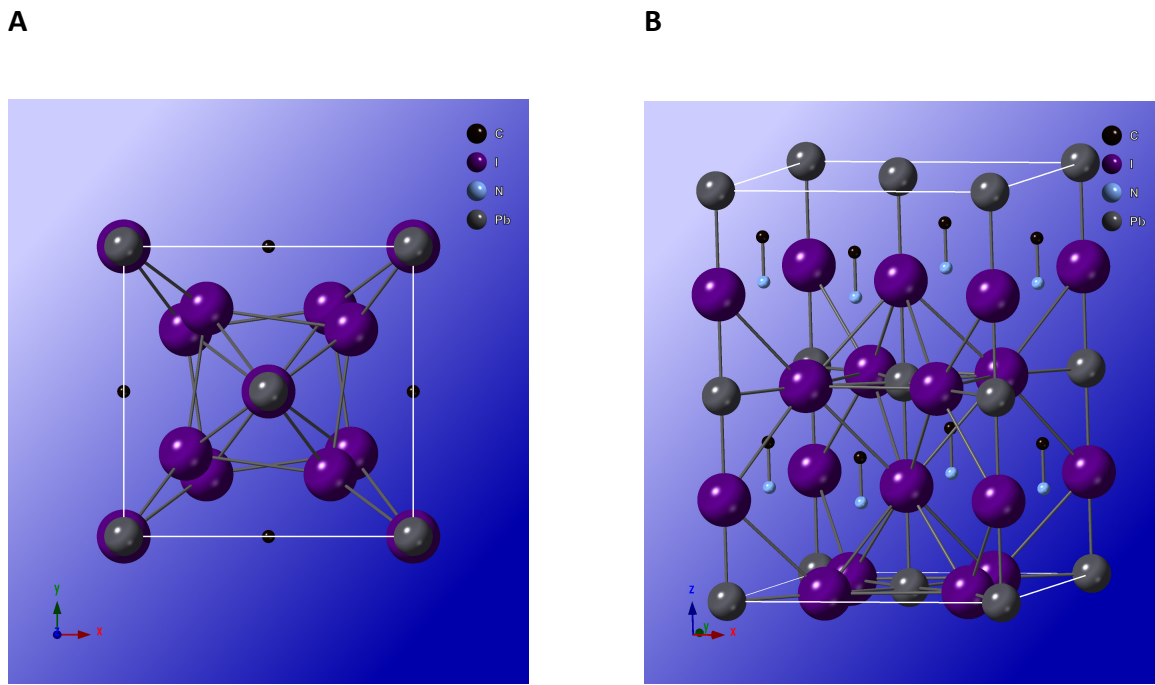


Figure 5.1. Unit cell structure of methylammonium lead perovskite ($\text{CH}_3\text{NH}_3\text{PbI}_3$). **A**) (001) view, **B**) side view. (I 4 c m, $a = 8.849 \text{ \AA}$, $c = 12.642 \text{ \AA}$).

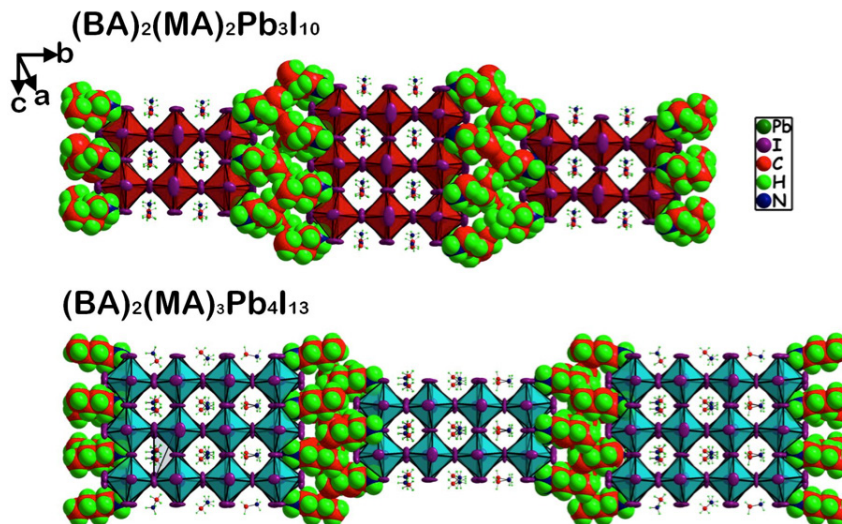


Figure 5.2. Lattice structure of $(\text{BA})_2(\text{MA})_{n-1}\text{Pb}_n\text{I}_{3n+1}$ for $n = 3, 4$. (Adapted from Tsai, et al.¹¹⁴)

5.1.1. Experimental methods

Pb_3I_{10} and Pb_4I_{13} were prepared¹¹⁴ (by the group of Prof M. Kanatzidis) with molar concentrations of 1.8 M, 0.9 M, 0.45 M, 0.225 M and 0.118 M of Pb^{2+} cations in anhydrous DMF. FTO/PEDOT:PSS substrates were prepared following refs Nie, et al.¹¹⁵ and Tsai, et al.¹¹⁶. FTO glasses were cleaned using an ultra-sonication bath in soap water and rinsed progressively with distilled water, acetone and isopropyl alcohol, and finally treated with oxygen plasma for 3 min. The PEDOT:PSS layer was then spin-coated onto the FTO substrates at 5,000 r.p.m. for 45 s as a hole-transporting layer. The coated substrates were then transferred to an argon-filled glovebox for device fabrication. The 2D perovskite solution was prepared by dissolving 0.025 mM 2D perovskite single crystal in DMF. The solution was then heated under continuous stirring at 70 °C for 30 min before device fabrication. For the film hot-casting process, the FTO/PEDOT:PSS substrates were first preheated from 30 °C to 150 °C on a hot plate for 10 min, right before spin-coating. These were immediately (within 5 s) transferred to the hot FTO/PEDOT:PSS substrates on the spin-coated ‘chunk’ (which is at room temperature), and 80 µl of precursor solution was dropped onto the hot substrate. The spin-coater was immediately started with a spin speed of 5,000 r.p.m. for 20 s without ramp; the colour of the thin film turned from pale yellow to brown in few seconds as the solvent escaped. After the spin-coater stopped, the substrates were quickly removed from it. The [6,6]-phenyl-C61-butyric acid methyl ester (PCBM) solution was prepared by dissolving 20 mg PCBM in 1 ml chlorobenzene. 50 µl of the PCBM solution was then dropped onto the perovskite-coated FTO/PEDOT substrate and spin-coated at 1,000 r.p.m. for 60 s to form a thin, electron-transporting layer. The metal electrodes (Al and Au) were deposited using a thermal evaporator with a shadow mast with a working area of 0.5 cm². GIWAXS measurements were carried out on Sector 8-ID-E at the Advanced Photon Source, Argonne National Laboratory.

5.1.2. GIWAXS analysis of $(BA)_2(MA)_2Pb_3I_{10}$ and $(BA)_2(MA)_3Pb_4I_{13}$ films

In order to probe the perovskite orientation with respect to the substrate (FTO/PEDOT:PSS) in the thin-film geometry we used GIWAXS measurements with synchrotron radiation source (Figure 5.3A,B). The resulting scattering patterns reveal two major characteristics for the films. The room-temperature (RT) cast films (Figure 5.3A) are comprised of diffraction rings with stronger intensities along certain extended arc segments indicating considerable randomness in the 3D orientation of the crystal domains (grains) within the polycrystalline film.

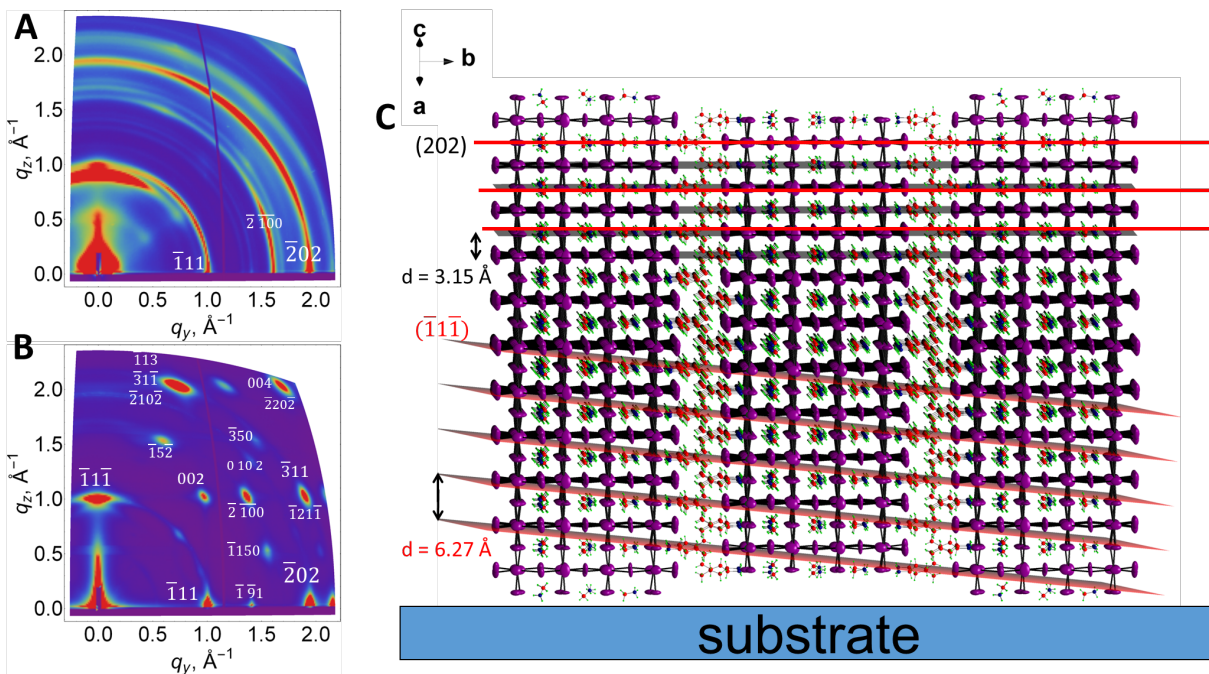


Figure 5.3. **A, B)** GIWAXS patterns for polycrystalline room-temperature-cast (**A**) and hot-cast (**B**) near-single-crystalline $(BA)_2(MA)_3Pb_4I_{13}$ perovskite films with Miller indices of the most prominent peaks shown in white. Color scale is proportional to X-ray scattering intensity, q is the wavevector transfer, q_z is perpendicular to the sample, q_y is parallel to both the sample and the detector. **C)** Schematic representation of the (101) orientation, along with the $(\bar{1}\bar{1}\bar{1})$ and (202) planes of a 2D perovskite crystal, consistent with the GIWAXS data.

In contrast, the hot cast films (Figure 5.3B), exhibit sharp, discrete Bragg spots along the same rings, indicating a textured polycrystalline film where the crystal domains are oriented with their (101) planes

parallel to the substrate surface (as shown in Figure 5.3C) and a 2D in-plane orientational randomness. This crystallographic determination came from indexing the observed Bragg peaks in Figure 5.3B using a simulated diffraction pattern from the orthorhombic structure described above.

Crystallographic data allows us to calculate the intensities of diffracted beams from various Bragg planes. This can be performed for example by *SingleCrystal* software. By using the obtained(hkl) → I list we can reconstruct the GIWAXS pattern of oriented polycrystalline powder. Below we will discuss the mathematical machinery for the GIWAXS pattern simulation of general triclinic lattice and its application to the case of 2D layered perovskite.

Let's assume the crystal is oriented with the plane $p_n = (h_n, k_n, l_n)$ parallel to the substrate and denote unit cell parameters by $a, b, c, \alpha, \beta, \gamma$. We orient the y axis of the real space along the side b (Figure 5.4). In this cartesian frame the vectors of unit cell sides can be written as:

$$\vec{a} = a \cdot \{\sin \gamma, \cos \gamma, 0\}$$

$$\vec{b} = b \cdot \{0, 1, 0\} \quad (5.1)$$

$$\vec{c} = \{c_x, c_y, c_z\}, \text{ with } \begin{cases} c_x = \frac{c}{\sin \gamma} (\cos \beta - \cos \alpha \cos \gamma) \\ c_y = c \cos \gamma \\ c_z = \sqrt{c - c_x^2 - c_y^2} \end{cases}$$

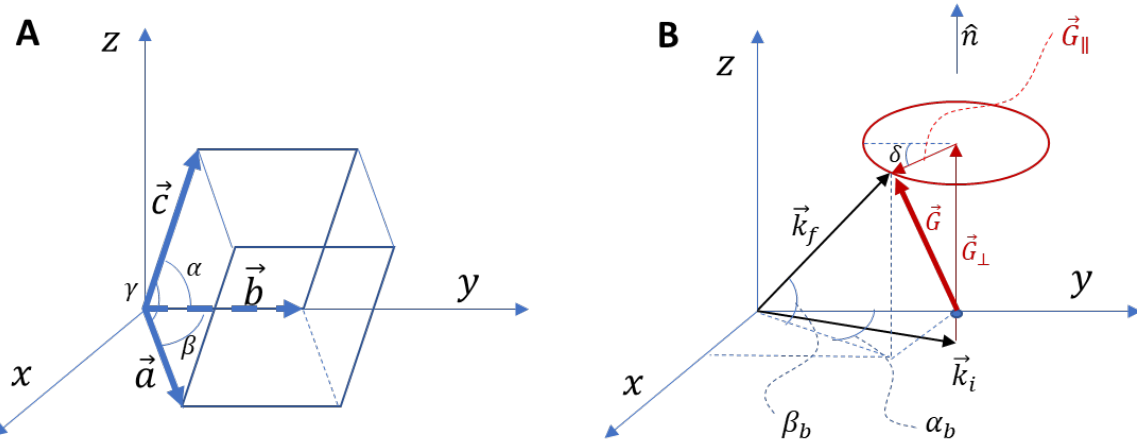


Figure 5.4. A) Triclinic unit cell embedded in the Cartesian frame, B) Laue condition for a polycrystalline powder oriented with the plane $p_n \perp \hat{n}$.

By writing the volume of the unit cell as $v_c = \vec{a} \cdot [\vec{b} \times \vec{c}]$, reciprocal lattice vectors can be cast in a usual form:

$$\begin{aligned}\vec{a}^* &= \frac{2\pi}{v_c} [\vec{b} \times \vec{c}] \\ \vec{b}^* &= \frac{2\pi}{v_c} [\vec{c} \times \vec{a}] \\ \vec{c}^* &= \frac{2\pi}{v_c} [\vec{a} \times \vec{b}]\end{aligned}\tag{5.2}$$

$$\vec{G} = h\vec{a}^* + k\vec{b}^* + l\vec{c}^*$$

The normal vector can be express through the Miller indices of the plane:

$$\begin{aligned}\vec{n} &= \left\{ \frac{h_p}{a}, \frac{k_p}{b}, \frac{l_p}{c} \right\}, \\ \hat{n} &= \frac{\vec{n}}{\|\vec{n}\|}.\end{aligned}\tag{5.3}$$

This allows us to write the parallel and perpendicular to the substrate components of the general reciprocal lattice vector as the following:

$$G_{\perp} = \vec{G} \cdot \hat{n},$$

$$G_{\parallel} = \sqrt{\vec{G}^2 - G_{\perp}^2}.$$

These two components of the reciprocal lattice vector are sufficient to write the Laue condition $\vec{q} = \vec{G}$

in terms of $q_r = \sqrt{q_x^2 + q_y^2}$ and q_z , i.e. $G_{\parallel} = q_r$ and $G_{\perp} = q_z$. To derive the angles of the scattered beam

we need to take into account the incident angle. With the incident and scattered wavevectors denoted by \vec{k}_i and \vec{k}_f , respectively, the Laue condition $\vec{k}_f - \vec{k}_i = \vec{G}$ in that case leads to the following system of

equations for the diffraction condition $\left(k = \frac{2\pi}{\lambda}\right)$ (Figure 5.4B):

$$\begin{cases} G_{\parallel} \sin \delta = k \cos \beta_b \sin \alpha_b \\ -G_{\parallel} \cos \delta = k (\cos \beta_b \cos \alpha_b - \cos \alpha_i) \\ G_{\perp} = k (\sin \beta_b + \sin \alpha_i) \end{cases} \quad (5.4)$$

Angle δ can be eliminated from this system of equations and solved for the scattered beam angles α_b and β_b :

$$\alpha_b = \arccos \left[\left(2 \cos \alpha_i \sqrt{1 - \left(\frac{G_{\perp}}{k} - \sin \alpha_i \right)^2} \right)^{-1} \left(1 + (\cos \alpha_i)^2 - \frac{G_{\parallel}^2}{k^2} - \left(\frac{G_{\perp}}{k} - \sin \alpha_i \right)^2 \right) \right]$$

$$\beta_b = \arcsin \left(\frac{G_{\perp}}{k} - \sin \alpha_i \right) \quad (5.5)$$

Wavevector transfer components then can be written as the following:

$$q_y = k \cos \beta_b \sin \alpha_b$$

$$q_z = k (\sin \beta_b + \sin \alpha_i) \quad (5.6)$$

To summarize the above formalism: given a specific orientation of the film, characterized by substrate parallel plane p_n , and for each reciprocal lattice vector \vec{G}_{hkl} we found the angles of the diffracted beam as well as its location on the detector.

It is convenient to work in polar coordinates, so we define in the Cartesian frame $\{q_y, q_z\}$ new polar variables: $q_{\theta,hkl} = \sqrt{q_{y,hkl}^2 + q_{z,hkl}^2}$ and $\theta_{hkl} = \arctan \frac{q_{z,hkl}}{q_{y,hkl}}$. Notice, θ_{hkl} here is not the grazing incidence angle. Let's assume that the peak profiles in both $\hat{\theta}$ (azimuthal) and \hat{q}_θ (radial) directions are given by Gaussian distribution and denote by $\mathcal{N}_x(\mu, \sigma)$ the probability density function of a Gaussian distribution with mean μ and variance σ^2 . The variance σ_θ of the variable θ will primarily characterize the orientational spread of the film, i.e. the distribution width of \hat{n} , while the variance σ_q of q_θ is related to the domain size of the polycrystalline powder through Scherrer formula. The latter can be stated in the reciprocal space by the following expression:

$$D = \frac{2\pi k}{\Delta q}, \quad (5.7)$$

where Δq is the integral width of the 1D diffraction peak and k is a constant depending on the shape of the crystallite. For a diffraction peak of Gaussian shape $\Delta q = \sqrt{2\pi}\sigma$, hence the Scherrer formula (5.7) can be recast in the following form:

$$D = \frac{\sqrt{2\pi}k}{\sigma} \quad (5.8)$$

The intensity of the diffraction can then be written as:

$$I(q_\theta, \theta) = \sum_{hkl} I_{hkl} \mathcal{N}_{q_\theta}(q_{\theta,hkl}, \sigma_\theta) \mathcal{N}_\theta(\theta_{hkl}, \sigma_q) \quad (5.9)$$

Implementation of the above formalism for simulation of GIWAXS pattern is described in Appendix C. Figure 5.5 depicts the simulated pattern of $(BA)_2(MA)_3Pb_4I_{13}$ perovskite with its (101) plane parallel to the substrate.

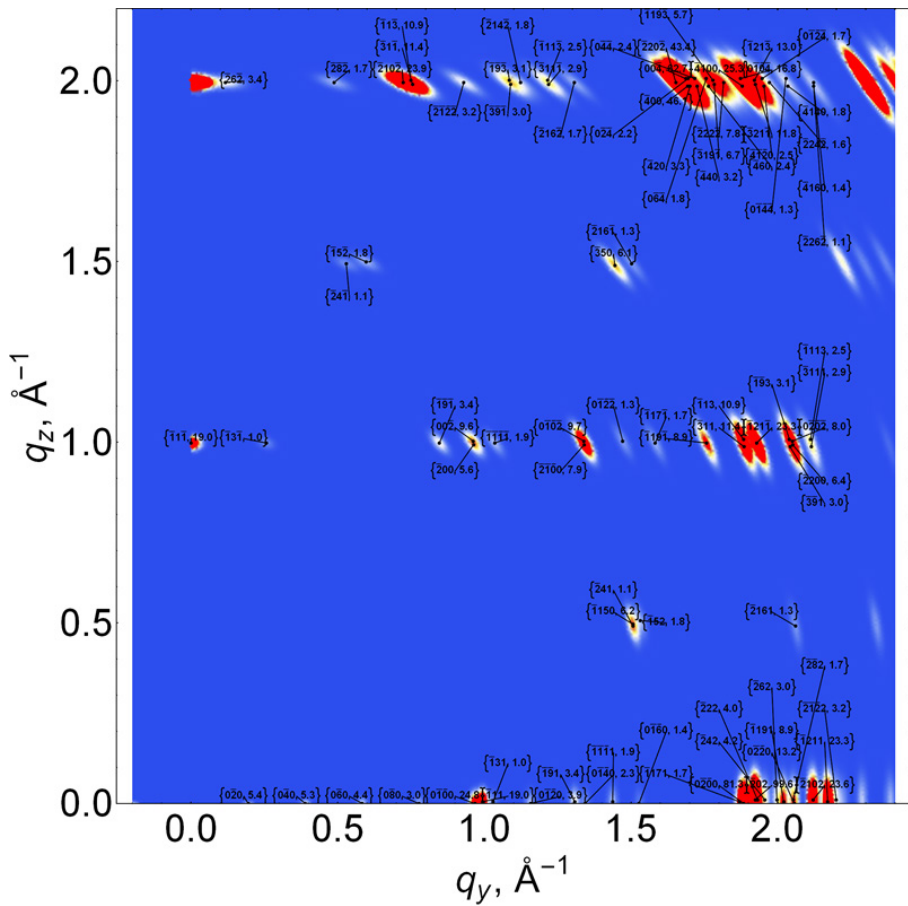


Figure 5.5. Simulated GIWAXS pattern for $(BA)_2(MA)_3PbI_{13}$ with (101) plane parallel to the substrate. Labels have the following format: {Miller indices hkl , intensity in arbitrary units}.

5.2. Dependence of the phase transition temperature of $\text{CH}_3\text{NH}_3\text{PbI}_3$ on HI additive

As mentioned above, methylammonium lead iodide ($\text{CH}_3\text{NH}_3^+\text{PbI}_3^-$) and other perovskites are intensely investigated as photoactive materials in solar cells¹¹⁷⁻¹²⁹. Part of the research effort has focused on improving the perovskite film morphology, optimizing charge extraction layers of the cell and the device structure in general, with resulting enhancements in efficiency reaching 22.1%. Optimizing morphology led to various fabrication methods such as: I) one-step solution methods^{125, 127}, II) vapor-assisted solution processes¹³⁰⁻¹³¹, III) sequential deposition¹³², IV) dual vapor deposition¹³³, and V) hot-casting¹³⁴.

One-step technique involves simple spin-casting from a solution of precursor salts with subsequent low temperature annealing. This relatively simple method lends itself to commercialization. However, the resulting non-uniformity of the film is a major hurdle on that route. Methods have been suggested to remedy this problem by: (1) composition engineering¹³⁵⁻¹³⁶, (2) solvent-engineering¹³⁷⁻¹³⁹, (3) tuning annealing conditions¹⁴⁰⁻¹⁴¹, and (4) incorporation of additives. Diverse number of additives have been explored: organic small molecules such as 1,8-diiodooctane¹⁴² and 1,3-bis[3,5-di(pyridin-3-yl)phenyl]benzene¹⁴³, halide salts such as $\text{CH}_3\text{NH}_3^+\text{Cl}^-$ ¹⁴⁴ and NH_4^+Cl^- ¹⁴⁵, and acids such as hydroiodic acid (HI)¹⁴⁶⁻¹⁴⁷ and hydrochloric acid (HCl)¹⁴⁸. PCEs of thus built devices were enhanced by as much as ~15% compared to simple one-step spin-casting.

In this work¹⁴⁹ we will consider the effect of HI on methylammonium lead perovskite films. Hydroiodic acid additive not only improves the morphology but also affects the electronic and crystal structure of the film. HI is a fairly reactive agent, forming HPbI_3 when precipitating PbI_2 from concentrated aqueous HI solution¹⁵⁰. HI incorporated perovskite solar cells have ~15% PCE.

HI additive modifies $\text{CH}_3\text{NH}_3\text{PbI}_3$ phases at room temperature depending on the HI concentration: the usual tetragonal β -phase is obtained at low acid concentrations, the more symmetrical pseudo-cubic α -phase is obtained at high acid concentrations. In the absence of additives, this transition is known to occur at ~57 °C in both the bulk material and thin films.¹⁵¹⁻¹⁵² With increase of the HI concentration the phase transition temperature shifts downward. 25% HI leads to formation of symmetric cubic lattice already at the room temperature. We will discuss below the lattice structure of these two phases and afterwards, in situ variable temperature XRR on the perovskite films with different HI concentrations that we performed to show the gradual decrease in the phase transition temperature.

5.2.1. Halide perovskites lattice structure

In halide perovskites (AMX_3 , where $\text{A}^+ = \text{Cs}^+, \text{CH}_3\text{NH}_3^+, \text{HC}(\text{NH}_2)_2^+$, $\text{M}^{2+} = \text{Ge}^{2+}, \text{Sn}^{2+}, \text{Pb}^{2+}$; and $\text{X}^- = \text{Cl}^-, \text{Br}^-$, I^-) $[\text{MX}_6]^{4-}$ octahedral fragments merge by their vertices to form a crystal lattice with voids filled by A^+ cations¹⁵³ (Figure 5.6). For ideal cubic symmetry, all $\text{M}-\text{X}-\text{M}$ angles are 180° , and the lattice is cubic. Deviations from the ideal cubic phase occur when the $\text{M}-\text{X}-\text{M}$ angles differ from 180° in the ab plane. This can be caused by exposure to heat¹⁵⁴ and/or pressure,^{129, 151, 155} resulting in contraction or expansion of the $[\text{MX}_3]^-$ arrangement. Structures with $\text{M}-\text{X}-\text{M}$ angles down to 150° have been achieved at low temperatures¹²⁰. But below $\sim 150^\circ$, the perovskite becomes unstable and phase transitions either into amorphous or other lattices^{120, 129, 151}. In the case of hybrid organic-inorganic halide perovskites, e.g., $\text{CH}_3\text{NH}_3\text{PbI}_3$, the highest symmetry crystal structure is pseudo-cubic (α -phase, $P4mm$ space group) as a result of the asymmetric cation shape, which can still be considered as cubic due to rotational averaging of the cations^{154, 156}. At room temperature, $\text{CH}_3\text{NH}_3\text{PbI}_3$ structure has $\text{M}-\text{X}-\text{M}$ angles equal to 163.6° as the pores are not large enough to fully accommodate the cation. This results in tetragonal β -phase of $I4cm$ space group (Figure 5.6). X-ray diffraction and calorimetric measurements show that $\text{CH}_3\text{NH}_3\text{PbI}_3$ undergoes a tetragonal to cubic phase transition between 42°C and 57°C ¹⁵⁶⁻¹⁵⁸, where thermal expansion and $\text{Pb}-\text{I}$ bond vibrations realign $\text{Pb}-\text{I}-\text{Pb}$ angles back to $\sim 180^\circ$ (Figure 5.6). In the pseudocubic phase, while the cell volume contracts, the organic cation is accommodated in the octahedral cage due to rapid, thermally activated rotation of the organic cation¹⁵⁹. Upon cooling, thermal motion is being suppressed, and the organic cation motion freezes below $\sim 160\text{ K}$, resulting in further distortions of the metal halide frame and lattice symmetry reduction to orthorhombic space group $Pbn2_1$ ¹⁵⁴.

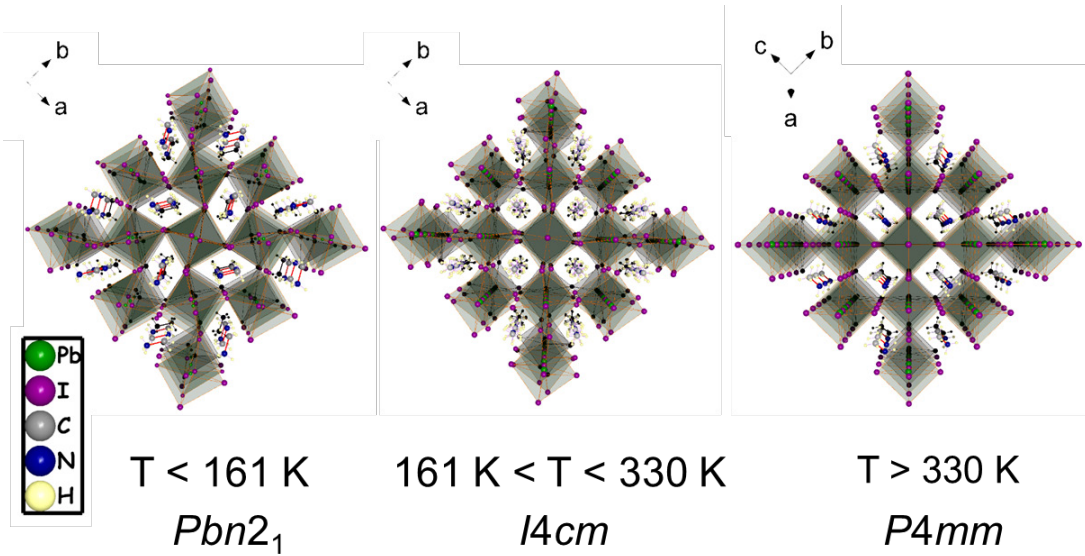


Figure 5.6. $\text{CH}_3\text{NH}_3\text{PbI}_3$ phase transition sequence. At high temperatures, it crystallizes in the pseudo-cubic phase ($P4mm$ space group). Upon cooling, it transforms into the tetragonal structure ($I4cm$ space group) at approximately 330 K. Lowering the temperature further results in an additional phase transition to the orthorhombic phase ($Pbn2_1$ space group) around 160 K¹⁵¹. (Adapted from Soe, et al.¹⁴⁹.)

5.2.2. Variable temperature XRR on $\text{CH}_3\text{NH}_3\text{PbI}_3$ films

Diffraction patterns of α - and β - phases differ primarily in the existence of (211) peak (Figure 5.7). The lack of this peak might, in principle, be indicative of the orientational preference of the deposited film. However, in the latter case other significant peaks would disappear too and that is not observed in the experiment (Figure 5.8). These considerations allow us to focus on *in situ* monitoring of the (211) peak while gradually increasing the temperature of the film. Thus collected powder diffraction patterns further reveal small shifts in the lattice parameter values which we attribute to the change in the strain of the grains.

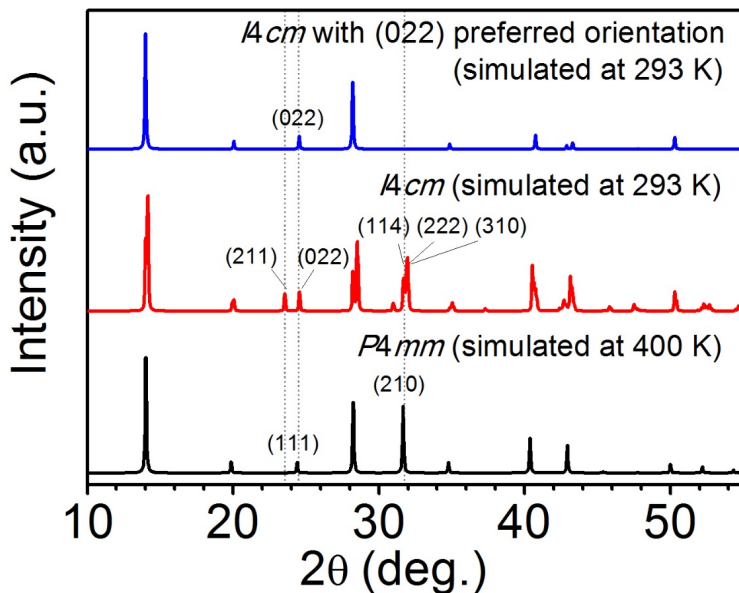


Figure 5.7. Simulated X-ray diffraction patterns of $\text{CH}_3\text{NH}_3\text{PbI}_3$: 3D powder of the tetragonal phase ($I4\text{cm}$) at 293 K (black), 3D powder of the pseudo-cubic phase ($P4\text{mm}$) at 400 K (red), and the ($I4\text{cm}$) textured phase with preferred orientation along the (022) plane at 293 K (blue)¹⁵³. The $I4\text{cm} \rightarrow P4\text{mm}$ transition results in suppression of the (211) reflection at 23.54° ($\text{Cu } K_\alpha$) whereas a preferred orientation in the $I4\text{cm}$ phase suppresses the (211) reflection as well as the (114), (222) and (310) reflections at 31.7° . (Adapted from Soe, et al.¹⁴⁹)

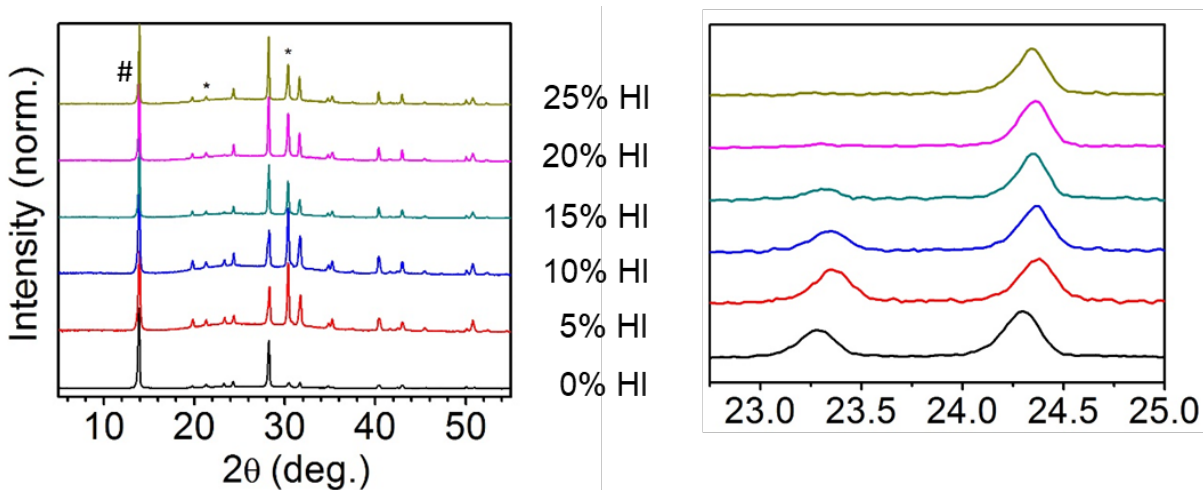


Figure 5.8. $\text{Cu } K_\alpha$ X-ray powder diffraction patterns of $\text{CH}_3\text{NH}_3\text{PbI}_3$ films on ITO/PEDOT:PSS prepared with the indicated HI concentrations. The * asterisks represent ITO peaks from the substrate. The # represents PbI_2 peak. The intensity is normalized to that of (110) reflection at 13.9° . (Adapted from Soe, et al.¹⁴⁹, performed by Chan Soe.)

5.2.2.1. Experimental method

In situ variable-temperature XRR: X-ray reflectivity θ - 2θ scans were performed on a Rigaku Smartlab instrument at a Cu K_{α} radiation wavelength of $\lambda = 1.5418 \text{ \AA}$ with an Anton Paar DHS 1100 heating stage. The temperature was incremented in a stepwise manner and allowed to stabilize before data acquisition. Poisson counting error bars were used in fitting observed peaks to Gaussian function. XRR measurements were carried out with 2-3 °C step sizes.

5.2.2.2. Results

A series of thin films with 0-15% of HI was selected as representative. The temperature at which the characteristic (211) reflection of the *I4cm* phase at $2\theta = 23.3^\circ$ disappears is considered to be the phase transition point. The control film without the HI additive exhibits a phase transition near 61 °C, very close to the reported value of $\sim 57 \text{ }^\circ\text{C}$ ¹⁵⁶⁻¹⁵⁸. As can be seen in Figure 5.9 and Figure 5.10, the transition point shifts to lower temperatures as the HI concentration is increased, ultimately peak intensity reaching a level below the instrumental detection range. This systematic decrease clearly demonstrates how HI addition gradually changes the perovskite phase and stabilizes the high-temperature cubic structure at the room temperature at high HI concentrations.

The described unusual tetragonal to cubic phase transition at room temperature can be attributed to Schottky disorder¹⁶⁰ in the perovskite polycrystalline thin films and the existence of structural strain induced by HI addition when the crystallite sizes are in the micron range or less. This is a known effect for perovskites, e.g. in BaTiO₃ reduction in grain size lowers the tetragonal to cubic phase transition temperature from 120 °C to 25 °C¹⁶¹⁻¹⁶³. Additives substantially smoothen the perovskite film by creating finer more uniform crystallites but simultaneously raising the surface tension energy and thereby lattice strain, accompanied by increased number of lattice defects in the perovskite¹⁶². This effect has already

been observed for CsPbI_3 perovskite system which transitions from a yellow wide bandgap orthorhombic phase to a black cubic phase upon HI addition¹⁴⁷.

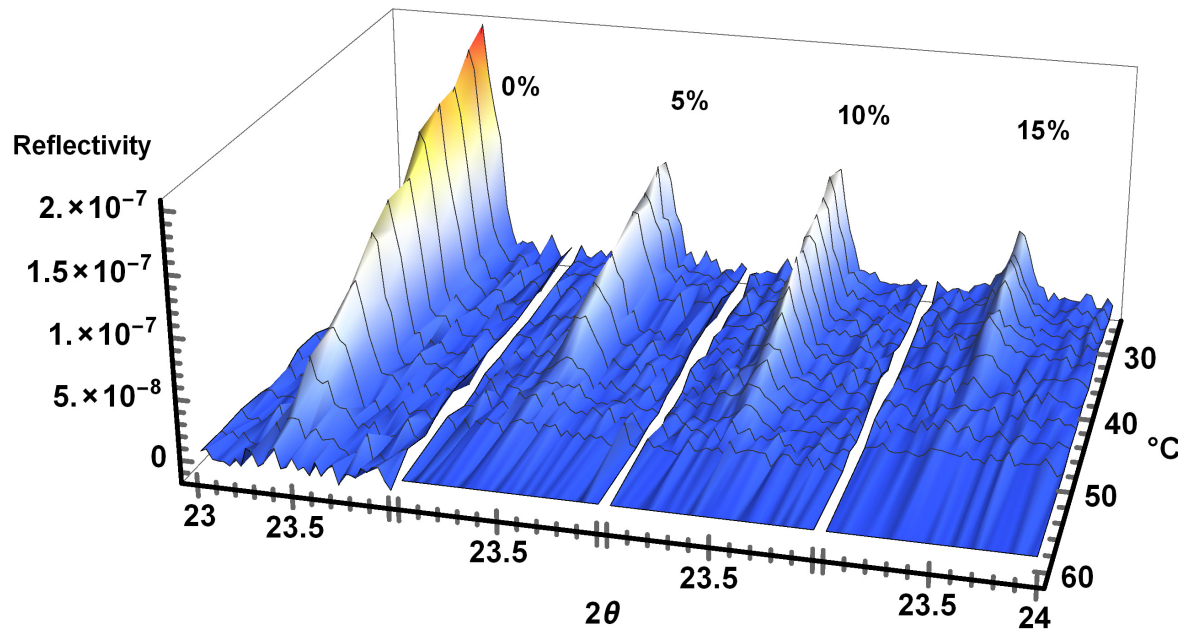


Figure 5.9. 2D view of peak reflectivity (intensity) vs. temperature and scattering angle for various HI weight fractions, of characteristic (211) reflection at $2\theta = 23.3^\circ$ for $\text{CH}_3\text{NH}_3^+\text{PbI}_3^-$ films, demonstrating the $I4cm \rightarrow P4mm$ phase transformation.

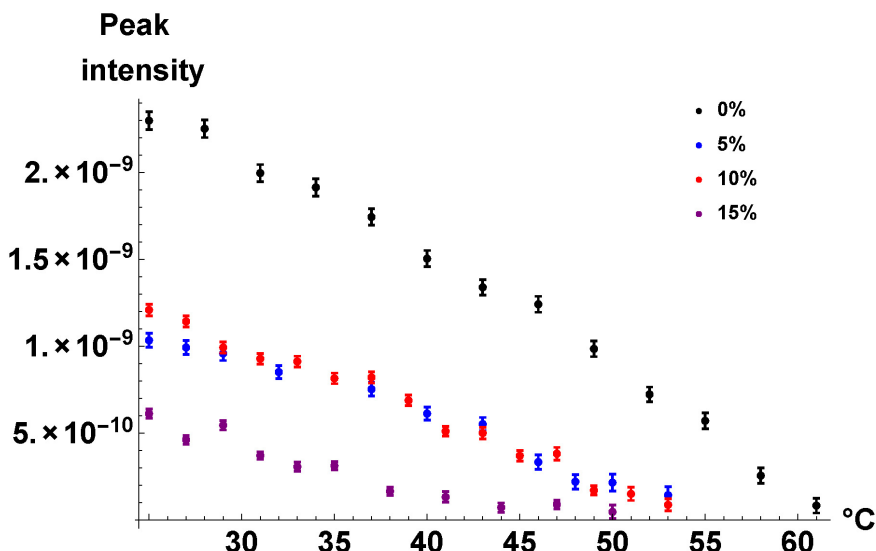


Figure 5.10. Background subtracted peak integral reflectivity vs. temperature

6. GIWAXS study of ternary organic photovoltaic films with fluorinated small molecule donor

Organic bulk heterojunction (BHJ) solar cells utilize a blend of various organic conjugated compounds as photoactive element. In a simple binary BHJ blend one of the components serves as a light harvesting agent which donates an electron to the other component (the acceptor). Thus generated electron can propagate through the film until it reaches the electrode and passes through the external loading. Bandgap of the donor compound and electron-hole mobility through the film play a crucial role in determining the cell efficiency. The mobility is determined largely by intermolecular interactions. In the majority of explored organic solar cells various polymers have been used as a donor component while the acceptor was primarily a fullerene derivative. Because of the spherical shape of the fullerene molecule it has the best geometry for capturing the propagating electron (Figure 6.1).

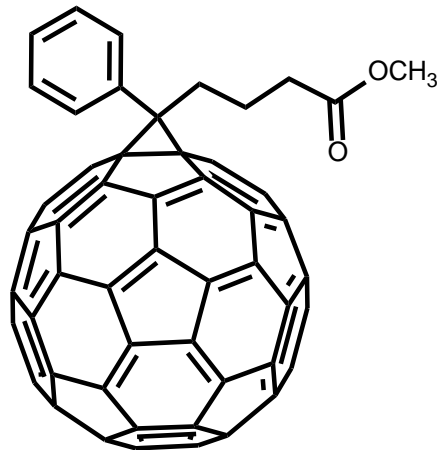


Figure 6.1. Phenyl-C₆₁-butyric acid methyl ester (PCBM)

The efficiencies achieved for organic photovoltaics (OPVs) have surpassed 12%^{8, 164-165} mark primarily thanks to optimization of bandgap, film morphology and other auxiliary components¹⁶⁶⁻¹⁷⁰. Small molecule donors (SMD), in contrast to their polymeric counterparts, do not have the long-range connectivity for

efficient electron conduction and have shown lower efficiencies¹⁷¹⁻¹⁷⁴ but recent SMDs nonetheless achieved over 9% efficiency¹⁷⁵.

It has been shown that fluorination of organic components can lead to substantial enhancement of charge mobility and device performance¹⁷⁶⁻¹⁷⁸, attributed primarily to the improvement of intermolecular connectivity. As a potent electron withdrawing group, fluorine atoms lower the HOMO energy level, thereby increasing the stability of the system¹⁷⁶⁻¹⁷⁸. Perfluorination of one of the aryl side-groups on a diaryl-substituted tetracene decreases lattice *d* spacings of tetracene crystal through formation of C–H···F hydrogen bonding, thereby enhancing photoconductivity and long-range order¹⁷⁹. It was further demonstrated that gradual fluorination of polymers reinforces π-π stacking and increases hole-mobility due to better orbital overlap¹⁸⁰. The role of fluorine atom in improving long-range connectivity also warrants our current study of SMD OPVs. To further improve the efficiency, three component (ternary) systems have been explored in the literature¹⁸¹⁻¹⁸³ with a mix of acceptor¹⁸⁴⁻¹⁸⁵ and donor¹⁸⁶⁻¹⁸⁹ compounds, resulting in tangible enhancements in the characteristics of thus created solar cells^{186, 190-194}. Unfortunately, these systems are complex, especially in the presence of various additives, e.g. 1,8-diiodooctane (DIO), diphenyl ether (DPE), used to overcome the immiscibility of components or poor film morphology^{184, 193, 195-196}.

One of the most well studied SMD compounds consists of benzodithiophene (BDT) unit with two diketopyrrolopyrrole (DPP) units to extend the conjugation^{171, 197-198}. The extended conjugation, which alters the bandgap, and improvements in film morphology have increased OPV performance¹⁹⁹⁻²⁰¹. Here we study²⁰²⁻²⁰³ two BDT-DPP₂ SMDs **PH** and **PF₂**, identical in the core structure but with varied degrees of fluorination on the conjugated side-chain (Figure 5.2).

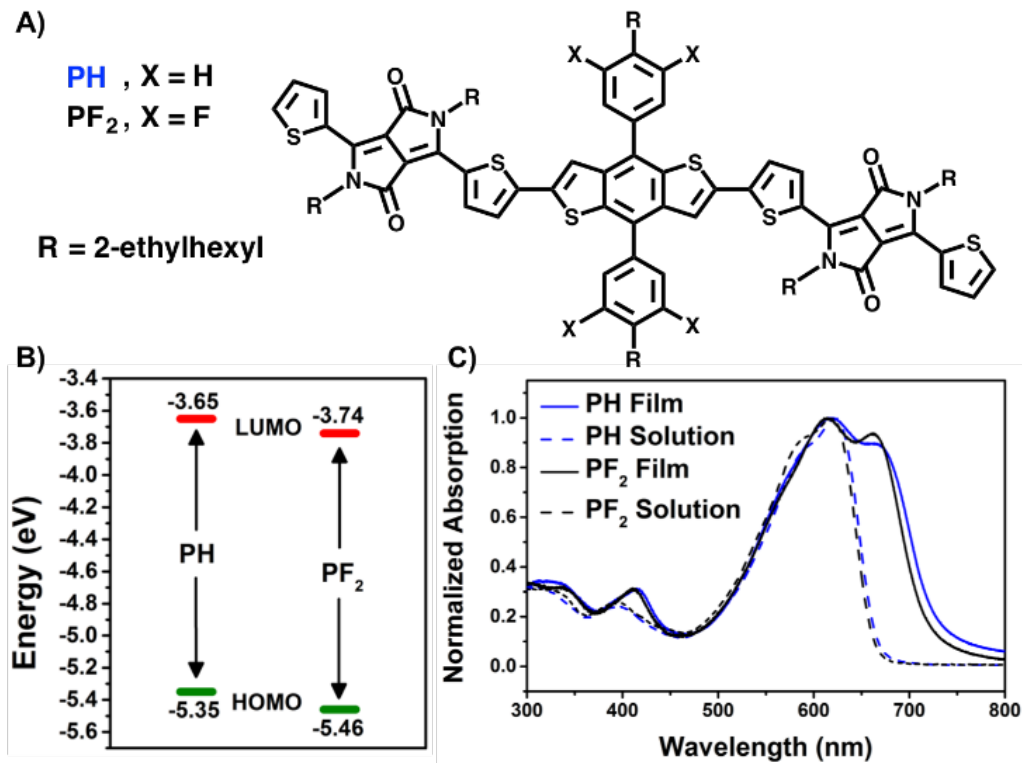


Figure 6.2. A) Molecular structures of **PH** and **PF₂** used in this study. B) CV-derived HOMO levels and optical absorption-derived LUMO levels of both donor materials. C) Solution and film UV-vis spectra of **PH** and **PF₂** exhibiting virtually identical bandgaps due to the minimal backbone effect of fluorination (Adapted from Eastham, et al.²⁰², synthesis performed by Nicholas Eastham).

Figure 6.2B and C show the effect of fluorination of **PH** and **PF₂** donors on their optical spectra and energy levels. They exhibit good photovoltaic performance in binary BHJ architecture and a 15% PCE improvement in the ternary architecture, among the highest performance enhancements reported to date for ternary OPVs²⁰⁴. **PH** and **PF₂** are miscible and have an alloy-like morphology^{190, 205}. V_{oc} is monotonically increasing with increase in **PF₂** concentration while J_{sc} peaks at 10:90 weight ratio (Table 6.1, Figure 6.3). The latter effect accounts for most of the increase in the PCE of the fabricated device. The reason for the improved J_{sc} can be understood by studying crystalline properties of the film with grazing incidence wide-angle X-ray scattering (GIWAXS). We correlate the increased short-circuit current of the OPV at the optimal ternary ratio to enhanced crystallinity in the photo-active layer. This result is the first

example of ternary system with fluorinated and non-fluorinated donor molecules mixed to induce higher crystallinity and improve overall performance.

Table 6.1. OPV performance of PH:PF₂:PC₆₁BM OPV devices at various donor component weight ratios.

PH:PF₂	100:0	75:25	50:50	25:75	15:85	10:90	5:95	0:100
<i>J_{sc}</i> (mA/cm ²)	8.36	7.51	8.06	8.19	8.74	9.18	8.71	7.81
<i>V_{oc}</i> (V)	0.833	0.862	0.878	0.882	0.918	0.927	0.932	0.944
<i>FF</i> (%)	59.6	62.6	61.4	62.1	59	57.6	55.6	57.8
PCE (%)^a	4.15 (4.04)	4.05 (4.03)	4.35 (4.34)	4.49 (4.40)	4.73 (4.65)	4.90 (4.85)	4.55 (4.51)	4.26 (4.21)

^aValues in parentheses are average PCE obtained from at least 10 devices

The most likely origin of enhanced light absorption in a system composed of identical bandgap materials is enhanced active layer crystallinity and generation of a larger absorption cross-section. GIWAXS measurements were performed on each ternary blend to observe any noticeable differences in the active layer structure (Figure 6.4). An increase in the number of microcrystalline phases at the optimal ternary ratio is observed upon analysis of these images, illustrated in the bubble plots in Figure 6.5. The size of the bubble is indicative of the size of the crystallite domains determined through Scherrer analysis. Upon deconvolution analysis of the broad PC₆₁BM peak at ~4.6 Å in ternary blends, the presence of new diffraction peaks at 4.13 Å, 4.42 Å, and 5.25 Å in the in-plane line-cut as well as 4.43 Å and 5.16 Å in the out-of-plane line-cut were observed in the 10:90 ratio films (Figure 6.7).

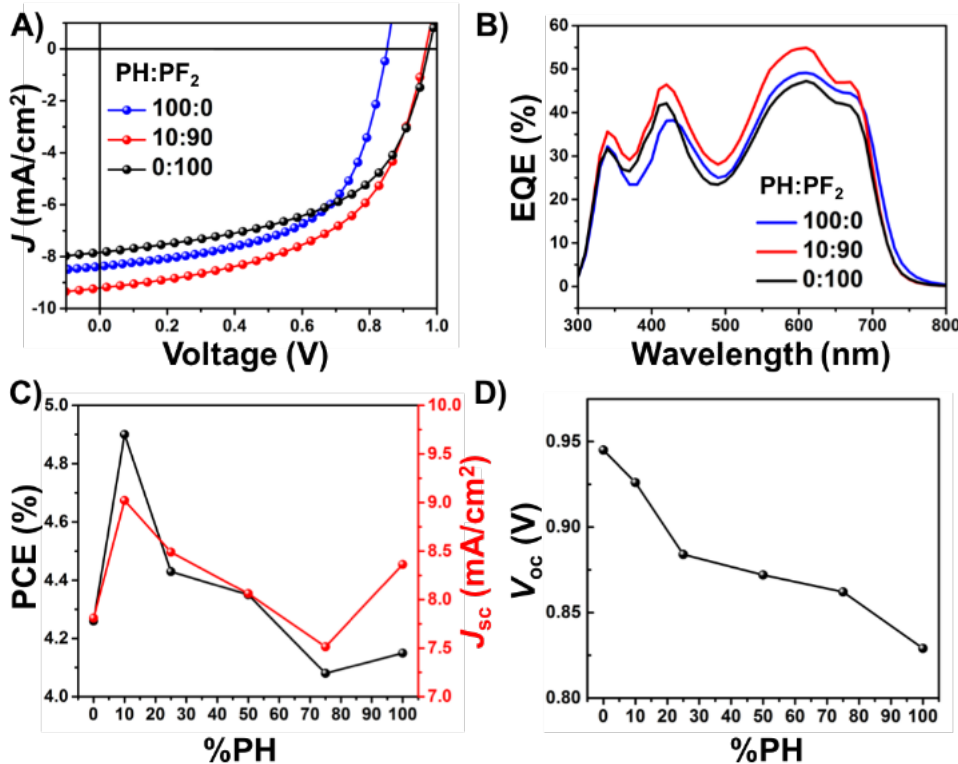


Figure 6.3. A) Current density versus voltage and B) EQE curves of solar cells based on binary and ternary blends of **PH** and **PF₂** with **PC₆₁BM**. C) Trends in PCE, J_{sc} , and D) V_{oc} with composition of ternary blend. (Adapted from Eastham, et al.²⁰².)

These peaks are not present in the pure **PH** or **PF₂** films and correspond to microcrystalline phases of ternary blends resulting from an optimal ratio of **PH:PF₂**. Furthermore, ratio of intensities of edge-on to face-on aligned stacks shows a sharp maximum at 10:90 weight blend for lamellar spacing (Figure 6.6). Increasing amounts of crystallinity in the ternary films, peaking at the optimal 10:90 **PH:PF₂** ratio, explains the increased absorption observed in UV-vis studies and the increased current in $J-V$ data.

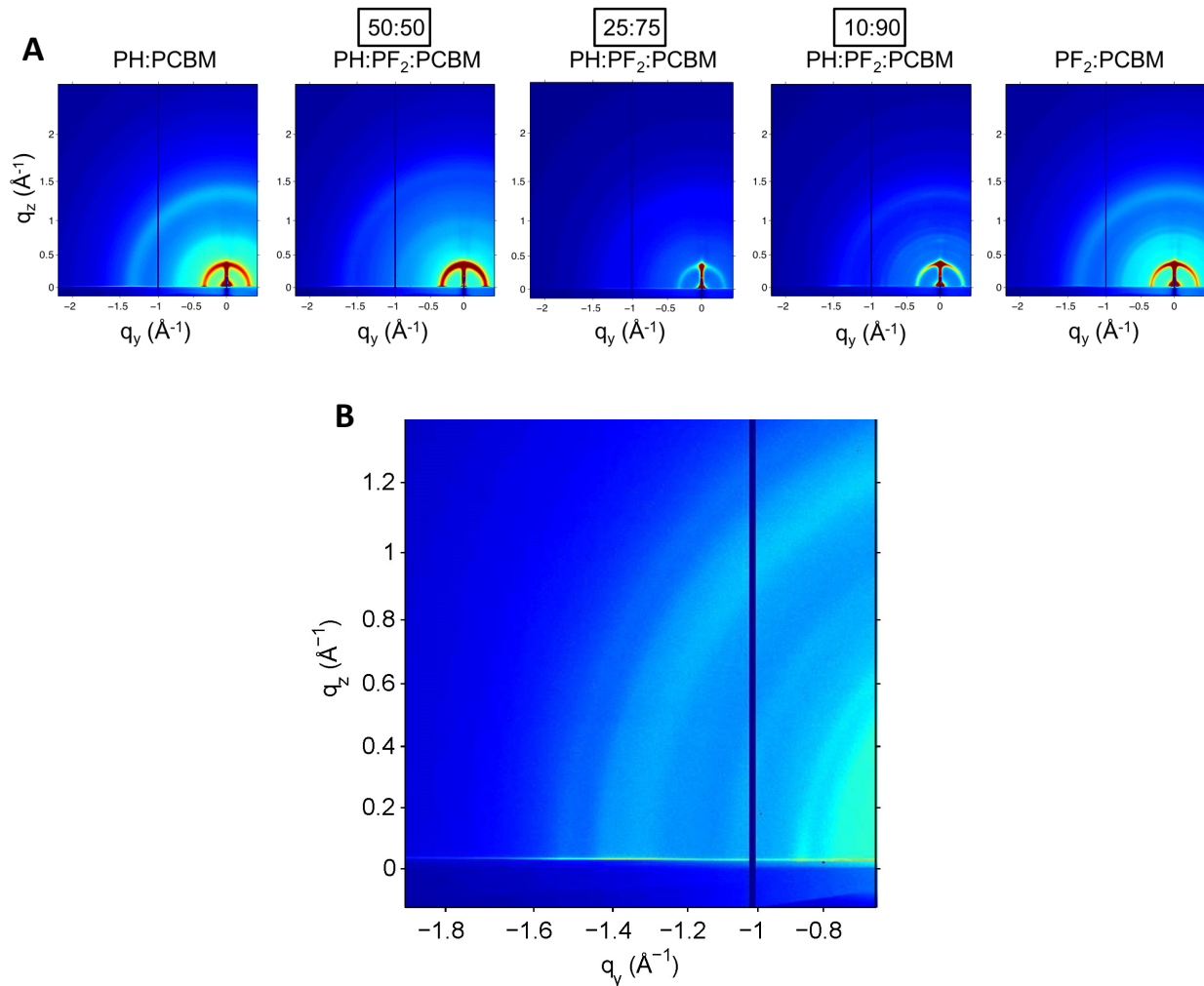


Figure 6.4. A) 2-D GIWAXS patterns of blend films containing PH, PF₂, and PCBM at various ternary ratios, B) zoomed GIWAXS pattern of 10:90 blend (Adapted from Eastham, et al.²⁰²).

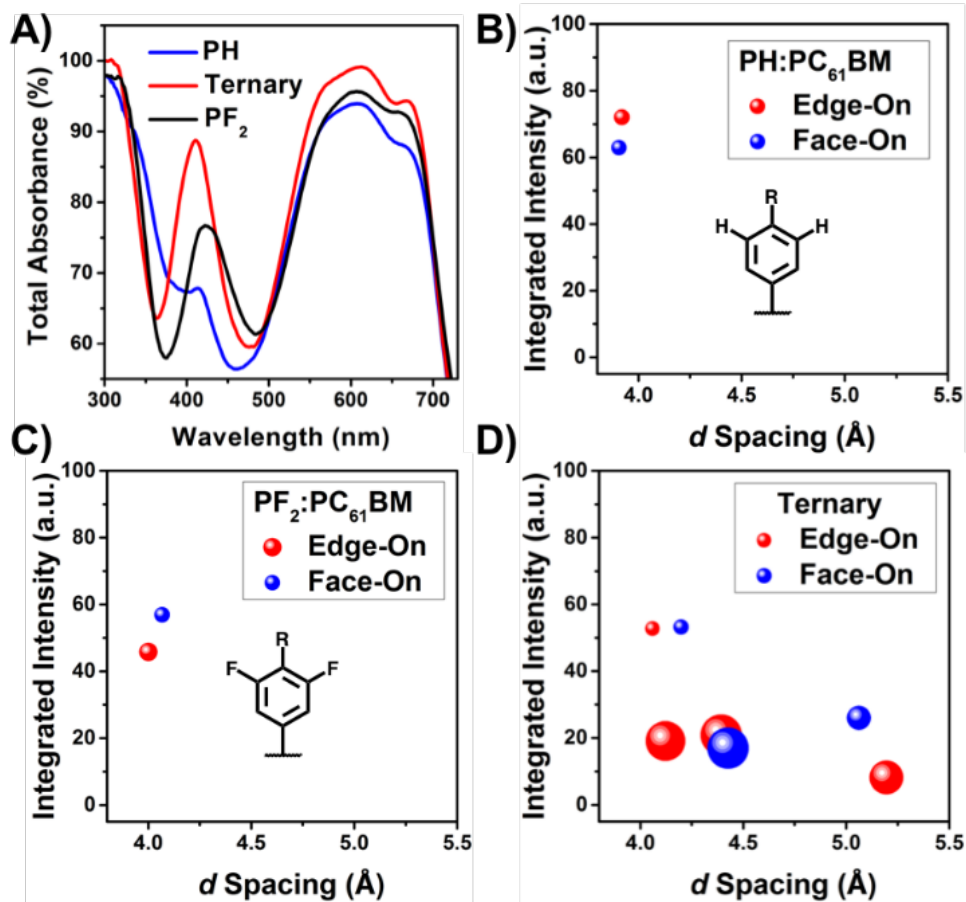


Figure 6.5. A) Diffuse reflectance UV-vis absorption measurements for binary and ternary **PH:PF2** blends with PC₆₁BM. 3-D Bubble plots depicting the spacing and intensity of crystalline diffractions and the relative size of the crystallite domains as determined by Scherrer analysis of B) **PH**, C) **PF₂**, and D) the optimal ternary blend (Adapted from Eastham, et al.²⁰²).

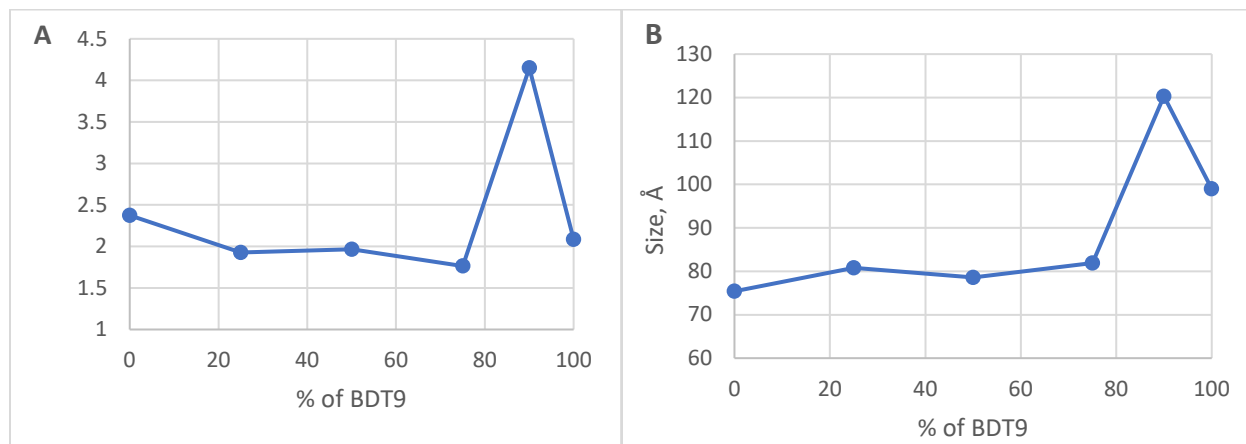


Figure 6.6. A) Ratio of intensities of edge-on to face-on aligned stacks for low q peak corresponding to the spacing \sim 17-18 Å, B) domain size in a direction parallel to substrate extracted by Scherrer formula.

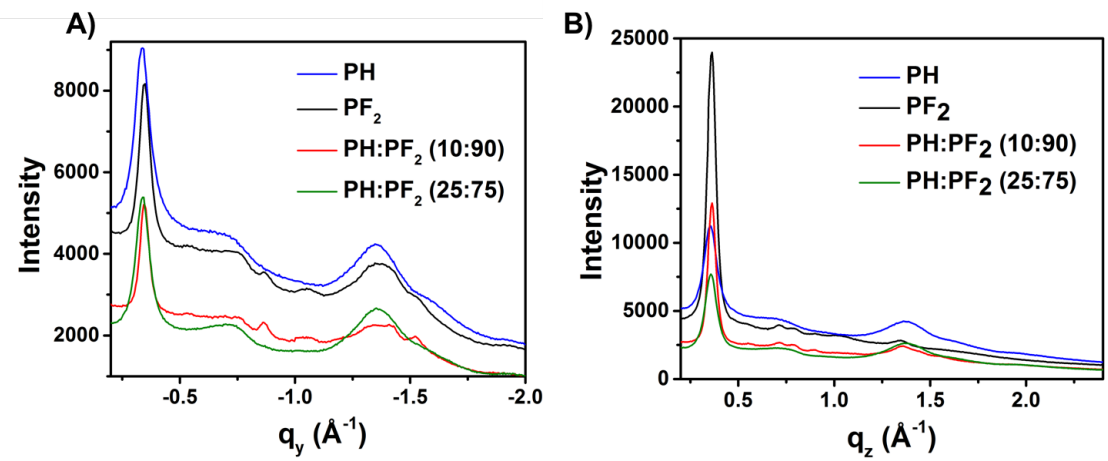


Figure 6.7. A) Horizontal ($q_z \approx 0$) and B) vertical ($q_r \approx 0$) line-cuts taken from the 2D GIWAXS patterns of ternary blend films containing PH, PF_2 and PCBM (Adapted from Eastham, et al.²⁰²).

7. Summary

Crystal lattice structure and assembly modes of photoactive materials, alongside electronic properties of individual constituent molecules, play a key role in determining the efficiency of solar devices. We investigated four types of photoactive systems: perylene monoimide (PMI) based nanoribbons/nanosheets for solar-to-fuel devices^{13, 52}, tetrathienoacene based dyes for dye sensitized solar cells^{83, 90}, 2D perovskite materials¹¹⁴ and fluorinated small molecule donor bulk heterojunction solar cells²⁰²⁻²⁰³.

PMI and its derivatives have the remarkable ability to self-assemble in water, forming ribbon-like structures of various aspect ratios. The nanoribbons absorb light and form excitons which can subsequently dissociate and allow the emerged electron to propagate through the ribbon until it reaches and transfers onto the water splitting catalyst present in the solution. The latter produces hydrogen gas. Modifications of the molecular structure lead to alteration of both the ribbon morphology, 2D crystal structure and packing modes of molecules. We used wide angle X-ray scattering (WAXS) technique to investigate 2D crystal structure and molecular packing of various PMI molecules, and small angle X-ray scattering for morphological study of nanoribbons at a larger scale. To interpret the diffraction pattern and extract the structural information, we created a simple slab model to represent the electron density distribution in individual PMI molecules, and parameterized form factor was constructed for the basis of the 2D unit cell. This simple model allowed efficient numerical implementation in fitting the model to the experimental data and finding optimal values of the parameters best reproducing the observed patterns. As a first step we applied it to fitting the grazing incidence wide angle X-ray scattering data for drop-cast dry samples and subsequently developed formalism for reproducing solution WAXS patterns of PMI nanosheets. The model fully accounted for asymmetric line-shape of the diffraction peaks due to 3D

averaging. This process yielded 2D unit cell parameters of various PMIs and their molecular packing modes, replicating the diffraction patterns remarkably well. The model was applied to MeO-PMI, HO-PMI, alkyl-PMIs and alkylamino-PMIs. The study revealed that the molecular packing of these 2D PMI lattices are in herringbone arrangement with various degrees of distortion. It further shone light on the 2D crystal structure of the most efficient PMIs. The analysis also revealed the lattice transformations occurring during a phase transition in n-propyl-PMI, one of the most efficiency PMIs. This allowed us to create a library of various PMI crystal structures, their efficiencies and other characteristics.

We further studied the morphology of tetrathienoacene (TTAR) based dye assemblies on TiO₂ surface by X-ray reflectivity (XRR). These dyes are an example of donor- π -bridge-acceptor systems used extensively in dye sensitized solar cells (DSSC). These devices have a potential of creating cheap and easily manufacturable solar cells with organic non-toxic photoactive element. To mimic the TiO₂ anatase surface of the active electrode in the solar cell and render it amenable to XRR experiments, we deposited by atomic layer deposition (ALD) smooth TiO₂ film of 16-20Å on hydrophilic SiO_x/Si wafer (with ~20Å native oxide). The latter was subsequently dipped into the dilute solution of the dyes in organic solvents. Subsequent washing with pure solvent yielded a dye monolayer. XRR experiments on a series of TTAR dyes revealed the impact of structural modifications of the molecule on the morphology of the film. Strategic insertions of thiophene rings between the donor and the bridge, or the acceptor and the bridge led to drastically different packings. The best packed system (thiophene between the acceptor and the bridge) yielded the highest efficiency in the DSSC: 10.1%, one of the highest among metal free dyes.

We then studied the effect of alkyl chain modifications in the best performing dye on the efficiency of the fabricated DSSC cell and morphology of the formed films on ALD TiO₂. Branching of the alkyl chain attached to the bridge was hypothesized to frustrate the face-to-face intermolecular interactions and thereby suppress intermolecular quenching of excitons. XRR demonstrated that branched octyl chain

increased the face-to-face distortions and enhanced the hydrophobic intermolecular adhesion. This correlated well with the enhanced efficiency of the branched TTAR dye.

In-plane grazing incidence diffraction patterns on these dye monolayers did not exhibit discernible peaks to indicate lateral ordering. Thus, XRR remains the most effective way of extracting relevant information about the morphology of these films.

Grazing incidence wide angle X-ray diffraction analysis has been performed on 2D layered perovskite films ($(BA)_2(MA)_{n-1}Pb_nI_{3n+1}$ for $n = 3, 4$) created by a new fabrication technique by Kanatzidis et al. This method overcame one of the key hurdles in using layered perovskites as stable photoactive element in solar cells, i.e. the parallel alignment of organic insulator layer with respect to the electrode surface. Perovskite films deposited by this method have perpendicular alignment of organic spacers, thereby allowing unimpeded flow of charge carriers. Indexing of GIWAXS pattern spots confirmed the perpendicular orientation of the organic spacer as well as high degree of crystallinity of the film. The achieved efficiency was 12.52% with no significant degradation of the encapsulated solar device.

GIWAXS analysis was performed on fluorinated benzodithiophene (BDT) derivatives with two diketopyrrolopyrrole (DPP) donor. Ternary mix of these donors in a proportion 1:9 showed highest efficiency in constructed bulk heterojunction solar cells. Diffraction pattern analysis revealed that this enhancement can attributed to higher degree of crystallinity and larger domain sizes for this particular proportion. We theorized that fluorination promoted better intermolecular interactions through hydrogen bonding. This manifest itself in higher UV-vis absorption and increased current on *J-V* curve of the cell.

X-ray scattering techniques are an indispensable tool for structural and morphological studies of photoactive materials. Their investigative power in this field will likely increase with the advancements in solar energy research.

References

1. Landau, L. D., *The classical theory of fields*. Elsevier: 2013; Vol. 2.
2. Als-Nielsen, J.; McMorrow, D., *Elements of modern X-ray physics*. John Wiley & Sons: 2011.
3. Warren, B. E., *X-ray Diffraction*. Courier Corporation: 1969.
4. Pershan, P. S.; Schlossman, M., *Liquid Surfaces and Interfaces: Synchrotron X-ray Methods*. Cambridge University Press: 2012.
5. Weingarten, A. S.; Kazantsev, R. V.; Palmer, L. C.; McClendon, M.; Koltonow, A. R.; Samuel, A. P.; Kiebala, D. J.; Wasielewski, M. R.; Stupp, S. I., Self-assembling hydrogel scaffolds for photocatalytic hydrogen production. *Nat. Chem.* **2014**, 6 (11), 964-70.
6. Hestand, N. J.; Kazantsev, R. V.; Weingarten, A. S.; Palmer, L. C.; Stupp, S. I.; Spano, F. C., Extended-Charge-Transfer Excitons in Crystalline Supramolecular Photocatalytic Scaffolds. *J. Am. Chem. Soc.* **2016**, 138 (36), 11762-74.
7. Weingarten, A. S.; Kazantsev, R. V.; Palmer, L. C.; Fairfield, D. J.; Koltonow, A. R.; Stupp, S. I., Supramolecular Packing Controls H₂ Photocatalysis in Chromophore Amphiphile Hydrogels. *J. Am. Chem. Soc.* **2015**, 137 (48), 15241-15246.
8. Tantakitti, F.; Boekhoven, J.; Wang, X.; Kazantsev, R. V.; Yu, T.; Li, J.; Zhuang, E.; Zandi, R.; Ortony, J. H.; Newcomb, C. J.; Palmer, L. C.; Shekhawat, G. S.; de la Cruz, M. O.; Schatz, G. C.; Stupp, S. I., Energy landscapes and functions of supramolecular systems. *Nat. Mat.* **2016**, 15 (4), 469-76.
9. Lefler, K. M.; Kim, C. H.; Wu, Y. L.; Wasielewski, M. R., Self-Assembly of Supramolecular Light-Harvesting Arrays from Symmetric Perylene-3,4-dicarboximide Trefoils. *J. Phys. Chem. Lett.* **2014**, 5 (9), 1608-15.

10. Würthner, F.; Saha-Möller, C. R.; Fimmel, B.; Ogi, S.; Leowanawat, P.; Schmidt, D., Perylene bisimide dye assemblies as archetype functional supramolecular materials. *Chem. Rev.* **2015**, *116* (3), 962-1052.
11. Laiho, A.; Smarsly, B. M.; Faul, C. F.; Ikkala, O., Macroscopically Aligned Ionic Self-Assembled Perylene-Surfactant Complexes within a Polymer Matrix. *Adv. Funct. Mater.* **2008**, *18* (13), 1890-1897.
12. Zakrevskyy, Y.; Faul, C. F.; Guan, Y.; Stumpe, J., Alignment of a Perylene-Based Ionic Self-Assembly Complex in Thermotropic and Lyotropic Liquid-Crystalline Phases. *Adv. Funct. Mater.* **2004**, *14* (9), 835-841.
13. Harutyunyan, B.; Dannenhoffer, A.; Kewalramani, S.; Aytun, T.; Fairfield, D. J.; Stupp, S. I.; Bedzyk, M. J., Molecular Packing of Amphiphilic Nanosheets Resolved by X-ray Scattering. *Journal of Physical Chemistry C* **2017**, *121* (2), 1047-1054.
14. Jiang, Z., GIXSGUI: a MATLAB toolbox for grazing-incidence X-ray scattering data visualization and reduction, and indexing of buried three-dimensional periodic nanostructured films. *J. Appl. Crystallogr.* **2015**, *48* (3), 917-926.
15. Li, T.; Senesi, A. J.; Lee, B., Small Angle X-ray Scattering for Nanoparticle Research. *Chem. Rev.* **2016**, *116* (18), 11128-80.
16. Bickerstaffe, A. K.; Cheah, N. P.; Clarke, S. M.; Parker, J. E.; Perdigon, A.; Messe, L.; Inaba, A., The crystalline structures of carboxylic acid monolayers adsorbed on graphite. *J. Phys. Chem. B* **2006**, *110* (11), 5570-5.
17. Brewer, A. Y.; Friscic, T.; Day, G. M.; Overvoorde, L. M.; Parker, J. E.; Richardson, C. N.; Clarke, S. M., The monolayer structure of 1,2-bis(4-pyridyl)ethylene physisorbed on a graphite surface. *Mol. Phys.* **2012**, *111* (1), 73-79.

18. Morishige, K.; Kawamura, K.; Kose, A., X-Ray-Diffraction Study of the Structure of a Monolayer Methanol Film Adsorbed on Graphite. *J. Chem. Phys.* **1990**, *93* (7), 5267-5270.
19. Knorr, K., Monolayers of polar methane derivatives physisorbed on graphite. *Phys. Rep.* **1992**, *214* (2), 113-157.
20. Yuan, Q.; Mannsfeld, S. C.; Tang, M. L.; Toney, M. F.; Luning, J.; Bao, Z., Thin film structure of tetraceno[2,3-b]thiophene characterized by grazing incidence X-ray scattering and near-edge X-ray absorption fine structure analysis. *J. Am. Chem. Soc.* **2008**, *130* (11), 3502-8.
21. Cheng, X.; Wang, K.; Huang, S.; Zhang, H.; Zhang, H.; Wang, Y., Organic Crystals with Near-Infrared Amplified Spontaneous Emissions Based on 2'-Hydroxychalcone Derivatives: Subtle Structure Modification but Great Property Change. *Angew. Chem.* **2015**, *127* (29), 8489-8493.
22. Mas-Torrent, M.; Durkut, M.; Hadley, P.; Ribas, X.; Rovira, C., High mobility of dithiophene-tetrathiafulvalene single-crystal organic field effect transistors. *J. Am. Chem. Soc.* **2004**, *126* (4), 984-5.
23. Mas-Torrent, M.; Hadley, P.; Bromley, S. T.; Ribas, X.; Tarrés, J.; Mas, M.; Molins, E.; Veciana, J.; Rovira, C., Correlation between crystal structure and mobility in organic field-effect transistors based on single crystals of tetrathiafulvalene derivatives. *J. Am. Chem. Soc.* **2004**, *126* (27), 8546-8553.
24. Sundar, V. C.; Zaumseil, J.; Podzorov, V.; Menard, E.; Willett, R. L.; Someya, T.; Gershenson, M. E.; Rogers, J. A., Elastomeric transistor stamps: reversible probing of charge transport in organic crystals. *Science* **2004**, *303* (5664), 1644-6.
25. Klebe, G.; Graser, F.; Hädicke, E.; Berndt, J., Crystallochromy as a solid-state effect: Correlation of molecular conformation, crystal packing and colour in perylene-3, 4: 9, 10-bis (dicarboximide) pigments. *Acta Crystallogr. Sect. B: Struct. Sci.* **1989**, *45* (1), 69-77.
26. Schildberg, H. P.; Lauter, H. J., Lineshape calculations for two-dimensional powder samples. *Surf. Sci.* **1989**, *208* (3), 507-532.

27. Dutta, P.; Sinha, S., Analytic form for the static structure factor for a finite two-dimensional harmonic lattice. *Phys. Rev. Lett.* **1981**, *47* (1), 50.
28. Youn, J.; Kewalramani, S.; Emery, J. D.; Shi, Y.; Zhang, S.; Chang, H. C.; Liang, Y. j.; Yeh, C. M.; Feng, C. Y.; Huang, H., Fused Thiophene Semiconductors: Crystal Structure–Film Microstructure Transistor Performance Correlations. *Advanced Functional Materials* **2013**, *23* (31), 3850-3865.
29. Appel, M. J.; Labarre, R.; Radulovic, D., On accelerated random search. *SIAM J. Optim.* **2004**, *14* (3), 708-731.
30. Zabinsky, Z. B., Random search algorithms. *Wiley Encyclopedia of Operations Research and Management Science* **2009**.
31. Zhao, H. M.; Pfister, J.; Settels, V.; Renz, M.; Kaupp, M.; Dehm, V. C.; Wurthner, F.; Fink, R. F.; Engels, B., Understanding ground- and excited-state properties of perylene tetracarboxylic acid bisimide crystals by means of quantum chemical computations. *J. Am. Chem. Soc.* **2009**, *131* (43), 15660-8.
32. Nolde, F.; Pisula, W.; Müller, S.; Kohl, C.; Müllen, K., Synthesis and Self-Organization of Core-Extended Perylene Tetracarboxdiimides with Branched Alkyl Substituents. *Chem. Mater.* **2006**, *18* (16), 3715-3725.
33. Wurthner, F., Perylene bisimide dyes as versatile building blocks for functional supramolecular architectures. *Chem Commun (Camb)* **2004**, *0* (14), 1564-79.
34. Hestand, N. J.; Tempelaar, R.; Knoester, J.; Jansen, T. L.; Spano, F. C., Exciton mobility control through sub- Å packing modifications in molecular crystals. *Phys. Rev. B* **2015**, *91* (19), 195315.
35. Gisslen, L.; Scholz, R., Crystallochromy of perylene pigments: Interference between Frenkel excitons and charge-transfer states. *Phys. Rev. B* **2009**, *80* (11), 115309.
36. Hestand, N. J.; Tempelaar, R.; Knoester, J.; Jansen, T. L. C.; Spano, F. C., Exciton mobility control through sub-Åpacking modifications in molecular crystals. *Phys. Rev. B* **2015**, *91* (19), 195315.

37. Zang, L.; Che, Y.; Moore, J. S., One-Dimensional Self-Assembly of Planar π -Conjugated Molecules: Adaptable Building Blocks for Organic Nanodevices. *Acc. Chem. Res.* **2008**, *41* (12), 1596-1608.
38. Würthner, F.; Saha-Möller, C. R.; Fimmel, B.; Ogi, S.; Leowanawat, P.; Schmidt, D., Perylene bisimide dye assemblies as archetype functional supramolecular materials. *Chem. Rev.* **2015**, *116* (3), 962-1052.
39. Tantakitti, F.; Boekhoven, J.; Wang, X.; Kazantsev, R. V.; Yu, T.; Li, J.; Zhuang, E.; Zandi, R.; Ortony, J. H.; Newcomb, C. J.; Palmer, L. C.; Shekhawat, G. S.; de la Cruz, M. O.; Schatz, G. C.; Stupp, S. I., Energy landscapes and functions of supramolecular systems. *Nat Mater* **2016**, *15* (4), 469-476.
40. Korevaar, P. A.; Schaefer, C.; de Greef, T. F. A.; Meijer, E. W., Controlling Chemical Self-Assembly by Solvent-Dependent Dynamics. *J. Am. Chem. Soc.* **2012**, *134* (32), 13482-13491.
41. Endo, M.; Fukui, T.; Jung, S. H.; Yagai, S.; Takeuchi, M.; Sugiyasu, K., Photoregulated Living Supramolecular Polymerization Established by Combining Energy Landscapes of Photoisomerization and Nucleation–Elongation Processes. *J. Am. Chem. Soc.* **2016**, *138* (43), 14347-14353.
42. Korevaar, P. A.; George, S. J.; Markvoort, A. J.; Smulders, M. M. J.; Hilbers, P. A. J.; Schenning, A. P. H. J.; De Greef, T. F. A.; Meijer, E. W., Pathway complexity in supramolecular polymerization. *Nature* **2012**, *481* (7382), 492-496.
43. Zhang, W.; Jin, W.; Fukushima, T.; Saeki, A.; Seki, S.; Aida, T., Supramolecular Linear Heterojunction Composed of Graphite-Like Semiconducting Nanotubular Segments. *Science* **2011**, *334* (6054), 340-343.
44. Fukui, T.; Kawai, S.; Fujinuma, S.; Matsushita, Y.; Yasuda, T.; Sakurai, T.; Seki, S.; Takeuchi, M.; Sugiyasu, K., Control over differentiation of a metastable supramolecular assembly in one and two dimensions. *Nat. Chem.* **2016**.

45. Ogi, S.; Sugiyasu, K.; Manna, S.; Samitsu, S.; Takeuchi, M., Living supramolecular polymerization realized through a biomimetic approach. *Nat Chem* **2014**, *6* (3), 188-195.
46. Ogi, S.; Stepanenko, V.; Sugiyasu, K.; Takeuchi, M.; Würthner, F., Mechanism of self-assembly process and seeded supramolecular polymerization of perylene bisimide organogelator. *J. Am. Chem. Soc.* **2015**, *137* (9), 3300-3307.
47. Kang, J.; Miyajima, D.; Mori, T.; Inoue, Y.; Itoh, Y.; Aida, T., A rational strategy for the realization of chain-growth supramolecular polymerization. *Science* **2015**, *347* (6222), 646-651.
48. Weingarten, A. S.; Kazantsev, R. V.; Palmer, L. C.; McClendon, M.; Koltonow, A. R.; Samuel Amanda, P. S.; Kiebala, D. J.; Wasielewski, M. R.; Stupp, S. I., Self-Assembling Hydrogel Scaffolds for Photocatalytic Hydrogen Production. *Nat Chem* **2014**, *6* (11), 964-970.
49. Shahar, C.; Baram, J.; Tidhar, Y.; Weissman, H.; Cohen, S. R.; Pinkas, I.; Rybtchinski, B., Self-Assembly of Light-Harvesting Crystalline Nanosheets in Aqueous Media. *ACS Nano* **2013**, *7* (4), 3547-3556.
50. Nam, K. T.; Shelby, S. A.; Choi, P. H.; Marciel, A. B.; Chen, R.; Tan, L.; Chu, T. K.; Mesch, R. A.; Lee, B.-C.; Connolly, M. D., Free-floating ultrathin two-dimensional crystals from sequence-specific peptoid polymers. *Nat. Mater.* **2010**, *9* (5), 454-460.
51. Lohr, A.; Lysetska, M.; Würthner, F., Supramolecular Stereomutation in Kinetic and Thermodynamic Self-Assembly of Helical Merocyanine Dye Nanorods. *Angew. Chem. Int. Ed.* **2005**, *44* (32), 5071-5074.
52. Kazantsev, R. V.; Dannenhoffer, A. J.; Weingarten, A. S.; Phelan, B. T.; Harutyunyan, B.; Aytun, T.; Narayanan, A.; Fairfield, D. J.; Boekhoven, J.; Sai, H.; Senesi, A.; O'Dogherty, P. I.; Palmer, L. C.; Bedzyk, M. J.; Wasielewski, M. R.; Stupp, S. I., Crystal-Phase Transitions and Photocatalysis in Supramolecular Scaffolds. *J. Am. Chem. Soc.* **2017**, *139* (17), 6120-6127.

53. Kibsgaard, J.; Jaramillo, T. F.; Besenbacher, F., Building an appropriate active-site motif into a hydrogen-evolution catalyst with thiomolybdate [Mo₃S₁₃]²⁻ clusters. *Nat Chem* **2014**, *6* (3), 248-253.
54. Grätzel, M., *Nature* **2001**, *414*, 338.
55. McEvoy, A. J.; Grätzel, M., *Sol. Energy Mater. Sol. Cells* **1994**, *32*, 221.
56. Gerischer, H.; Tributsch, H., *Ber. Bunsen-Ges. Phys. Chem.* **1968**, *72*, 437.
57. Gerischer, H.; Michel-Beyerle, M. E.; Rebentrost, F.; Tributsch, H., *Electrochim. Acta* **1968**, *13*, 1509.
58. Hasselman, G. M.; Watson, D. F.; Stromberg, J. R.; Bocian, D. F.; Holten, D.; Lindsey, J. S.; Meyer, G. J., *J. Phys. Chem. B* **2006**, *110*, 25430.
59. Matsumura, M.; Nomura, Y.; Tsubomura, H., *Bull. Chem. Soc. Jpn.* **1977**, *50*, 2533.
60. Alonso, N.; Beley, M.; Chartier, P.; Ern, V., *Rev. Phys. Appl.* **1981**, *16*, 5.
61. Oregan, B.; Gratzel, M., A Low-Cost, High-Efficiency Solar-Cell Based on Dye-Sensitized Colloidal TiO₂ Films. *Nature* **1991**, *353* (6346), 737-740.
62. Mathew, S.; Yella, A.; Gao, P.; Humphry-Baker, R.; CurchodBasile, F. E.; Ashari-Astani, N.; Tavernelli, I.; Rothlisberger, U.; NazeeruddinMd, K.; Grätzel, M., Dye-sensitized solar cells with 13% efficiency achieved through the molecular engineering of porphyrin sensitizers. *Nat Chem* **2014**, *6* (3), 242-247.
63. Hagfeldt, A.; Boschloo, G.; Sun, L. C.; Kloo, L.; Pettersson, H., Dye-Sensitized Solar Cells. *Chem Rev* **2010**, *110* (11), 6595-6663.
64. Jiao, Y.; Zhang, F.; Gratzel, M.; Meng, S., Structure-Property Relations in All-Organic Dye-Sensitized Solar Cells. *Adv Funct Mater* **2013**, *23* (4), 424-429.

65. Kozma, E.; Concina, I.; Braga, A.; Borgese, L.; Depero, L. E.; Vomiero, A.; Sberveglieri, G.; Catellani, M., Metal-free organic sensitizers with a sterically hindered thiophene unit for efficient dye-sensitized solar cells. *J Mater Chem* **2011**, *21* (36), 13785-13788.
66. Kim, D.; Ghicov, A.; Albu, S. P.; Schmuki, P., Bamboo-Type TiO₂ Nanotubes: Improved Conversion Efficiency in Dye-Sensitized Solar Cells. *J Am Chem Soc* **2008**, *130* (49), 16454-+.
67. Sauvage, F.; Di Fonzo, F.; Bassi, A. L.; Casari, C. S.; Russo, V.; Divitini, G.; Ducati, C.; Bottani, C. E.; Comte, P.; Graetzel, M., Hierarchical TiO₂ Photoanode for Dye-Sensitized Solar Cells. *Nano Lett* **2010**, *10* (7), 2562-2567.
68. Hagfeldt, A.; Boschloo, G.; Sun, L.; Kloo, L.; Pettersson, H., Dye-sensitized solar cells. *Chem. Rev.* **2010**, *110* (11), 6595-6663.
69. Haid, S.; Marszalek, M.; Mishra, A.; Wielopolski, M.; Teuscher, J.; Moser, J. E.; Humphry-Baker, R.; Zakeeruddin, S. M.; Gratzel, M.; Bauerle, P., Significant Improvement of Dye-Sensitized Solar Cell Performance by Small Structural Modification in pi-Conjugated Donor-Acceptor Dyes. *Adv Funct Mater* **2012**, *22* (6), 1291-1302.
70. Joly, D.; Pellejà, L.; Narbey, S.; Oswald, F.; Chiron, J.; Clifford, J. N.; Palomares, E.; Demadrille, R., A Robust Organic Dye for Dye Sensitized Solar Cells Based on Iodine/Iodide Electrolytes Combining High Efficiency and Outstanding Stability. *Sci. Rep.* **2014**, *4*.
71. Kim, B.-G.; Chung, K.; Kim, J., Molecular Design Principle of All-organic Dyes for Dye-Sensitized Solar Cells. *Chemistry – A European Journal* **2013**, *19* (17), 5220-5230.
72. Teng, C.; Yang, X. C.; Yang, C.; Li, S. F.; Cheng, M.; Hagfeldt, A.; Sun, L. C., Molecular Design of Anthracene-Bridged Metal-Free Organic Dyes for Efficient Dye-Sensitized Solar Cells. *J Phys Chem C* **2010**, *114* (19), 9101-9110.

73. Chen, H. J.; Huang, H.; Huang, X. W.; Cliford, J. N.; Forneli, A.; Palomares, E.; Zheng, X. Y.; Zheng, L. P.; Wang, X. Y.; Shen, P.; Zhao, B.; Tan, S. T., High Molar Extinction Coefficient Branchlike Organic Dyes Containing Di(p-tolyl)phenylamine Donor for Dye-Sensitized Solar Cells Applications. *J Phys Chem C* **2010**, *114* (7), 3280-3286.
74. Choi, H.; Raabe, I.; Kim, D.; Teocoli, F.; Kim, C.; Song, K.; Yum, J. H.; Ko, J.; Nazeeruddin, M. K.; Gratzel, M., High Molar Extinction Coefficient Organic Sensitizers for Efficient Dye-Sensitized Solar Cells. *Chem-Eur J* **2010**, *16* (4), 1193-1201.
75. Hagberg, D. P.; Marinado, T.; Karlsson, K. M.; Nonomura, K.; Qin, P.; Boschloo, G.; Brinck, T.; Hagfeldt, A.; Sun, L., Tuning the HOMO and LUMO energy levels of organic chromophores for dye sensitized solar cells. *J Org Chem* **2007**, *72* (25), 9550-9556.
76. Numata, Y.; Ashraful, I.; Shirai, Y.; Han, L., Preparation of donor-acceptor type organic dyes bearing various electron-withdrawing groups for dye-sensitized solar cell application. *Chem. Commun.* **2011**, *47* (21), 6159-6161.
77. Joly, D.; Pellejà, L.; Narbey, S.; Oswald, F.; Chiron, J.; Clifford, J. N.; Palomares, E.; Demadrille, R., A Robust Organic Dye for Dye Sensitized Solar Cells Based on Iodine/Iodide Electrolytes Combining High Efficiency and Outstanding Stability. *Sci. Rep.* **2014**, *4*, 4033.
78. Chen, H.; Huang, H.; Huang, X.; Clifford, J. N.; Forneli, A.; Palomares, E.; Zheng, X.; Zheng, L.; Wang, X.; Shen, P.; Zhao, B.; Tan, S., High Molar Extinction Coefficient Branchlike Organic Dyes Containing Di(p-tolyl)phenylamine Donor for Dye-Sensitized Solar Cells Applications. *J. Phys. Chem. C* **2010**, *114* (7), 3280-3286.
79. Choi, H.; Raabe, I.; Kim, D.; Teocoli, F.; Kim, C.; Song, K.; Yum, J.-H.; Ko, J.; Nazeeruddin, M. K.; Grätzel, M., High Molar Extinction Coefficient Organic Sensitizers for Efficient Dye-Sensitized Solar Cells. *Chem. Eur. J.* **2010**, *16* (4), 1193-1201.

80. Hagberg, D. P.; Marinado, T.; Karlsson, K. M.; Nonomura, K.; Qin, P.; Boschloo, G.; Brinck, T.; Hagfeldt, A.; Sun, L., Tuning the HOMO and LUMO Energy Levels of Organic Chromophores for Dye Sensitized Solar Cells. *J. Org. Chem.* **2007**, *72* (25), 9550-9556.
81. Haid, S.; Marszalek, M.; Mishra, A.; Wielopolski, M.; Teuscher, J.; Moser, J.-E.; Humphry-Baker, R.; Zakeeruddin, S. M.; Grätzel, M.; Bäuerle, P., Significant Improvement of Dye-Sensitized Solar Cell Performance by Small Structural Modification in π -Conjugated Donor–Acceptor Dyes. *Adv. Funct. Mater.* **2012**, *22* (6), 1291-1302.
82. Teng, C.; Yang, X.; Yang, C.; Li, S.; Cheng, M.; Hagfeldt, A.; Sun, L., Molecular Design of Anthracene-Bridged Metal-Free Organic Dyes for Efficient Dye-Sensitized Solar Cells. *J. Phys. Chem. C* **2010**, *114* (19), 9101-9110.
83. Zhou, N. J.; Prabakaran, K.; Lee, B.; Chang, S. H.; Harutyunyan, B.; Guo, P. J.; Butler, M. R.; Timalsina, A.; Bedzyk, M. J.; Ratner, M. A.; Vegiraju, S.; Yau, S.; Wu, C. G.; Chang, R. P. H.; Facchetti, A.; Chen, M. C.; Marks, T. J., Metal-Free Tetrathienoacene Sensitizers for High-Performance Dye-Sensitized Solar Cells. *J. Am. Chem. Soc.* **2015**, *137* (13), 4414-4423.
84. Youn, J.; Huang, P.-Y.; Huang, Y.-W.; Chen, M.-C.; Lin, Y.-J.; Huang, H.; Ortiz, R. P.; Stern, C.; Chung, M.-C.; Feng, C.-Y.; Chen, L.-H.; Facchetti, A.; Marks, T. J., Versatile α,ω -Disubstituted Tetrathienoacene Semiconductors for High Performance Organic Thin-Film Transistors. *Adv. Funct. Mater.* **2012**, *22* (1), 48-60.
85. Kim, C.; Chen, M.-C.; Chiang, Y.-J.; Guo, Y.-J.; Youn, J.; Huang, H.; Liang, Y.-J.; Lin, Y.-J.; Huang, Y.-W.; Hu, T.-S.; Lee, G.-H.; Facchetti, A.; Marks, T. J., Functionalized dithieno[2,3-b:3',2'-d]thiophenes (DTTs) for organic thin-film transistors. *Organic Electronics* **2010**, *11* (5), 801-813.
86. Nazeeruddin, M. K.; Kay, A.; Rodicio, I.; Humphrybaker, R.; Muller, E.; Liska, P.; Vlachopoulos, N.; Gratzel, M., Conversion of Light to Electricity by Cis-X₂bis(2,2'-Bipyridyl-4,4'-Dicarboxylate)Ruthenium(II)

Charge-Transfer Sensitizers (X = Cl-, Br-, I-, Cn-, and Scn-) on Nanocrystalline TiO₂ Electrodes. *J Am Chem Soc* **1993**, *115* (14), 6382-6390.

87. Xie, Q.; Jiang, Y.-L.; Detavernier, C.; Deduytsche, D.; Meirhaeghe, R. L.; Ru, G.-P.; Li, B.-Z.; Qu, X.-P., Atomic layer deposition of TiO₂ from tetrakis-dimethyl-amido titanium or Ti isopropoxide precursors and H₂O. *J. Appl. Phys.* **2007**, *102* (8), 83521.
88. Nelson, A., Co-refinement of multiple-contrast neutron/X-ray reflectivity data using MOTOFIT. *Journal of Applied Crystallography* **2006**, *39* (2), 273-276.
89. Griffith, M. J.; James, M.; Tiani, G.; Wagner, P.; Wallace, G. G.; Officer, D. L., Determining the Orientation and Molecular Packing of Organic Dyes on a TiO₂ Surface Using X-ray Reflectometry. *Langmuir* **2011**, *27* (21), 12944-12950.
90. Ezhumalai, Y.; Lee, B.; Fan, M. S.; Harutyunyan, B.; Prabakaran, K.; Lee, C. P.; Chang, S. H.; Ni, J. S.; Vegiraju, S.; Priyanka, P.; Wu, Y. W.; Liu, C. W.; Yau, S. L.; Lin, J. T.; Wu, C. G.; Bedzyk, M. J.; Chang, R. P. H.; Chen, M. C.; Ho, K. C.; Marks, T. J., Metal-free branched alkyl tetrathienoacene (TTAR)-based sensitizers for high-performance dye-sensitized solar cells. *Journal of Materials Chemistry A* **2017**, *5* (24), 12310-12321.
91. Ezhumalai, Y.; Lee, B.; Fan, M.-S.; Harutyunyan, B.; Prabakaran, K.; Lee, C.-P.; Chang, S. H.; Ni, J.-S.; Vegiraju, S.; Priyanka, P.; Wu, Y.-W.; Liu, C.-W.; Yau, S.-L.; Lin, J. T.; Wu, C.-G.; Bedzyk, M. J.; Chen, M.-C. M.; Ho, K.-C.; Chang, R.; Marks, T., New Branched Alkyl Tetrathienothiophene (TTAR)-Based Organic Sensitizers with Power Conversion Efficiency up to 11%. *Journal of Materials Chemistry A* **2017**.
92. Yum, J.-H.; Holcombe, T. W.; Kim, Y.; Rakstys, K.; Moehl, T.; Teuscher, J.; Delcamp, J. H.; Nazeeruddin, M. K.; Grätzel, M., Blue-Coloured Highly Efficient Dye-Sensitized Solar Cells by Implementing the Diketopyrrolopyrrole Chromophore. *Sci. Rep.* **2013**, *3*.

93. Vos, W. L.; Sprik, R.; van Blaaderen, A.; Imhof, A.; Lagendijk, A.; Wegdam, G. H., Strong effects of photonic band structures on the diffraction of colloidal crystals. *Physical Review B* **1996**, *53* (Copyright (C) 2010 The American Physical Society), 16231.
94. Lee, B.; Hwang, D.-K.; Guo, P.; Ho, S.-T.; Buchholtz, D. B.; Wang, C.-Y.; Chang, R. P. H., Materials, Interfaces, and Photon Confinement in Dye-Sensitized Solar Cells. *The Journal of Physical Chemistry B* **2010**, *114* (45), 14582-14591.
95. Lee, B.; Guo, P.; Li, S.-Q.; Buchholz, D. B.; Chang, R. P. H., Three Dimensional Indium–Tin–Oxide Nanorod Array for Charge Collection in Dye-Sensitized Solar Cells. *ACS Applied Materials & Interfaces* **2014**, *6* (20), 17713-17722.
96. Parratt, L. G., *Physical Review* **1954**, *95* (2), 359-369.
97. Yaffe, O.; Chernikov, A.; Norman, Z. M.; Zhong, Y.; Velauthapillai, A.; van der Zande, A.; Owen, J. S.; Heinz, T. F., Excitons in ultrathin organic-inorganic perovskite crystals. *Phys. Rev. B* **2015**, *92* (4).
98. Wang, G.; Li, D.; Cheng, H. C.; Li, Y.; Chen, C. Y.; Yin, A.; Zhao, Z.; Lin, Z.; Wu, H.; He, Q.; Ding, M.; Liu, Y.; Huang, Y.; Duan, X., Wafer-scale growth of large arrays of perovskite microplate crystals for functional electronics and optoelectronics. *Science Advances* **2015**, *1* (9), e1500613-e1500613.
99. de Quilettes, D. W.; Vorpahl, S. M.; Stranks, S. D.; Nagaoka, H.; Eperon, G. E.; Ziffer, M. E.; Snaith, H. J.; Ginger, D. S., Impact of microstructure on local carrier lifetime in perovskite solar cells. *Science* **2015**, *348* (6235), 683-686.
100. Yin, W.-J.; Shi, T.; Yan, Y., Unique Properties of Halide Perovskites as Possible Origins of the Superior Solar Cell Performance. *Adv. Mater.* **2014**, *26* (27), 4653-4658.
101. Stranks, S. D.; Eperon, G. E.; Grancini, G.; Menelaou, C.; Alcocer, M. J. P.; Leijtens, T.; Herz, L. M.; Petrozza, A.; Snaith, H. J., Electron-Hole Diffusion Lengths Exceeding 1 Micrometer in an Organometal Trihalide Perovskite Absorber. *Science* **2013**, *342* (6156), 341-344.

102. Saliba, M.; Orlandi, S.; Matsui, T.; Aghazada, S.; Cavazzini, M.; Correa-Baena, J.-P.; Gao, P.; Scopelliti, R.; Mosconi, E.; Dahmen, K.-H.; De Angelis, F.; Abate, A.; Hagfeldt, A.; Pozzi, G.; Graetzel, M.; Nazeeruddin, M. K., A molecularly engineered hole-transporting material for efficient perovskite solar cells. *Nature Energy* **2016**, *1* (2), 15017.
103. Yang, W. S.; Noh, J. H.; Jeon, N. J.; Kim, Y. C.; Ryu, S.; Seo, J.; Seok, S. I., High-performance photovoltaic perovskite layers fabricated through intramolecular exchange. *Science* **2015**, *348* (6240), 1234-1237.
104. Shockley, W.; Queisser, H. J., Detailed Balance Limit of Efficiency of p-n Junction Solar Cells. *J. Appl. Phys.* **1961**, *32* (3), 510-519.
105. You, J.; Meng, L.; Song, T.-B.; Guo, T.-F.; Yang, Y.; Chang, W.-H.; Hong, Z.; Chen, H.; Zhou, H.; Chen, Q.; Liu, Y.; De Marco, N.; Yang, Y., Improved air stability of perovskite solar cells via solution-processed metal oxide transport layers. *Nature Nanotechnology* **2015**, *11* (1), 75-81.
106. Li, X.; Ibrahim Dar, M.; Yi, C.; Luo, J.; Tschumi, M.; Zakeeruddin, S. M.; Nazeeruddin, M. K.; Han, H.; Grätzel, M., Improved performance and stability of perovskite solar cells by crystal crosslinking with alkylphosphonic acid ω -ammonium chlorides. *Nat. Chem.* **2015**, *7* (9), 703-711.
107. Kaltenbrunner, M.; Adam, G.; Glowacki, E. D.; Drack, M.; Schwödauer, R.; Leonat, L.; Apaydin, D. H.; Groiss, H.; Scharber, M. C.; White, M. S.; Sariciftci, N. S.; Bauer, S., Flexible high power-per-weight perovskite solar cells with chromium oxide–metal contacts for improved stability in air. *Nat. Mat.* **2015**, *14* (10), 1032-1039.
108. Han, Y.; Meyer, S.; Dkhissi, Y.; Weber, K.; Pringle, J. M.; Bach, U.; Spiccia, L.; Cheng, Y.-B., Degradation observations of encapsulated planar CH₃NH₃PbI₃ perovskite solar cells at high temperatures and humidity. *Journal of Materials Chemistry A* **2015**, *3* (15), 8139-8147.

109. Smith, I. C.; Hoke, E. T.; Solis-Ibarra, D.; McGehee, M. D.; Karunadasa, H. I., A Layered Hybrid Perovskite Solar-Cell Absorber with Enhanced Moisture Stability. *Angew. Chem. Int. Ed.* **2014**, *53* (42), 11232-11235.
110. Noh, J. H.; Im, S. H.; Heo, J. H.; Mandal, T. N.; Seok, S. I., Chemical Management for Colorful, Efficient, and Stable Inorganic–Organic Hybrid Nanostructured Solar Cells. *Nano Lett.* **2013**, *13* (4), 1764-1769.
111. Leijtens, T.; Eperon, G. E.; Pathak, S.; Abate, A.; Lee, M. M.; Snaith, H. J., Overcoming ultraviolet light instability of sensitized TiO₂ with meso-superstructured organometal tri-halide perovskite solar cells. *Nature Communications* **2013**, *4*.
112. Cao, D. H.; Stoumpos, C. C.; Farha, O. K.; Hupp, J. T.; Kanatzidis, M. G., 2D Homologous Perovskites as Light-Absorbing Materials for Solar Cell Applications. *J. Am. Chem. Soc.* **2015**, *137* (24), 7843-7850.
113. Kagan, C. R., Organic-Inorganic Hybrid Materials as Semiconducting Channels in Thin-Film Field-Effect Transistors. *Science* **1999**, *286* (5441), 945-947.
114. Tsai, H. H.; Nie, W. Y.; Blancon, J. C.; Toumpas, C. C. S.; Asadpour, R.; Harutyunyan, B.; Neukirch, A. J.; Verduzco, R.; Crochet, J. J.; Tretiak, S.; Pedesseau, L.; Even, J.; Alam, M. A.; Gupta, G.; Lou, J.; Ajayan, P. M.; Bedzyk, M. J.; Kanatzidis, M. G.; Mohite, A. D., High-efficiency two-dimensional Ruddlesden-Popper perovskite solar cells. *Nature* **2016**, *536* (7616), 312-+.
115. Nie, W.; Tsai, H.; Asadpour, R.; Blancon, J. C.; Neukirch, A. J.; Gupta, G.; Crochet, J. J.; Chhowalla, M.; Tretiak, S.; Alam, M. A.; Wang, H. L.; Mohite, A. D., High-efficiency solution-processed perovskite solar cells with millimeter-scale grains. *Science* **2015**, *347* (6221), 522-525.
116. Tsai, H.; Nie, W.; Cheruku, P.; Mack, N. H.; Xu, P.; Gupta, G.; Mohite, A. D.; Wang, H.-L., Optimizing composition and morphology for large-grain perovskite solar cells via chemical control. *Chem. Mater.* **2015**, *27* (16), 5570-5576.

117. Kazim, S.; Nazeeruddin, M. K.; Grätzel, M.; Ahmad, S., Perovskite as Light Harvester: A Game Changer in Photovoltaics. *Angewandte Chemie International Edition* **2014**, *53* (11), 2812-2824.
118. Park, N.-G., Organometal Perovskite Light Absorbers Toward a 20% Efficiency Low-Cost Solid-State Mesoscopic Solar Cell. *The Journal of Physical Chemistry Letters* **2013**, *4* (15), 2423-2429.
119. Green, M. A.; Ho-Baillie, A.; Snaith, H. J., The emergence of perovskite solar cells. *Nat Photon* **2014**, *8* (7), 506-514.
120. Stoumpos, C. C.; Kanatzidis, M. G., The Renaissance of Halide Perovskites and Their Evolution as Emerging Semiconductors. *Acc Chem Res* **2015**, *48* (10), 2791-802.
121. Sum, T. C.; Mathews, N., Advancements in perovskite solar cells: photophysics behind the photovoltaics. *Energy & Environmental Science* **2014**, *7* (8), 2518-2534.
122. Xing, G.; Mathews, N.; Sun, S.; Lim, S. S.; Lam, Y. M.; Grätzel, M.; Mhaisalkar, S.; Sum, T. C., Long-Range Balanced Electron- and Hole-Transport Lengths in Organic-Inorganic CH₃NH₃PbI₃. *Science* **2013**, *342* (6156), 344-347.
123. Stranks, S. D.; Eperon, G. E.; Grancini, G.; Menelaou, C.; Alcocer, M. J.; Leijtens, T.; Herz, L. M.; Petrozza, A.; Snaith, H. J., Electron-hole diffusion lengths exceeding 1 micrometer in an organometal trihalide perovskite absorber. *Science* **2013**, *342* (6156), 341-4.
124. Gao, P.; Grätzel, M.; Nazeeruddin, M. K., Organohalide lead perovskites for photovoltaic applications. *Energy & Environmental Science* **2014**, *7* (8), 2448.
125. Kim, H.-S.; Lee, C.-R.; Im, J.-H.; Lee, K.-B.; Moehl, T.; Marchioro, A.; Moon, S.-J.; Humphry-Baker, R.; Yum, J.-H.; Moser, J. E.; Grätzel, M.; Park, N.-G., Lead Iodide Perovskite Sensitized All-Solid-State Submicron Thin Film Mesoscopic Solar Cell with Efficiency Exceeding 9%. *Scientific Reports* **2012**, *2*, 591.

126. Heo, J. H.; Im, S. H.; Noh, J. H.; Mandal, T. N.; Lim, C.-S.; Chang, J. A.; Lee, Y. H.; Kim, H.-j.; Sarkar, A.; NazeeruddinMd, K.; Gratzel, M.; Seok, S. I., Efficient inorganic-organic hybrid heterojunction solar cells containing perovskite compound and polymeric hole conductors. *Nat Photon* **2013**, *7* (6), 486-491.
127. Lee, M. M.; Teuscher, J.; Miyasaka, T.; Murakami, T. N.; Snaith, H. J., Efficient Hybrid Solar Cells Based on Meso-Superstructured Organometal Halide Perovskites. *Science* **2012**, *338* (6107), 643-647.
128. Jung, H. S.; Park, N.-G., Perovskite Solar Cells: From Materials to Devices. *Small* **2015**, *11* (1), 10-25.
129. Lee, Y.; Mitzi, D. B.; Barnes, P. W.; Vogt, T., Pressure-induced phase transitions and templating effect in three-dimensional organic-inorganic hybrid perovskites. *Physical Review B* **2003**, *68* (2), 020103.
130. Chen, Q.; Zhou, H.; Hong, Z.; Luo, S.; Duan, H.-S.; Wang, H.-H.; Liu, Y.; Li, G.; Yang, Y., Planar Heterojunction Perovskite Solar Cells via Vapor-Assisted Solution Process. *Journal of the American Chemical Society* **2014**, *136* (2), 622-625.
131. Hao, F.; Stoumpos, C. C.; Liu, Z.; Chang, R. P.; Kanatzidis, M. G., Controllable perovskite crystallization at a gas-solid interface for hole conductor-free solar cells with steady power conversion efficiency over 10%. *J Am Chem Soc* **2014**, *136* (46), 16411-9.
132. Burschka, J.; Pellet, N.; Moon, S.-J.; Humphry-Baker, R.; Gao, P.; Nazeeruddin, M. K.; Gratzel, M., Sequential deposition as a route to high-performance perovskite-sensitized solar cells. *Nature* **2013**, *499* (7458), 316-319.
133. Liu, M.; Johnston, M. B.; Snaith, H. J., Efficient planar heterojunction perovskite solar cells by vapour deposition. *Nature* **2013**, *501* (7467), 395-398.
134. Nie, W.; Tsai, H.; Asadpour, R.; Blancon, J.-C.; Neukirch, A. J.; Gupta, G.; Crochet, J. J.; Chhowalla, M.; Tretiak, S.; Alam, M. A.; Wang, H.-L.; Mohite, A. D., High-efficiency solution-processed perovskite solar cells with millimeter-scale grains. *Science* **2015**, *347* (6221), 522-525.

135. Docampo, P.; Ball, J. M.; Darwich, M.; Eperon, G. E.; Snaith, H. J., Efficient organometal trihalide perovskite planar-heterojunction solar cells on flexible polymer substrates. *Nat Commun* **2013**, *4*.
136. Jeon, N. J.; Noh, J. H.; Yang, W. S.; Kim, Y. C.; Ryu, S.; Seo, J.; Seok, S. I., Compositional engineering of perovskite materials for high-performance solar cells. *Nature* **2015**, *517* (7535), 476-480.
137. Kim, H.-B.; Choi, H.; Jeong, J.; Kim, S.; Walker, B.; Song, S.; Kim, J. Y., Mixed solvents for the optimization of morphology in solution-processed, inverted-type perovskite/fullerene hybrid solar cells. *Nanoscale* **2014**, *6* (12), 6679-6683.
138. Jeon, N. J.; Noh, J. H.; Kim, Y. C.; Yang, W. S.; Ryu, S.; Seok, S. I., Solvent engineering for high-performance inorganic–organic hybrid perovskite solar cells. *Nat Mater* **2014**, *13* (9), 897-903.
139. Xiao, M.; Huang, F.; Huang, W.; Dkhissi, Y.; Zhu, Y.; Etheridge, J.; Gray-Weale, A.; Bach, U.; Cheng, Y.-B.; Spiccia, L., A Fast Deposition-Crystallization Procedure for Highly Efficient Lead Iodide Perovskite Thin-Film Solar Cells. *Angewandte Chemie* **2014**, *126* (37), 10056-10061.
140. Dualeh, A.; Tétreault, N.; Moehl, T.; Gao, P.; Nazeeruddin, M. K.; Grätzel, M., Effect of Annealing Temperature on Film Morphology of Organic–Inorganic Hybrid Pervoskite Solid-State Solar Cells. *Advanced Functional Materials* **2014**, *24* (21), 3250-3258.
141. Eperon, G. E.; Burlakov, V. M.; Docampo, P.; Goriely, A.; Snaith, H. J., Morphological Control for High Performance, Solution-Processed Planar Heterojunction Perovskite Solar Cells. *Advanced Functional Materials* **2014**, *24* (1), 151-157.
142. Liang, P.-W.; Liao, C.-Y.; Chueh, C.-C.; Zuo, F.; Williams, S. T.; Xin, X.-K.; Lin, J.; Jen, A. K. Y., Additive Enhanced Crystallization of Solution-Processed Perovskite for Highly Efficient Planar-Heterojunction Solar Cells. *Adv. Mater.* **2014**, *26* (22), 3748-3754.
143. Chen, C.-C.; Hong, Z.; Li, G.; Chen, Q.; Zhou, H.; Yang, Y., One-step, low-temperature deposited perovskite solar cell utilizing small molecule additive. *Journal of Photonics for Energy* **2015**, *5* (1), 057405.

144. Zhao, Y.; Zhu, K., CH₃NH₃Cl-Assisted One-Step Solution Growth of CH₃NH₃PbI₃: Structure, Charge-Carrier Dynamics, and Photovoltaic Properties of Perovskite Solar Cells. *The Journal of Physical Chemistry C* **2014**, *118* (18), 9412-9418.
145. Zuo, C.; Ding, L., An 80.11% FF record achieved for perovskite solar cells by using the NH₄Cl additive. *Nanoscale* **2014**, *6* (17), 9935-8.
146. Eperon, G. E.; Stranks, S. D.; Menelaou, C.; Johnston, M. B.; Herz, L. M.; Snaith, H. J., Formamidinium lead trihalide: a broadly tunable perovskite for efficient planar heterojunction solar cells. *Energy & Environmental Science* **2014**, *7* (3), 982.
147. Eperon, G. E.; Paterno, G. M.; Sutton, R. J.; Zampetti, A.; Haghhighirad, A. A.; Cacialli, F.; Snaith, H. J., Inorganic caesium lead iodide perovskite solar cells. *Journal of Materials Chemistry A* **2015**, *3* (39), 19688-19695.
148. Li, G.; Zhang, T.; Zhao, Y., Hydrochloric acid accelerated formation of planar CH₃NH₃PbI₃perovskite with high humidity tolerance. *J. Mater. Chem. A* **2015**, *3* (39), 19674-19678.
149. Soe, C. M. M.; Stoumpos, C. C.; Harutyunyan, B.; Manley, E. F.; Chen, L. X.; Bedzyk, M. J.; Marks, T. J.; Kanatzidis, M. G., Room Temperature Phase Transition in Methylammonium Lead Iodide Perovskite Thin Films Induced by Hydrohalic Acid Additives. *Chemsuschem* **2016**, *9* (18), 2656-2665.
150. Wang, F.; Yu, H.; Xu, H.; Zhao, N., HPbI₃: A New Precursor Compound for Highly Efficient Solution-Processed Perovskite Solar Cells. *Advanced Functional Materials* **2015**, *25* (7), 1120-1126.
151. Onoda-Yamamoto, N.; Yamamoto, O.; Matsuo, T.; Suga, H., p-T phase relations of CH₃NH₃PbX₃ (X = Cl, Br, I) crystals. *Journal of Physics and Chemistry of Solids* **1992**, *53* (2), 277-281.
152. Milot, R. L.; Eperon, G. E.; Snaith, H. J.; Johnston, M. B.; Herz, L. M., Temperature-Dependent Charge-Carrier Dynamics in CH₃NH₃PbI₃Perovskite Thin Films. *Advanced Functional Materials* **2015**, *25* (39), 6218-6227.

153. Stoumpos, C. C.; Malliakas, C. D.; Kanatzidis, M. G., Semiconducting Tin and Lead Iodide Perovskites with Organic Cations: Phase Transitions, High Mobilities, and Near-Infrared Photoluminescent Properties. *Inorganic Chemistry* **2013**, *52* (15), 9019-9038.
154. Poglitsch, A.; Weber, D., Dynamic disorder in methylammoniumtrihalogenoplumbates (II) observed by millimeter-wave spectroscopy. *The Journal of Chemical Physics* **1987**, *87* (11), 6373-6378.
155. Wang, Y.; Lu, X.; Yang, W.; Wen, T.; Yang, L.; Ren, X.; Wang, L.; Lin, Z.; Zhao, Y., Pressure-Induced Phase Transformation, Reversible Amorphization, and Anomalous Visible Light Response in Organolead Bromide Perovskite. *J Am Chem Soc* **2015**, *137* (34), 11144-9.
156. Onoda-Yamamoto, N.; Matsuo, T.; Suga, H., Calorimetric and IR spectroscopic studies of phase transitions in methylammonium trihalogenoplumbates (II)[†]. *Journal of Physics and Chemistry of Solids* **1990**, *51* (12), 1383-1395.
157. Baikie, T.; Fang, Y.; Kadro, J. M.; Schreyer, M.; Wei, F.; Mhaisalkar, S. G.; Graetzel, M.; White, T. J., Synthesis and crystal chemistry of the hybrid perovskite (CH₃NH₃)PbI₃ for solid-state sensitised solar cell applications. *Journal of Materials Chemistry A* **2013**, *1* (18), 5628.
158. Knop, O.; Wasylisen, R. E.; White, M. A.; Cameron, T. S.; Oort, M. J. M. V., Alkylammonium lead halides. Part 2. CH₃NH₃PbX₃ (X = Cl, Br, I) perovskites: cuboctahedral halide cages with isotropic cation reorientation. *Canadian Journal of Chemistry* **1990**, *68* (3), 412-422.
159. Xu, Q.; Eguchi, T.; Nakayama, H.; Nakamura, N.; Kishita, M., Molecular Motions and Phase Transitions in Solid CH₃NH₃PbX₃ (X = Cl, Br, I) as Studied by NMR and NQR. In *Zeitschrift für Naturforschung A*, 1991; Vol. 46, p 240.
160. Walsh, A.; Scanlon, D. O.; Chen, S.; Gong, X. G.; Wei, S. H., Self-regulation mechanism for charged point defects in hybrid halide perovskites. *Angew Chem Int Ed Engl* **2015**, *54* (6), 1791-4.

161. Arlt, G.; Hennings, D.; de With, G., Dielectric properties of fine-grained barium titanate ceramics. *Journal of Applied Physics* **1985**, *58* (4), 1619-1625.
162. Begg, B. D.; Vance, E. R.; Nowotny, J., Effect of Particle Size on the Room-Temperature Crystal Structure of Barium Titanate. *Journal of the American Ceramic Society* **1994**, *77* (12), 3186-3192.
163. Frey, M. H.; Payne, D. A., Grain-size effect on structure and phase transformations for barium titanate. *Physical Review B* **1996**, *54* (5), 3158-3168.
164. Zhao, J.; Li, Y.; Yang, G.; Jiang, K.; Lin, H.; Ade, H.; Ma, W.; Yan, H., Efficient organic solar cells processed from hydrocarbon solvents. *Nat. Energy* **2016**, *1* (2), 15027.
165. Lin, Y.; Zhao, F.; Wu, Y.; Chen, K.; Xia, Y.; Li, G.; Prasad, S. K.; Zhu, J.; Huo, L.; Bin, H.; Zhang, Z. G.; Guo, X.; Zhang, M.; Sun, Y.; Gao, F.; Wei, Z.; Ma, W.; Wang, C.; Hodgkiss, J.; Bo, Z.; Inganás, O.; Li, Y.; Zhan, X., Mapping Polymer Donors toward High-Efficiency Fullerene Free Organic Solar Cells. *Adv. Mater.* **2017**, *29* (3), 1604155.
166. Kippelen, B.; Brédas, J.-L., Organic photovoltaics. *Energy Environ. Sci.* **2009**, *2* (3), 251-261.
167. Huang, Y.; Kramer, E. J.; Heeger, A. J.; Bazan, G. C., Bulk heterojunction solar cells: morphology and performance relationships. *Chem. Rev.* **2014**, *114* (14), 7006-7043.
168. Hu, H.; Jiang, K.; Yang, G.; Liu, J.; Li, Z.; Lin, H.; Liu, Y.; Zhao, J.; Zhang, J.; Huang, F.; Qu, Y.; Ma, W.; Yan, H., Terthiophene-based D-A polymer with an asymmetric arrangement of alkyl chains that enables efficient polymer solar cells. *J. Am. Chem. Soc.* **2015**, *137* (44), 14149-57.
169. Poelking, C.; Tietze, M.; Elschner, C.; Olthof, S.; Hertel, D.; Baumeier, B.; Wurthner, F.; Meerholz, K.; Leo, K.; Andrienko, D., Impact of mesoscale order on open-circuit voltage in organic solar cells. *Nat. Mater.* **2015**, *14* (4), 434-9.

170. Dyer-Smith, C.; Howard, I. A.; Cabanetos, C.; El Labban, A.; Beaujuge, P. M.; Laquai, F., Interplay Between Side Chain Pattern, Polymer Aggregation, and Charge Carrier Dynamics in PBDTTPD:PCBM Bulk-Heterojunction Solar Cells. *Adv. Energy Mater.* **2015**, *5* (9), 1401778.
171. Yao, H.; Ye, L.; Zhang, H.; Li, S.; Zhang, S.; Hou, J., Molecular Design of Benzodithiophene-Based Organic Photovoltaic Materials. *Chem. Rev.* **2016**, *116* (12), 7397-457.
172. Roncali, J., Molecular bulk heterojunctions: an emerging approach to organic solar cells. *Acc. Chem. Res.* **2009**, *42* (11), 1719-30.
173. Walker, B.; Kim, C.; Nguyen, T.-Q., Small Molecule Solution-Processed Bulk Heterojunction Solar Cells†. *Chem. Mater.* **2011**, *23* (3), 470-482.
174. Loser, S.; Miyauchi, H.; Hennek, J.; Smith, J.; Huang, C.; Facchetti, A.; Marks, T., A "zig-zag" naphthodithiophene core for increased efficiency in solution-processed small molecule solar cells. *Chem. Commun.* **2012**, *48* (68), 8511-8513.
175. Yang, L.; Zhang, S.; He, C.; Zhang, J.; Yao, H.; Yang, Y.; Zhang, Y.; Zhao, W.; Hou, J., New Wide Band Gap Donor for Efficient Fullerene-Free All-Small-Molecule Organic Solar Cells. *J. Am. Chem. Soc.* **2017**, *139* (5), 1958-1966.
176. Kawashima, K.; Fukuhara, T.; Suda, Y.; Suzuki, Y.; Koganezawa, T.; Yoshida, H.; Ohkita, H.; Osaka, I.; Takimiya, K., Implication of Fluorine Atom on Electronic Properties, Ordering Structures, and Photovoltaic Performance in Naphthobisthiadiazole-Based Semiconducting Polymers. *J. Am. Chem. Soc.* **2016**, *138* (32), 10265-10275.
177. Chen, Z.; Brown, J.; Drees, M.; Seger, M.; Hu, Y.; Xia, Y.; Boudinet, D.; McCray, M.; Delferro, M.; Marks, T. J.; Liao, C.-Y.; Ko, C.-W.; Chang, Y.-M.; Facchetti, A., Benzo[d][1,2,3]thiadiazole (isoBT): Synthesis, Structural Analysis, and Implementation in Semiconducting Polymers. *Chem. Mater.* **2016**, *28* (17), 6390-6400.

178. Gao, Y.; Deng, Y.; Tian, H.; Zhang, J.; Yan, D.; Geng, Y.; Wang, F., Multifluorination toward High-Mobility Ambipolar and Unipolar n-Type Donor-Acceptor Conjugated Polymers Based on Isoindigo. *Adv. Mater.* **2017**, 1606217.
179. Okamoto, T.; Nakahara, K.; Saeki, A.; Seki, S.; Oh, J. H.; Akkerman, H. B.; Bao, Z.; Matsuo, Y., Aryl-Perfluoroaryl Substituted Tetracene: Induction of Face-to-Face π - π Stacking and Enhancement of Charge Carrier Properties. *Chem. Mater.* **2011**, 23 (7), 1646-1649.
180. Li, W.; Albrecht, S.; Yang, L.; Roland, S.; Tumbleston, J. R.; McAfee, T.; Yan, L.; Kelly, M. A.; Ade, H.; Neher, D.; You, W., Mobility-controlled performance of thick solar cells based on fluorinated copolymers. *J. Am. Chem. Soc.* **2014**, 136 (44), 15566-15576.
181. Zhao, W.; Li, S.; Zhang, S.; Liu, X.; Hou, J., Ternary Polymer Solar Cells based on Two Acceptors and One Donor for Achieving 12.2% Efficiency. *Adv. Mater.* **2016**, 29 (2), 1604059.
182. Mai, J.; Lau, T.-K.; Li, J.; Peng, S.-H.; Hsu, C.-S.; Jeng, U. S.; Zeng, J.; Zhao, N.; Xiao, X.; Lu, X., Understanding Morphology Compatibility for High-Performance Ternary Organic Solar Cells. *Chem. Mater.* **2016**, 28 (17), 6186-6195.
183. Liu, T.; Guo, Y.; Yi, Y.; Huo, L.; Xue, X.; Sun, X.; Fu, H.; Xiong, W.; Meng, D.; Wang, Z.; Liu, F.; Russell, T. P.; Sun, Y., Ternary Organic Solar Cells Based on Two Compatible Nonfullerene Acceptors with Power Conversion Efficiency >10%. *Adv. Mater.* **2016**, 28 (45), 10008-10015.
184. Wang, Y.; Xu, W.-D.; Zhang, J.-D.; Zhou, L.; Lei, G.; Liu, C.-F.; Lai, W.-Y.; Huang, W., A Small Molecule/Fullerene Binary Acceptor System for High-Performance Polymer Solar Cells with Enhanced Light-Harvesting Property and Balanced Carrier Mobility. *J. Mater. Chem. A* **2017**, 5 (6), 2460-2465.
185. Kouijzer, S.; Li, W.; Wienk, M. M.; Janssen, R. A. J., Charge transfer state energy in ternary bulk-heterojunction polymer–fullerene solar cells. *J. Photon. Energy* **2014**, 5 (1), 057203.

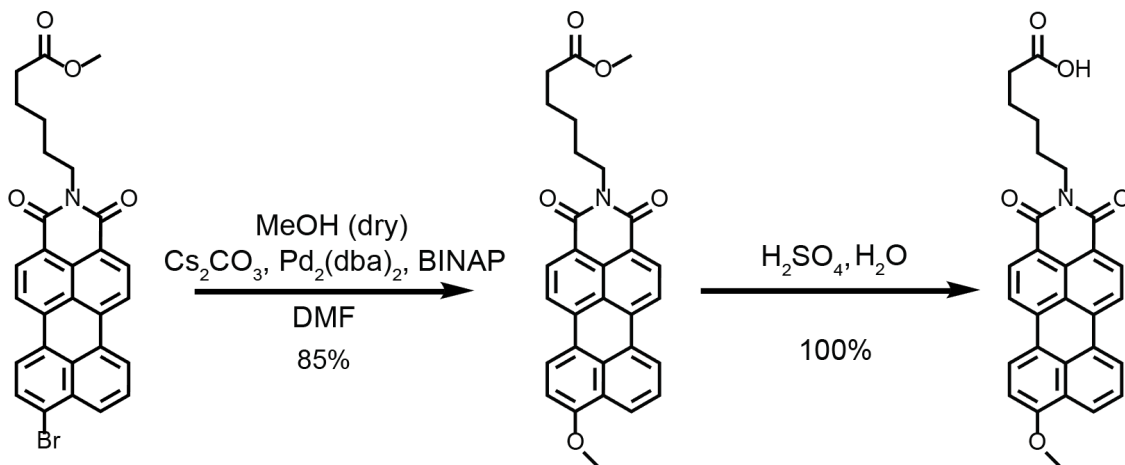
186. Gobalasingham, N. S.; Noh, S.; Howard, J. B.; Thompson, B. C., Influence of Surface Energy on Organic Alloy Formation in Ternary Blend Solar Cells Based on Two Donor Polymers. *ACS Appl. Mater. Interfaces* **2016**, 8 (41), 27931-27941.
187. Zhang, Y.; Deng, D.; Lu, K.; Zhang, J.; Xia, B.; Zhao, Y.; Fang, J.; Wei, Z., Synergistic effect of polymer and small molecules for high-performance ternary organic solar cells. *Adv. Mater.* **2015**, 27 (6), 1071-1076.
188. Ye, L.; Sun, K.; Jiang, W.; Zhang, S.; Zhao, W.; Yao, H.; Wang, Z.; Hou, J., Enhanced Efficiency in Fullerene-Free Polymer Solar Cell by Incorporating Fine-designed Donor and Acceptor Materials. *ACS Appl. Mater. Interfaces* **2015**, 7 (17), 9274-80.
189. Yang, Y.; Chen, W.; Dou, L.; Chang, W.-H.; Duan, H.-S.; Bob, B.; Li, G.; Yang, Y., High-performance multiple-donor bulk heterojunction solar cells. *Nat. Photon.* **2015**, 9 (3), 190-198.
190. Savoie, B. M.; Dunaisky, S.; Marks, T. J.; Ratner, M. A., The Scope and Limitations of Ternary Blend Organic Photovoltaics. *Adv. Energy Mater.* **2015**, 5 (3), 1400891.
191. Zhang, J.; Zhang, Y.; Fang, J.; Lu, K.; Wang, Z.; Ma, W.; Wei, Z., Conjugated Polymer-Small Molecule Alloy Leads to High Efficient Ternary Organic Solar Cells. *J. Am. Chem. Soc.* **2015**, 137 (25), 8176-83.
192. Liao, H. C.; Chen, P. H.; Chang, R. P. H.; Su, W. F., Morphological Control Agent in Ternary Blend Bulk Heterojunction Solar Cells. *Polymers* **2014**, 6 (11), 2784-2802.
193. Khlyabich, P. P.; Rudenko, A. E.; Street, R. A.; Thompson, B. C., Influence of polymer compatibility on the open-circuit voltage in ternary blend bulk heterojunction solar cells. *ACS Appl. Mater. Interfaces* **2014**, 6 (13), 9913-9.
194. Zhang, G.; Zhang, K.; Yin, Q.; Jiang, X. F.; Wang, Z.; Xin, J.; Ma, W.; Yan, H.; Huang, F.; Cao, Y., High-Performance Ternary Organic Solar Cell Enabled by a Thick Active Layer Containing a Liquid Crystalline Small Molecule Donor. *J. Am. Chem. Soc.* **2017**, 139 (6), 2387-2395.

195. Lu, L.; Chen, W.; Xu, T.; Yu, L., High-performance ternary blend polymer solar cells involving both energy transfer and hole relay processes. *Nat. Commun.* **2015**, *6*, 7327.
196. Ameri, T.; Khoram, P.; Heumuller, T.; Baran, D.; Machui, F.; Troeger, A.; Sgobba, V.; Guldi, D. M.; Halik, M.; Rathgeber, S.; Scherf, U.; Brabec, C. J., Morphology analysis of near IR sensitized polymer/fullerene organic solar cells by implementing low bandgap heteroanalogue C-/Si-PCPDTBT. *J. Mater. Chem. A* **2014**, *2* (45), 19461-19472.
197. Huang, J.; Zhan, C.; Zhang, X.; Zhao, Y.; Lu, Z.; Jia, H.; Jiang, B.; Ye, J.; Zhang, S.; Tang, A.; Liu, Y.; Pei, Q.; Yao, J., Solution-processed DPP-based small molecule that gives high photovoltaic efficiency with judicious device optimization. *ACS Appl. Mater. Interfaces* **2013**, *5* (6), 2033-9.
198. Li, M.; Ni, W.; Wan, X.; Zhang, Q.; Kan, B.; Chen, Y., Benzo[1,2-*b*:4,5-*b'*]dithiophene (BDT)-based small molecules for solution processed organic solar cells. *J. Mater. Chem. A* **2015**, *3* (9), 4765-4776.
199. Harschneck, T.; Zhou, N.; Manley, E. F.; Lou, S. J.; Yu, X.; Butler, M. R.; Timalsina, A.; Turrisi, R.; Ratner, M. A.; Chen, L. X.; Chang, R. P.; Facchetti, A.; Marks, T. J., Substantial photovoltaic response and morphology tuning in benzo[1,2-*b*:6,5-*b'*]dithiophene (bBDT) molecular donors. *Chem. Commun.* **2014**, *50* (31), 4099-101.
200. Loser, S.; Bruns, C. J.; Miyauchi, H.; Ortiz, R. P.; Facchetti, A.; Stupp, S. I.; Marks, T. J., A naphthodithiophene-diketopyrrolopyrrole donor molecule for efficient solution-processed solar cells. *J. Am. Chem. Soc.* **2011**, *133* (21), 8142-5.
201. Loser, S.; Lou, S. J.; Savoie, B. M.; Bruns, C. J.; Timalsina, A.; Leonardi, M. J.; Smith, J. N.; Harschneck, T.; Turrisi, R.; Zhou, N.; Stern, C. L.; Sarjeant, A.; Facchetti, A.; Chang, R.; Stupp, S.; Ratner, M. A.; Chen, L. X.; Marks, T., Systematic Evaluation of Structure-Property Relationships in Heteroacene - Diketopyrrolopyrrole Molecular Donors for Organic Solar Cells. *J. Mater. Chem. A* **2017**.

202. Eastham, N. D.; Dudnik, A. S.; Harutyunyan, B.; Aldrich, T. J.; Leonardi, M. J.; Manley, E. F.; Butler, M. R.; Harschneck, T.; Ratner, M. A.; Chen, L. X., Enhanced Light Absorption in Fluorinated Ternary Small-Molecule Photovoltaics. *ACS Energy Letters* **2017**, 2 (7), 1690-1697.
203. Aldrich, T. J.; Leonardi, M. J.; Dudnik, A. S.; Eastham, N. D.; Harutyunyan, B.; Fauvell, T. J.; Manley, E. F.; Zhou, N.; Butler, M. R.; Harschneck, T., Enhanced Fill Factor through Chalcogen Side-Chain Manipulation in Small-Molecule Photovoltaics. *ACS Energy Letters* **2017**, 2 (10), 2415-2421.
204. Huang, H.; Yang, L.; Sharma, B., Recent advances in organic ternary solar cells. *J. Mater. Chem. A* **2017**.
205. Street, R. A.; Davies, D.; Khlyabich, P. P.; Burkhart, B.; Thompson, B. C., Origin of the tunable open-circuit voltage in ternary blend bulk heterojunction organic solar cells. *J. Am. Chem. Soc.* **2013**, 135 (3), 986-9.
206. Lumley, T.; Miller, A.; Lumley, M. T., Package 'leaps'. **2015**.

8. Appendix A

8.1. Synthesis of MeO-PMI



Scheme 8.1. Synthesis of 9-methoxy-N-(hexanoic acid) perylene-3,4-dicarboximide.

Buchwald-Hartwig Type coupling (step 1).

A Schlenk flask of appropriate size (125 ml) was filled with 100 mg (0.19 mmols) of 9-bromo-N-(methyl hexanoate)perylene-3,4-dicarboximide, 430 mg (1.32 mmols) Cs_2CO_3 , 10 mg (0.016 mmols) BINAP, and 10 mg (0.011 mmols) $\text{Pd}_2(\text{dba})_3$. The flask was then evacuated for 15 minutes before being filled with nitrogen. 50 ml of DMF (dried on a solvent still with calcium hydride) containing 2 ml methanol (dried using 3 Å molecular sieves) was purged with N_2 for 15 minutes and then cannulated into the Schlenk flask, yielding a red solution. The solution was heated at 90°C overnight until a purple solution was obtained. After cooling the solution was diluted with 200 ml of 1 M HCl, causing the formation of a brown precipitate. The precipitate was filtered with a Buckner funnel and then washed with 500 ml of warm water. The solid was dissolved with 3:1 DCM/MeOH and then dried on a rotary evaporator. The compound was then purified on a silica column using 0.5 volume % MeOH in DCM, and then further purified by recycling gel permeation chromatography. Yield 85%.

¹H NMR (499 MHz, Chloroform-d) δ 8.39 (d, *J* = 4.6 Hz, 1H), 8.38 (d, *J* = 4.8 Hz, 1H), 8.29 (d, *J* = 7.8 Hz, 1H), 8.25 (d, *J* = 8.3 Hz, 1H), 8.19 (d, *J* = 8.4 Hz, 1H), 8.16 (d, *J* = 8.1 Hz, 1H), 8.05 (d, *J* = 8.0 Hz, 1H), 7.54 (d, *J* = 7.5 Hz, 1H), 6.88 (d, *J* = 8.4 Hz, 1H), 4.21 – 4.17 (t, 2H), 4.10 (s, 3H), 2.38 (t, *J* = 7.5 Hz, 2H), 1.78 (d, 4H), 1.51 (q, *J* = 7.8 Hz, 2H).

¹³C NMR (126 MHz, Chloroform-d) δ 174.14, 163.94, 157.81, 137.58, 137.29, 131.45, 131.22, 129.77, 128.69, 128.50, 126.22, 126.13, 125.81, 125.11, 124.95, 124.26, 121.68, 120.41, 119.50, 119.23, 118.48, 105.55, 55.92, 51.49, 40.09, 34.02, 27.76, 26.72, 24.73.

HRMS (ESI-TOF-MS): Expected: 479.17402 Observed: 480.1805

De-esterification (step 2).

Compound 1 (30 mg) was dissolved in 8 ml of H₂SO₄, and 2 ml of water was added dropwise, mixing the solution every 5-10 drops. The reaction proceeded for 3 hours at which point it was quenched by 100 ml of water leading to the formation of a brown precipitate. Subsequently the solid was filtered using a Buckner funnel and washed with 500 ml of warm water. The final compound was collected off the filter paper by dissolving in 3:1 DCM/MeOH (sonication may be required). Yield 100%.

¹H NMR (499 MHz, DMSO-*d*₆) δ 11.98 (s, 1H), 8.67 (d, *J* = 7.2 Hz, 1H), 8.60 (t, *J* = 8.9 Hz, 2H), 8.49 (d, *J* = 8.7 Hz, 1H), 8.39 (m, 2H), 8.25 (d, *J* = 7.9 Hz, 1H), 7.69 (t, *J* = 7.2 Hz, 1H), 7.20 (d, *J* = 7.8 Hz, 1H), 4.10 (s, 3H), 4.04 (t, *J* = 7.8 Hz, 2H), 2.24 (t, *J* = 7.2 Hz, 2H), 1.65 (p, *J* = 8.0 Hz, 2H), 1.57 (p, *J* = 7.4 Hz, 2H), 1.37 (p, *J* = 7.7 Hz, 2H).

¹³C NMR (126 MHz, DMSO-*d*₆) δ 174.90, 163.50, 157.94, 137.33, 131.73, 131.50, 128.80, 127.22, 126.97, 126.11, 125.67, 125.13, 121.45, 120.95, 120.55, 119.86, 119.25, 107.20, 56.73, 41.97, 41.80, 41.63, 41.47, 33.95, 27.74, 26.54, 24.70.

HRMS (ESI-TOF-MS): Expected: 465.15807 Observed: 465.15762

8.2. Synthesis of $\text{Na}_2[\text{Mo}_3\text{S}_{13}] \cdot 5\text{H}_2\text{O}$

The procedure from Kibsgaard et al.⁵³ was modified as follows: To 15.4 ml of ammonium sulfide was added 1.0 g elemental sulfur, the solution was stirred until all sulfur dissolved. In a separate vial, 2 g of $\text{Mo}_7\text{O}_{24} \cdot 4\text{H}_2\text{O}(\text{NH}_4)_6$ was dissolved in 10.2 ml of water. This solution was then added to the sulfur solution resulting in a dark red solution. The flask containing this mixture was then sealed and heated at 95°C for 5 days. Note: make sure the flask is properly sealed, evaporation of water during heating will result in formation of impurities. After 5 days, the dark red crystals were filtered, washed with water and ethanol, and then transferred to a flask of toluene. The toluene was brought to a boil to dissolve away any unreacted sulfur. The crystals were then filtered and washed with an addition 200 ml of fresh toluene and dried under vacuum. The crystals (1.5 grams) were then added to 20 ml of 1% NaOH under nitrogen and allowed to stir for 2 hours yielding a deep red solution. The solution was then poured into a 100 ml of 10% NaCl and left overnight until a red/orange precipitate had formed. The solid was filtered and washed with IPA, ether, and finally dried on a vacuum line. The solid was stored under Ar in a -20°C freezer until use.

8.3. Hydrogen production experiments

MeO-PMI and PMI solutions (100 μL , 8.7 mM) were first gelled with poly(diallyl dimethyl ammonium) chloride (PDDA) (20 μL , 4 wt%) in a 7 ml clear screw cap septum vial (Thermo Scientific product # TS-13028) and allowed to age for two hours. Ascorbic acid solutions (1.7 M) were adjusted to pH 4 using 4 M NaOH (measured using a Fisher Scientific Accumet Research AR50 Dual Channel pH/Ion/Conductivity Meter, calibrated with pH 4.0 and pH 7.0 standard solutions). A fresh solution of $\text{Na}_2[\text{Mo}_3\text{S}_{13}] \cdot 5\text{H}_2\text{O}$

clusters (0.17 mM) was prepared by adding 6 mg of cluster to 45.2 ml of water. 20 μ L of this cluster solution was then added to the gels, along with 860 μ L of 0.85 M ascorbic acid as a source of protons and sacrificial electrons. Vials were sealed with a septum, and wrapped in Parafilm to ensure proper sealing. After purging for 10 minutes with Ar, the samples were illuminated for 18 hours with a Schott DCR III lamp equipped with 150 W EKE bulb (output 400 – 700 nm) and fiber optic goosenecks. Samples were placed approximately 1.5 cm from the fiber optic light source (power output \sim 250 W/cm²). For H₂ identification and quantification, a 300 μ L aliquot was taken from the sample vial (7 mL headspace) and injected onto a gas chromatograph (Shimadzu GC-2014) equipped with a 5 Å molecular sieve column, Ar carrier gas, and a thermal conductivity detector. Eight-point calibration curves for H₂ and N₂ were created using a standard (7% H₂ balanced with N₂) and integrated peak areas were used to determine the H₂ concentration in the sample headspace at STP.

8.4. Peak matching for unit cell parameter deduction

As a criterion of goodness of match between generated and measured peak positions for a particular assignment of indices (shown by subscript *s*), a quantitative descriptor Γ was introduced:

$$\Gamma_s = \sum_{i=1}^n I_i^p B_s(q_i, \Delta q)$$

where I_i is the intensity of the *i*th peak, function B returns 1 if within the radius Δq of q_i there is a peak in the experimental list of peaks, and zero otherwise. $p > 0$ is an a priori constant indicating the weight placed on using smaller peaks: larger p values give greater emphasis to larger peaks.

Since a 2D lattice has 3 unknowns (a , b and γ), 3 prominent peaks, which were not multiples of each other in q , were selected. A list of all possible indices for these peaks are generated and other peak

positions predicted. Matching function Γ_s is computed for each peak assignment triad s and ranked in decreasing order. The first few members give the best possible 2D lattice matching.

8.5. X-Ray Reflectivity and Grazing Incidence X-Ray Scattering

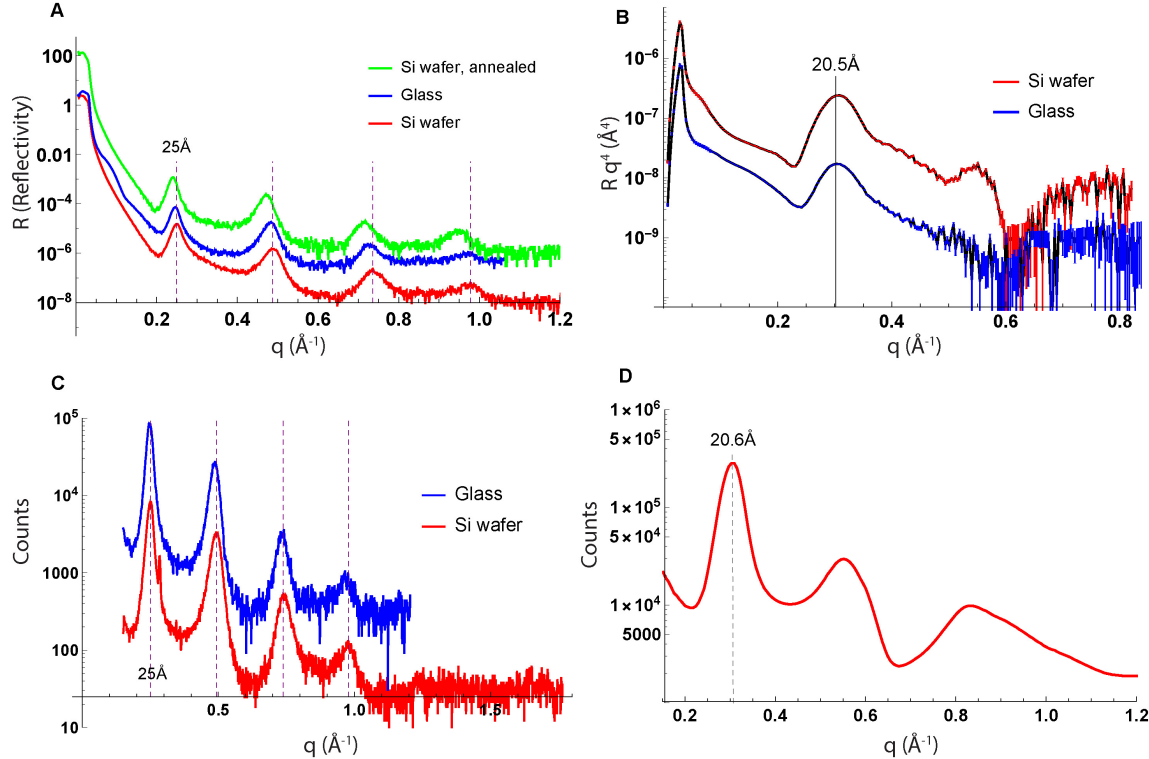


Figure 8.1. **A)** Specular X-ray reflectivity of drop-cast samples on Si wafer and glass. Annealing of the dried sample was performed in a vacuum oven at 40°C for 24 hours. **B)** Normalized specular X-ray reflectivity of spin cast films, **C)** X-ray diffraction pattern of drop-cast samples at a fixed grazing incident angle of 1° for the glass substrate and 2° for the Si wafer. The top curves are vertically offset in **A-C** for purposes of clarity. q is the wavevector transfer. Scattered X-ray counts in **A-C** were collected by a point detector on a Rigaku SmartLab instrument in the NU X-ray Diffraction Facility. **D)** Vertical line-cut in GIWAXS pattern of Figure 3.5A with constraint: $-0.05\text{Å}^{-1} < q_y < 0.05\text{Å}^{-1}$ (here $q = \sqrt{q_x^2 + q_y^2 + q_z^2}$).

8.6. Numerical integration procedure for WAXS intensity

With 2σ precision (which essentially covers the non-vanishing portion of the bell curve) for reciprocal lattice vector \vec{G}_i intensity $I_i(q) = 0$ unless $q > G_i - 2\sigma$.

$$\text{If } G_i - 2\sigma \leq q \leq G_i + 2\sigma \Rightarrow I_i(q) = 2|F_{\parallel}(\vec{G}_i)|^2 \sum_{k=0}^N \sigma e^{-\frac{(q \sin \theta_k - G_i)^2}{2\sigma^2}} \operatorname{sinc}^2\left(q \cos \theta_k \frac{h}{2}\right)$$

where $\theta_k = \arcsin \frac{G_i - 2\sigma}{q} + \frac{k}{N} \left(\frac{\pi}{2} - \arcsin \frac{G_i - 2\sigma}{q} \right)$ and N is the desired number of divisions. ($N = 7$ reproduces the experimental peaks reasonably well.)

$$\text{If } q > G_i + 2\sigma, \text{ same summation as above where } \theta_k = \arcsin \frac{G_i - 2\sigma}{q} + \frac{k}{N} \left(\arcsin \frac{G_i + 2\sigma}{q} - \arcsin \frac{G_i - 2\sigma}{q} \right)$$

Finally, $I(q) = \sum_i I_i(q)$, where summation is over reciprocal lattice vectors.

Geometrically, the integration is over the intersecting arcs of the reciprocal space cylinder and $q = \text{const}$ sphere.

8.7. WAXS peak position shifts and shoulder widths estimation

To estimate the relative importance of parameters in eq. (3.9) and elucidate non-linear behavior of the peak shift and high-q tail, we employ statistical methods, since a direct Taylor series expansion is not reasonable. We define the shoulder widths as below:

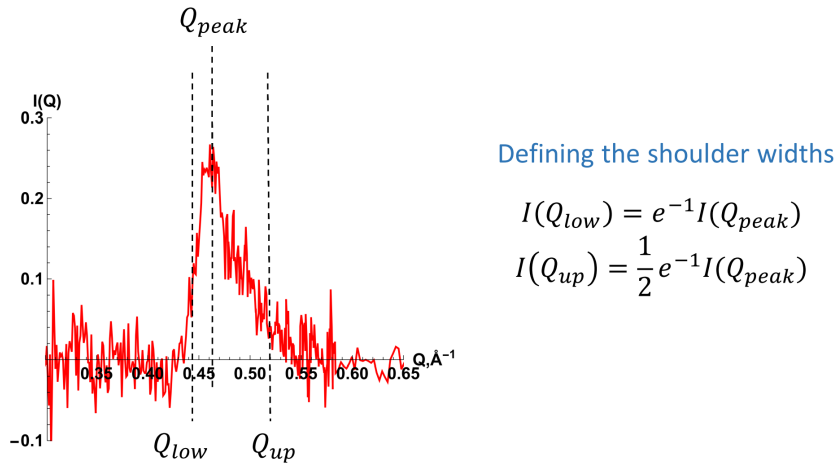
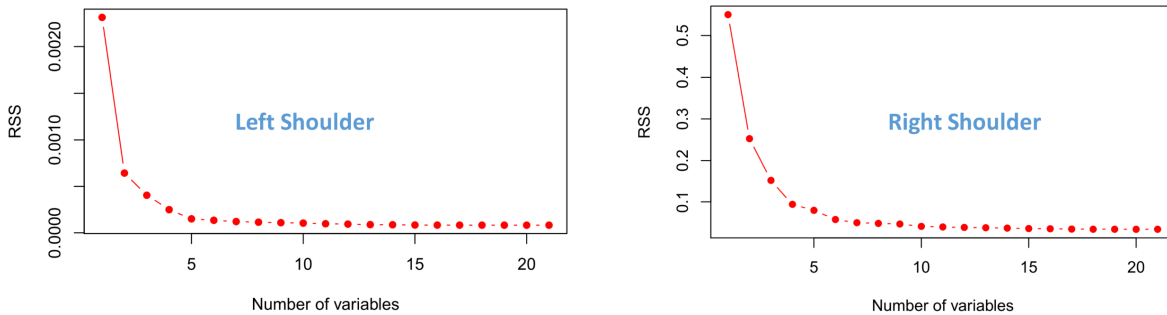


Figure 8.2. Peak asymmetry illustration and shoulder widths definition. $\frac{1}{2}$ for the high- q shoulder is introduced to account for decrease in the form factor along the normal to the sheet.

By using the abovementioned numerical algorithm, we can generate a table of peak positions and shoulder widths as a function of σ, G, h and use statistical methods to find the coefficients of linearized expansion $f(\sigma, G, h) \approx c_i x_i + c_{ij} x_i x_j$, where f stands for either peak position or any of the shoulder widths and c_i for any of σ, G, h variables. A convenient computational tool is the R's *leaps* package²⁰⁶ which allows for an exhaustive search in choosing N variables that minimize the residual sum of squares (RSS). Figure below shows RSS vs number of variables for each case.



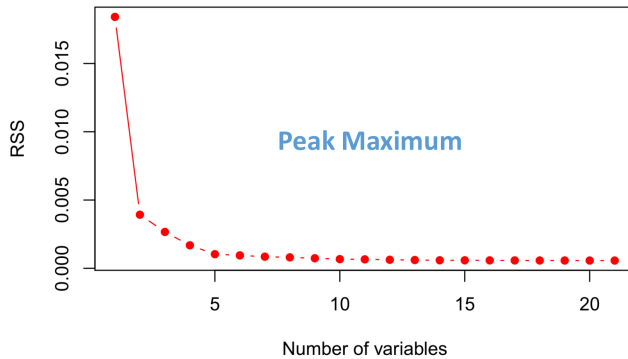


Figure 8.3 RSS as a function of number of variables retained in the model.

By choosing in each case the number of variables right before RSS plateaus, one can write the expansion in terms of standardized variables, hence with each coefficient showing the weight of contribution for the corresponding term:

$$\Delta Q_{peak}^s \approx 2.3 \sigma - 0.24 G h - 0.79 \sigma h - 1.69 h \sigma^2 + 0.97 h^2 \sigma^2$$

$$\Delta Q_{right}^s \approx 2.97 \sigma - 0.12 G - 1.16 \sigma^2 - 3.53 \sigma h + 1.52 \sigma h^2 + 1.01 \sigma^2 h$$

$$\Delta Q_{left}^s \approx 1.2 \sigma - 0.05 \sigma G - 0.13 \sigma h - 0.21 h \sigma^2 + 0.16 \sigma^2 h^2$$

$$\Delta Q_{right} = Q_{up} - Q_{peak}, \Delta Q_{left} = Q_{peak} - Q_{low}, \Delta Q_{peak} = Q_{peak} - G$$

By recasting these equations from standardized to normal variable, we obtain:

$$\Delta Q_{peak} \approx 0.827 \sigma - 0.0532 G h - 0.0215 \sigma h - 0.96 h \sigma^2 + 0.0337 h^2 \sigma^2 + 6.21 \cdot 10^{-4}$$

$$\Delta Q_{right} \approx 6.97 \sigma - 0.0044 G - 54.32 \sigma^2 - 0.624 \sigma h + 0.0157 \sigma h^2 + 3.75 \sigma^2 h + 0.014$$

$$\Delta Q_{left} \approx 1.29 \sigma - 0.03 \sigma G - 0.01 \sigma h + 0.353 h \sigma^2 + 0.016 \sigma^2 h^2 + 2.58 \cdot 10^{-4}$$

8.8. Tilt angle deduction and scattering from tilted chains

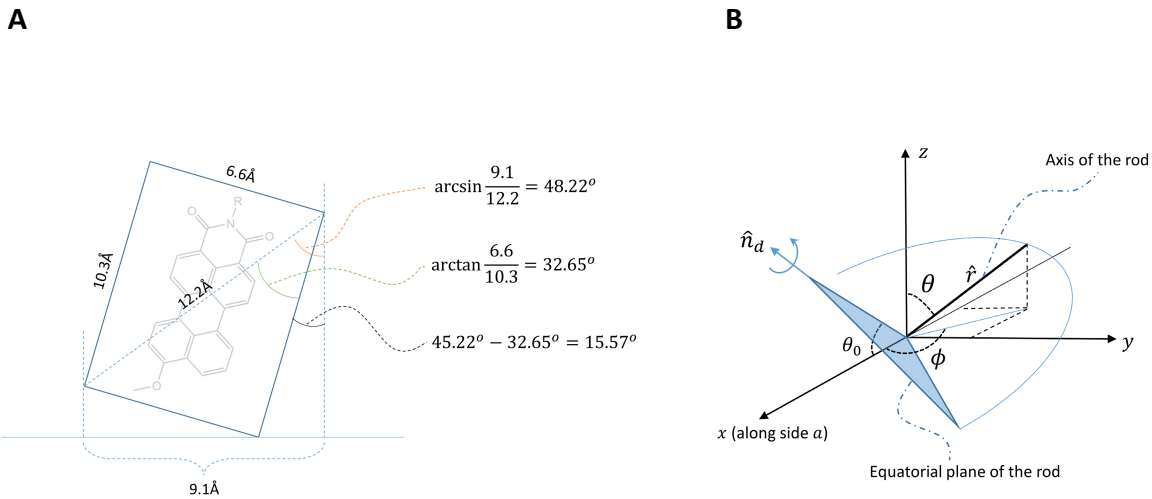


Figure 8.4. **A)** Schematic depiction of the perylene tilt angle, **B)** Geometry of X-ray scattering from a tilted rod (carboxypentyl chain).

Notice, the corners of the slab contain electron rich oxygen atoms hence the choice of the corners as terminating ends of the projection is sounder than height weighted average. The sensitivity of the tilt angle as a function of the chosen slab height is illustrated in the plot below. It indicates that within reasonably chosen slab height only $\approx 1\text{-}2^\circ$ deviation is introduced.

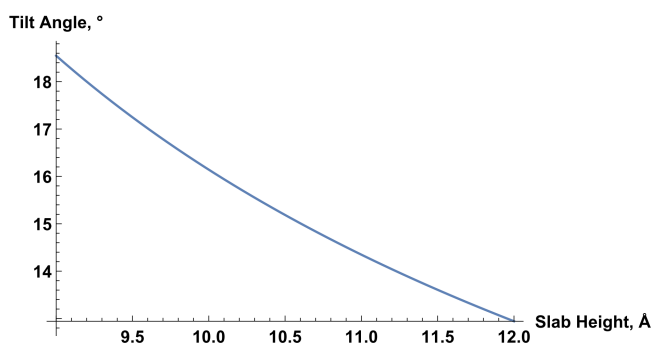


Figure 8.5. Derived tilt angle as a function of chosen slab height.

The narrow rod-like shape of the carboxypentyl chain constrains the X-ray scattering predominantly to the equatorial plane of the rod (i.e. the plane perpendicular to the rod, blue triangle on Figure 8.1b). The observed diffraction spot at $q_r = 0.5 \text{ \AA}^{-1}$, $q_z = 0.45 \text{ \AA}^{-1}$ ($\theta_0 = 42^\circ$) corresponds to scattering along the direction of unit vector \hat{n}_d , which should be an intersection line of the equatorial plane of the rod and the xz plane, to ensure that the maximum of the form factor is oriented along \hat{n}_d . Arbitrary rotation of the thin rod around \hat{n}_d in the plane perpendicular to \hat{n}_d will uphold this condition of maximum scattering. Unit vector \hat{r} along the axis of the rod can be expressed as $\hat{r} = \{\sin \theta \cos \phi, \sin \theta \sin \phi, \cos \theta\}$ and unit vector \hat{n}_d as $\hat{n}_d = \{\cos \theta_0, 0, \sin \theta_0\}$. The maxima condition can be written simply as $\hat{n}_d \cdot \hat{r} = 0$. Hence, the polar angle of the rod is found: $\theta = \arctan\left(-\frac{\tan \theta_0}{\cos \phi}\right)$. The polar angle includes both the natural bend of the chain with respect to perylene plate (Figure 3.4A, $\theta_{nat} \approx 45^\circ$) and the above-deduced tilt angle $\theta_{tilt} = 15.57^\circ$. Therefore, the experimental bend angle can be written as follows:

$$\theta_{nat} = \left| \arctan\left(-\frac{\tan \theta_0}{\cos \phi}\right) \right| - \theta_{tilt}$$

If we idealize the arrangement of chains to be along the bisectors of the basis, the azimuthal angle of the chains can be assumed $\phi \sim 125^\circ$ (or $\phi \sim 55^\circ$), leading to an estimate of natural bend angle from the above formula $\theta_{nat} \sim 42^\circ$, in good agreement with the expected $\theta_{nat} \approx 45^\circ$ value.

8.9. Molecular Orbitals and Partial Charges of the Monomer

Ab initio calculation was performed by DFT (B3LYP) with 6-31G basis.

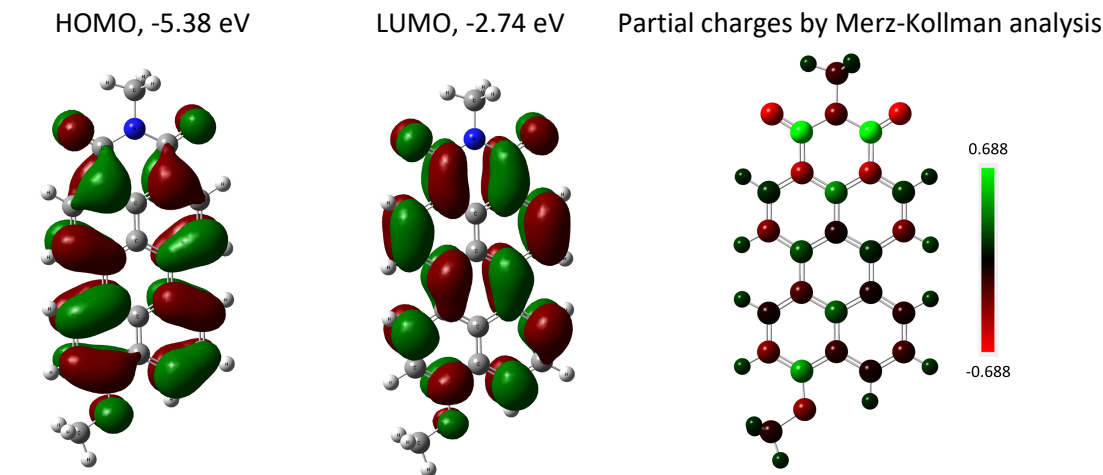


Figure 8.6. HOMO, LUMO and partial charge distribution of MeO-PMI-Me.

Time dependent DFT calculation of the dipole moment of the excited state of MeO-PMI yields a value of 8.2D (ground state has dipole moment of 8.6D), hence Frenkel exciton (FE), formed on the same molecule immediately after absorption of photon, contributes a dipole moment of 0.4D, parallel to the dipole moment of the adjacent molecule. Unsubstituted PMI has dipole moments of 6.7D and 0.4D, for ground state and FE correspondingly.

8.10. UV-vis spectra for various concentrations of MeO-PMI

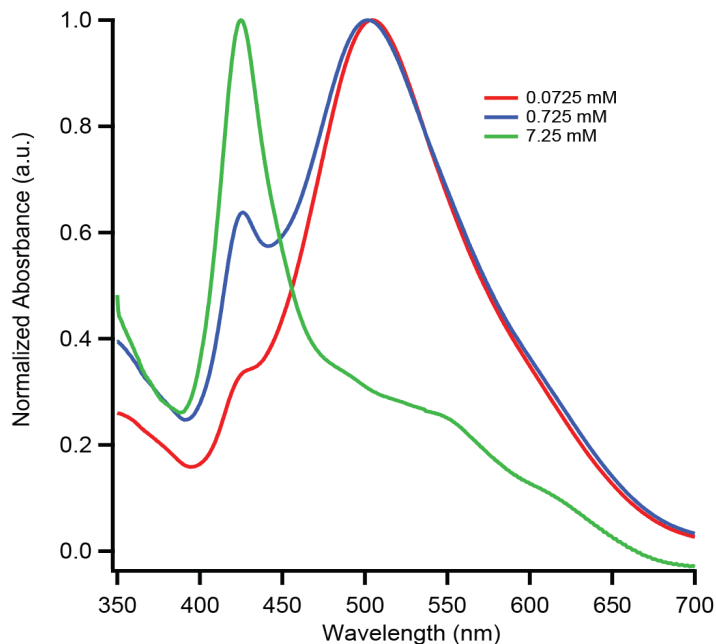


Figure 8.7. UV-Vis absorbance spectra of MeO-PMI at concentrations 0.0725, 0.725 and 7.25 mM in water. Green curve manifests disappearance of monomer peak and formation of nanosheets.

8.11. Cyclic Voltammetry

Cyclic voltammograms (CV) were measured on 5 mM MeO-PMI solutions in DCM, with 0.1M tetrabutylammonium hexafluorophosphate (TBAPF₆, recrystallized twice from ethanol) as supporting electrolyte. Experiments were performed using a three electron setup with a Ag/AgNO₃ (in ACN) reference electrode, platinum wire as the counter electrode, and a platinum disk working electrode. Solutions were purged with Ar for 1 minute before the experiments. The potential was cycled 3 times at 0.1 V/s to insure consistent electrochemical behaviour. All waves were calibrated to the ferrocene/ferrocenium redox couple in order to account for any junction potential. The following potentials were obtained: E_{oxi} = 1.12 V, E_{red1} = -1.12 V, E_{red2} = -1.69 V. Energy level diagram was constructed using the oxidation potential from

CV as the HOMO energy and by adding the band gap the LUMO was found. The HOMO energy agrees well with DFT calculations, however the DFT overestimates the LUMO energy.

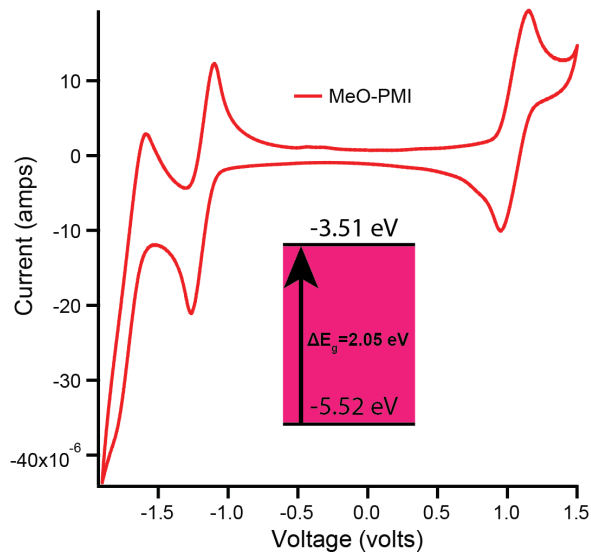


Figure 8.8. Cyclic voltammogram of MeO-PMI (5 mM) in DCM with 0.1 M tetrabutylammonium hexafluorophosphate as the supporting electrolyte. Ferrocene internal standard was used to calibrate scans. Inset shows an energy diagram constructed from CV and UV-Vis data.

8.12. WAXS sensitivity to structural details

Referring to Figure 3.6B and Figure 8.9, the (11) peak has higher intensity than the model prediction but shows a closer match for integral intensity. We surmise that this is due to the difference in the correlation lengths along different directions as also suggested by the AFM image (Figure 3.4C) of the sheets, which have an elongated aspect ratio. To reduce the number of free parameters our model assumed domains to be circular and thereby all peaks were given the same width. Note that the peak at $q_r = 1.93 \text{ \AA}^{-1}$ is most likely an artifact from small 3D single crystalline contaminants, as is suggested by the appearance of two small diffraction spots in the Fig. 2a GIWAXS image near $q_z = 0$.

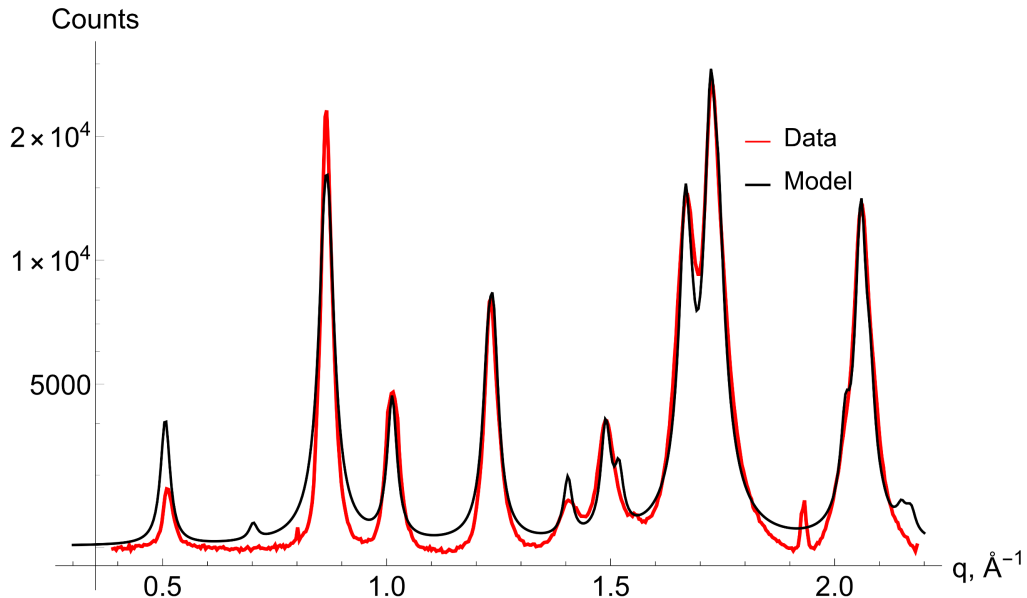


Figure 8.9. Best fit to the full model from the main text in the log scale of counts.

Simplified models do not fully reproduce the correct intensity distribution. Examples of missing features are shown below.

Model with no chains

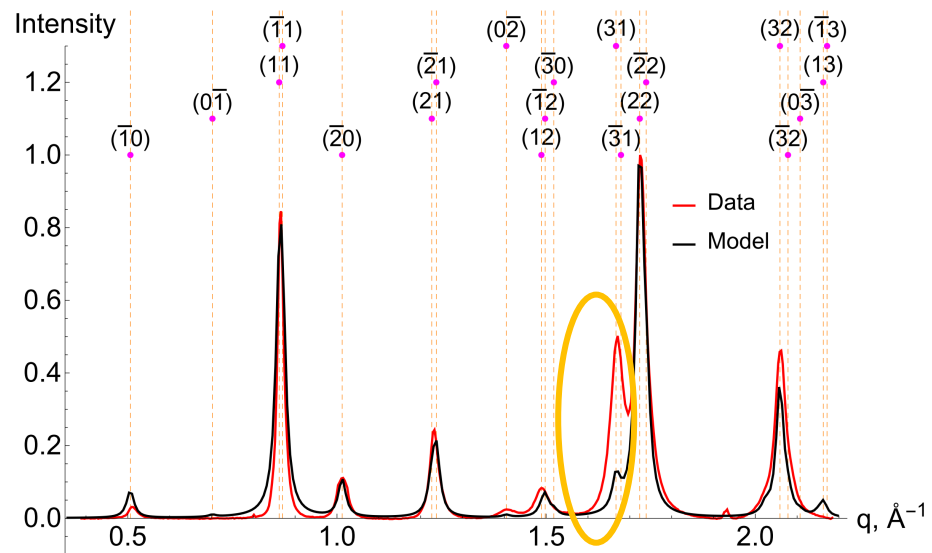


Figure 8.10. The best fit for a model consisting of plates without carboxypentyl chains

Models with chains at right angle with respect to the plates

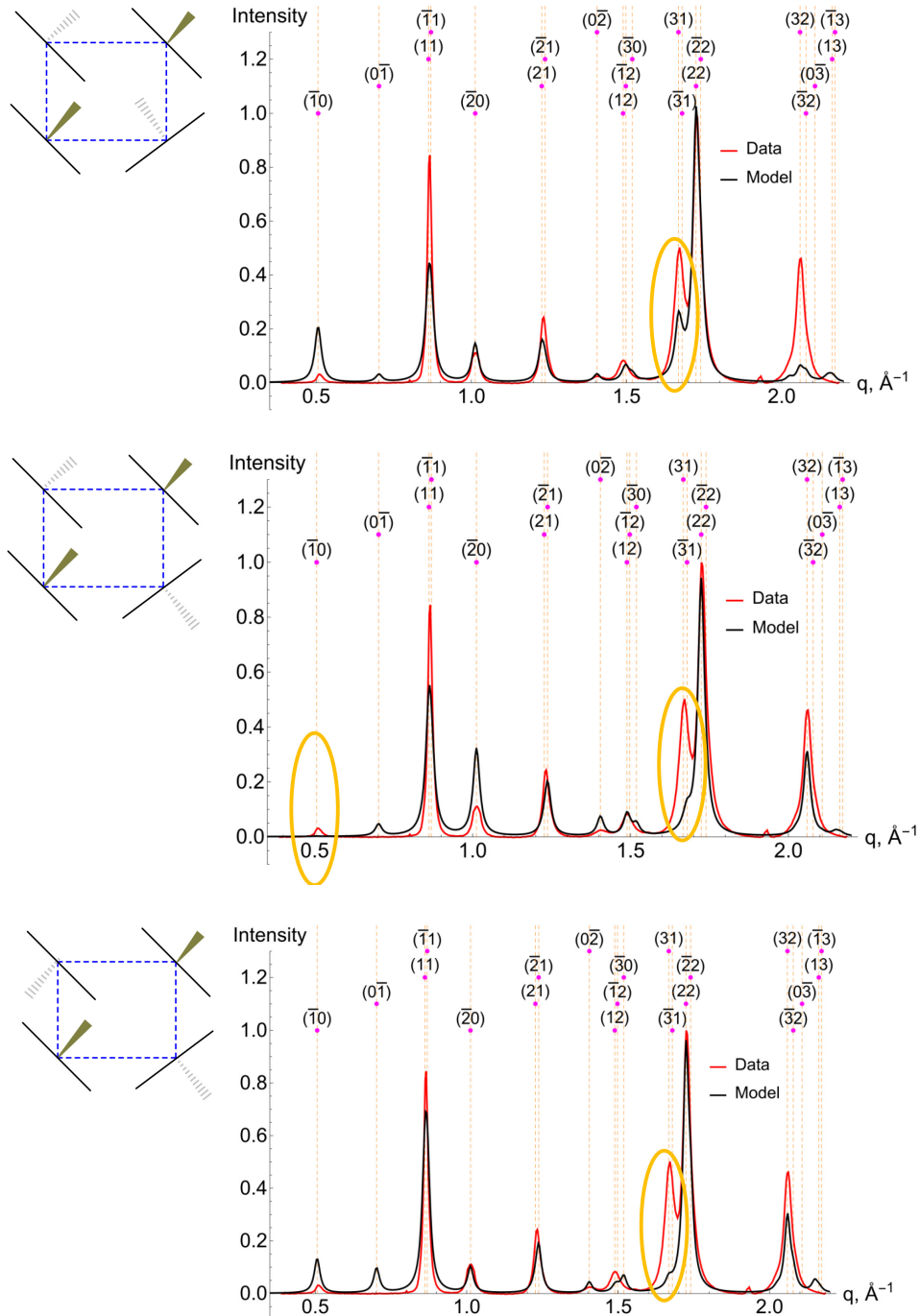


Figure 8.11. Best fits for models with the angle of the chain with respect to the plate frozen to normal during fitting procedure.

Models with different tilt angles between the stacked plates

In the following fits the tilt angle is fixed.

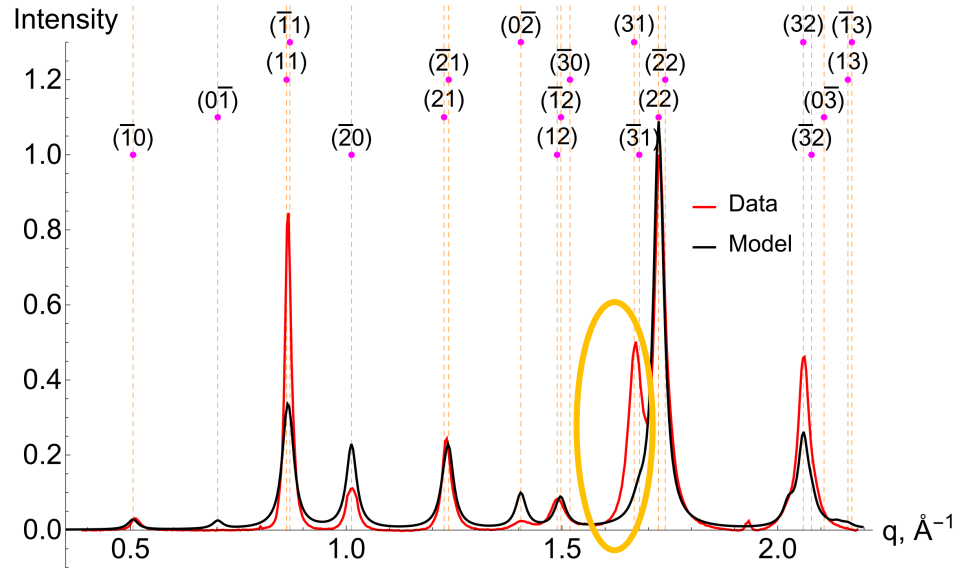


Figure 8.12. Best fit for a model with zero tilt angle (i.e. rotational angle between two plates is 0)

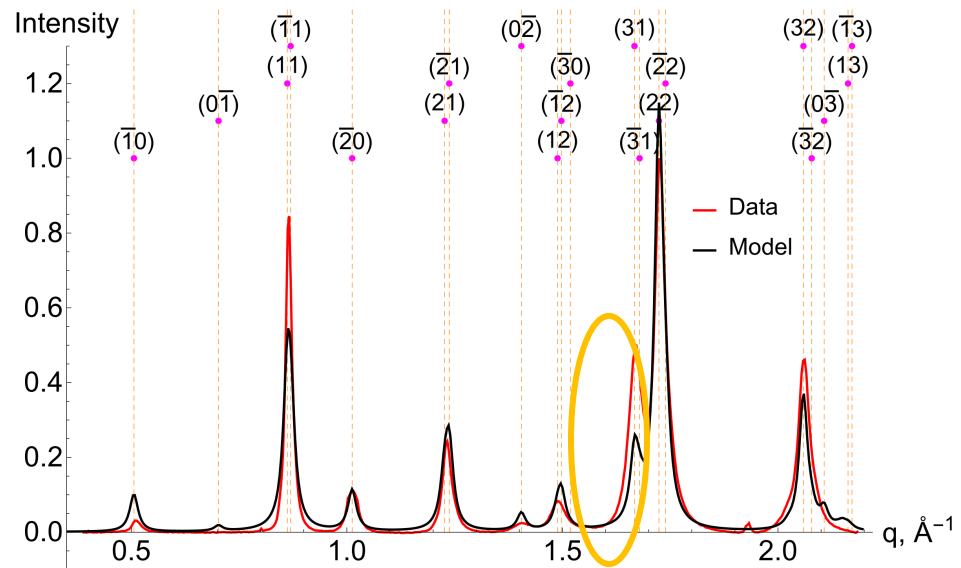


Figure 8.13. Best fit for a model with 8.2° tilt angle (i.e. rotational angle between two plates is 16.4°)

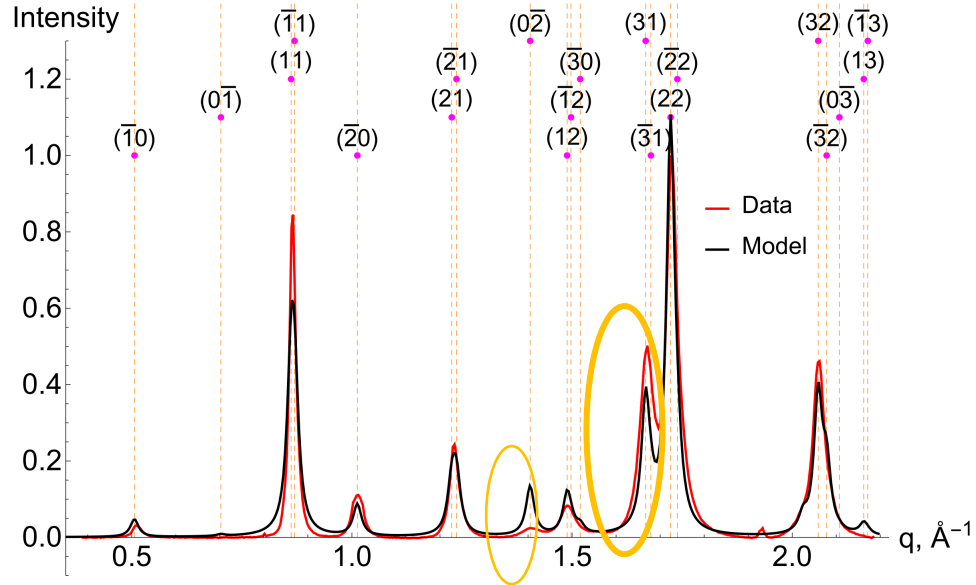


Figure 8.14. Best fit for a model with 31.4° tilt angle (i.e. rotational angle between two plates is 62.8°)

8.13. Statistical errors on GIWAXS fitted parameters

The table below lists the parameters and uncertainties (at 95% confidence level) obtained from the non-linear fitting of the model (described in the main text) to the GIWAXS line cut (Fig. 3b). Each of the $\alpha_{x,i}$ angles is measured counterclockwise from unit cell vector \vec{a} (Fig. 3c,d). Subscript p is for the plate and c is for the chain angles. Subscript $i = 1$ corresponds to the lower left corner molecule with 2, 3, and 4 corresponding in counterclockwise order to the other 3 molecules in the basis. The variance estimator function was set to $\sum_i \frac{w_i(I_i - \hat{I}_i)^2}{n-P}$, where I_i is the observed intensity at the i th data point, \hat{I}_i is the model predicted intensity, $w_i = I_i^{-1}$ is the Poisson weight, n is the number of data points and P is the number

of free parameters. Notice that the uncertainties for the rotation angles of the chains are approximately 3 times larger than those for the plates. This is due to the plates having 3 times more electrons.

Table 8.1. Statistical uncertainties on fit parameters at 95% confidence level.

	$\sigma, \text{\AA}^{-1}$	$l_{p,y}, \text{\AA}$	$\alpha_{p,1}, {}^\circ$	$\alpha_{p,2}, {}^\circ$	$\alpha_{p,3}, {}^\circ$	$\alpha_{p,4}, {}^\circ$	$\alpha_{c,1}, {}^\circ$	$\alpha_{c,2}, {}^\circ$	$\alpha_{c,3}, {}^\circ$	$\alpha_{c,4}, {}^\circ$
Value	0.0108	9.12	142.5	38.9	156.8	130.4	78.3	112.0	76.6	119.3
Uncertainty	0.0002	0.06	0.5	0.5	0.7	0.6	1.4	2.0	1.6	2.2

9. Appendix B

The code below implements solution WAXS diffraction pattern simulation on *Mathematica*.

```

Remove[f, f2, F, n, nn, div, \[Pi], Q, G, int, l];
counter = 0;
(*Upper Limit of Q at which to consider*)
Quplim = 2.5;
(*Order of peaks to represent*)
nn = 5;
(*Sigmas of precision*)
n = 2;
(*Double integration divisions*)
div = 7;
(*Unit cell sizes and sizes of the model slab*)
w = 1.2; dl = 4.8; dw = 1.8;
(*number of electrons on the slab*)
Nel = 33 * 6 + 31 * 1 + 2 * 7 + 4 * 8.; (*as=15.815/2;
bs=8.813/2;
\phi=121.7 Degree;*)

(*Defining the Q through Cartesian decomposition for G*)

G[n_, k_, as_, bs_, \phi_] :=  $\frac{\pi}{bs \sin[\phi]} k \{0., 1., 0.\} + \frac{\pi}{as \sin[\phi]} n \{\sin[\phi], -\cos[\phi], 0.\}$ ;
(*Form factor of the slab*)
fw[Q_, w_, l_] := Sinc[Q[[1]] l/2] Sinc[Q[[2]] w/2];
(*Form factor of the tail*)
fwt[Q_, dw_, dl_] := 1./3 Sinc[dl Q[[1]]/2] Sinc[dw Q[[2]]/2] E^I^{dl/2 Q[[1]]};

(*Here \phi is just a variable for this function*)
M[\alpha_] = RotationMatrix[\alpha, {0, 0, 1}];
(*Parallel component of the form factor. Notice,
only l is left as a free variable, the w, dl, dw are fixed as constants above*)
Fw[Q_, p_, pc_, l_, a_, b_] :=
  fw[M[-p[[1]]].Q, w, l] + fw[M[-p[[2]]].Q, w, l] E^{I a . Q} +
  fw[M[-p[[3]]].Q, w, l] E^{I (a+b) . Q} + fw[M[-p[[4]]].Q, w, l] E^{I b . Q} +
  fwt[M[-pc[[1]]].Q, dw, dl] + fwt[M[-pc[[2]]].Q, dw, dl] E^{I a . Q} +
  fwt[M[-pc[[3]]].Q, dw, dl] E^{I (a+b) . Q} + fwt[M[-pc[[4]]].Q, dw, dl] E^{I b . Q};
(*Perpendicular component of the form factor*)
Fp[Qz_, h_] := Sinc[Qz \frac{h}{2}];

f2[Q_, \theta_, \sigma_, G_] := \sigma Exp[-\frac{(Q \sin[\theta] - G)^2}{2 \sigma^2}] \sqrt{\frac{2 \pi \sin[\theta]}{Q G}};

(*pw are the rotational angles, aw, bw,
phw are correspondingly lattice sides and lattice angle*)
(*p is the list of angles of the slabs and pc is that of the chains*)
int[Q_?NumberQ, p_?{VectorQ[\#, NumberQ] &}, pc_?{VectorQ[\#, NumberQ] &},
l_?NumberQ, h_?NumberQ, \sigma_?NumberQ, as_?NumberQ, bs_?NumberQ, \phi_?NumberQ] :=

```

```

Module[{i, j, θ, intensity, a1, aup, AbsG, a, b, at, bt, Gt},

intensity = 0.;

at = {as, 0., 0.};

bt = {bs Cos[φ], bs Sin[φ], 0.};

For[i = 0, i <= nn, i++,
  For[j = -nn, j ≤ nn, j++,
    If[(! (i == 0 && j == 0)),
      Gt = G[i, j, as, bs, φ];
      (*Magnitude of G 2D lattice vector = t1*)
      AbsG = Sqrt[Gt[[1]]^2 + Gt[[2]]^2];
      If[AbsG < Quplim,
        (*Limits of the peak's region of existence*)
        a1 = AbsG - n σ;
        aup = AbsG + n σ;

        Which[aup ≥ Q > a1 > 0.,
          a = ArcSin[a1/Q]; b = π/2.;
          intensity = intensity + 2 Abs[Fw[Gt, p, pc, l, at, bt]]^2 *
            Sum[f2[Q, θ, σ, AbsG] * Sinc[Q Cos[θ] h/2]^2 * (b-a)/div, {θ, a, b, (b-a)/div}],
          Q > aup > 0.,
          a = ArcSin[a1/Q]; b = ArcSin[aup/Q];
          intensity = intensity + 2 Abs[Fw[Gt, p, pc, l, at, bt]]^2 *
            Sum[f2[Q, θ, σ, AbsG] * Sinc[Q Cos[θ] h/2]^2 * (b-a)/div, {θ, a, b, (b-a)/div}]

        ];
      ];
    ];
  ];
];

LinkWrite[$ParentLink, SetNotebookStatusLine[FrontEnd`EvaluationNotebook[],
  ToString[{counter++, p, pc, l, h, σ, Q(*,intensity*)}]]];

intensity
];

```

10. Appendix C

The code below implements GIWAXS diffraction pattern simulation on *Mathematica*. The procedure is described in the main text.

```
(*Specifying the incidence angle and lattice constants*)
(*Incidence angle*)
αi = 0.2 Degree;
(*lattice constants for general triclinic unit cell. For coding
convenience different notation is used than in the main text*)
a = 8.9274; b = 64.383; c = 8.8816;
(*inputting crystallographic angle α*)
θ = 90 Degree;
(*inputting crystallographic angle β*)
χ = 90 Degree;
(*inputting crystallographic angle γ*)
ϕ = 90 Degree;
(*Miller plane parallel to substrate*)
p1 = {0, 1, 0};
(*wavelength of the X-ray beam in Å*)
λ = 1.6868;
(*Orientational standard deviation of the normal n̂ in degrees*)
σθ = 1;
(*Crystallite domain size effect, expressed as std of diffraction gaussian peak*)
σq = 0.01;
(*Wavevector*)kw =  $\frac{2\pi}{\lambda}$ ;
Gc[h_, k_, l_] := Module[{a1, a2, a3, vc, a1s, a2s, a3s,
  n, G, G11(*parallel*), Gp (*perpendicular*), α, β, at, bt, v},
  a1 = a {Sin[ϕ], Cos[ϕ], 0};
  a2 = b {0, 1, 0};
  a3 = c {Cos[χ] Sin[ϕ], Cos[χ] Cos[ϕ] + Cos[θ],  $\sqrt{1 - \cos[\theta]^2 - \cos[\chi]^2}$ };
  vc = a1.Cross[a2, a3];
  a1s =  $\frac{2\pi}{vc}$  Cross[a2, a3];
  a2s =  $\frac{2\pi}{vc}$  Cross[a3, a1];
  a3s =  $\frac{2\pi}{vc}$  Cross[a1, a2];
  n = {p1[[1]]/a, p1[[2]]/b, p1[[3]]/c};
  G = h a1s + k a2s + l a3s;
  n =  $\frac{n}{Norm[n]}$ ;
```

```

Gp = n.G;
Gll = Sqrt[G.G - Gp^2];
at = Gp/(kappa w) - Sin[alpha i];
bt = 
$$\left( 2 \cos[\alpha i] \sqrt{1 - \left( \frac{Gp}{\kappa w} - \sin[\alpha i] \right)^2} \right)^{-1} \left( 1 + \cos[\alpha i]^2 - \frac{Gll^2}{\kappa w^2} - \left( \frac{Gp}{\kappa w} - \sin[\alpha i] \right)^2 \right);$$


beta = Re@ArcSin[at];
alpha = Re@ArcCos[bt];
v = kappa w {Cos[beta] Sin[alpha], Sin[beta] + Sin[alpha]};
(*Outputting a pair of coordinates {Qy, Qz}*)
v
];

(*Inputting the table saved from SingleCrystal software*)
tab =
Import["X-Ray Reciprocal Lattice- BA2MA3Pb4I13_Cc2m Listing single crystal full.txt",
"Table"];
tab = DeleteCases[tab, x_ String /; ! StringContainsQ[x, __ ~~ "%"], 2];
tab = ReplaceAll[tab,
x_ String /; StringContainsQ[x, __ ~~ "%"] :> ToExpression[StringDrop[x, -1]]];
tab = DeleteCases[tab, {}];
peaks = Reap[
For[i = 1, i < Length[tab] + 1, i++,
coor = tab[[i, 1 ;; 3]];
Sow[{coor, Gc[Apply[Sequence, coor]], tab[[i, 4]], tab[[i, -1]] }];
]];
[[[2, 1]]];
peaks = DeleteCases[peaks, {_, {0, 0}, ___}];
peaks = SortBy[peaks, -#[[-1]] &];
peaksall = peaks;
peaks = Select[peaks, #[[-1]] > 1 &];
r = Sqrt[qy^2 + qz^2]; theta = ArcCos[qy/(r + 1.*10^-8)];

```

```
(*Writing the total intensity as a function in Cartesian frame {qy, qz}*)
f = Sum[peaks[[i, -1]] PDF[NormalDistribution[ArcTan[ $\frac{\text{peaks}[[i, 2, 2]]}{1. * 10^{-8} + \text{peaks}[[i, 2, 1]]}$ ],  $\frac{\sigma\theta \text{ Degree}}{\sqrt{\text{peaks}[[i, 2, 2]]^2 + \text{peaks}[[i, 2, 1]]^2}}$ ] * 2 π / peaks[[i, 3]]], θa]
PDF[NormalDistribution[ $\sqrt{\text{peaks}[[i, 2, 2]]^2 + \text{peaks}[[i, 2, 1]]^2}$ , σq], r ], {i,
1, Length[peaks]}];

(*Printing the simulated graph*)
gr = DensityPlot[f, {qy, -0.1, 2.2}, {qz, 0, 2.2}, ColorFunction → "TemperatureMap",
PlotRange → {0, 25000}, ClippingStyle → Red, ImageSize → 800,
FrameStyle → Directive[Black, 50], FrameLabel → {"qy, Å-1", "qz, Å-1"}, PlotPoints → 90]
```